universität wien

MASTERARBEIT / MASTER'S THESIS

Titel der Masterarbeit / Title of the Master's Thesis

"Properties of the Laves phase C14 ($MgZn_2$) in the quaternary system Al-Fe-Si-Ti"

verfasst von / submitted by

Patric Berger, BSc.

angestrebter akademischer Grad / in partial fulfilment of the requirements for the degree of

Master of Science (MSc.)

Wien, 2016 / Vienna, 2016

Studienkennzahl lt. Studienblatt / degree programme code as it appears on the student record sheet:	A 066 862
Studienrichtung lt. Studienblatt / degree programme as it appears on the student record sheet:	Masterstudium Chemie
Betreut von / Supervisor:	ao. Univ.-Prof. Mag. Dr. Klaus Richter

Preface

This work was undertaken from August 2015 to May 2016 in the working group of ao. Univ.-Prof. Mag. Dr. Klaus Richter at the Department of Inorganic Chemistry-functional materials.

Herewith, I would like to thank all people who have contributed to this master thesis.

In particular,

ao. Univ.-Prof. Dr. Klaus Richter for giving me the opportunity to work on this interesting topic and his great supervision.

Alexander Beutl Msc., Peter Kainzbauer MSc., Dr. Martin Marker, Gabriel Reisinger MSc. and all other colleagues of the working group Inorganic Chemistry-functional materials for their support and the nice working atmosphere during this time.

Dr. Stephan Puchegger, from the Faculty Center for Nanostructure Research for helping me with the SEM-measurments.

My friends and colleagues Evi, Hiasi, Christian, Sepp and Björn for their afterwork discussions and entertainment.

My family for their support throughout the life.

Contents

1. Introduction

Laves phases, with the general composition AB_2, represent the largest group of intermetallic compounds. They are formed from almost all metals and crystallize in topologically closed-packed structures, whereby three different polytypes can be distinguished: the cubic $MgCu_2$ type (C15), the hexagonal $MgZn_2$ type (C14) and the hexagonal $MgNi_2$ (C36). Most of the Laves phases show a distinct brittleness at ambient temperature. However, an enormous strength up to high temperature is characteristic for most of them **[1]**.

There are several functional as well as structural applications for Laves phases. Especially their utilization as hydrogen storage materials in rechargeable Ni-MH batteries has to be mentioned **[2, 3]**. Furthermore, they were applied as super-conducting magnets, as magnetoelastic transducers and as wear resistance materials **[4]**. To improve and to characterize the physical and mechanical properties of Laves phases a huge number of studies was done during the last years, like **[5-10]**.

The hexagonal Laves phase Fe_2Ti (C14) shows, like several other binary Laves phases, a large solubility of third elements without changing its crystal structure type. Previous studies on the ternary systems Al-Fe-Ti and Fe-Si-Ti reported an increasing solid solubility of Al in Fe_2Ti from 33.5 at.% at 800 °C to 47 at.% at 1000°C [**11**]; the solubility for Si reaches around 27 at.% and shows a temperature independent behavior in the range from 850-1050 °C **[12]**. The quaternary system Al-Fe-Si-Ti has also been investigated in the iron rich corner at 900 °C **[9, 10]**. Marker et al. reported a large solubility of the binary Laves phase Fe_2Ti in the quaternary system towards the Ti-poor side.

The aim of this work was the characterization of the homogeneity range of the Laves phase Fe_2Ti (C14) in the quaternary system Al-Fe-Si-Ti. Based on the given work by Marker et al. **[10]**, three partial isothermal sections at 900 °C at 20, 25 and 33.3 at.% Ti were investigated by XRD, SEM and LOM. The dependence of the site occupancy on the composition for the Laves phase Fe_2Ti in the quaternary system Al-Fe-Si-Ti, as well as in the ternary system Fe-Si-Ti, was studied by Rietveld refinement of XRD-patterns. Furthermore, the behavior of the lattice parameters *a* and *c,* as well as the volume of the Laves phase Fe_2Ti by increasing amounts of additional elements, was investigated for the Fe-Si-Ti and the Al-Fe-Si-Ti system.

2. Basic materials

2.1. Aluminium

Natural occurrence

Aluminium, the most common metal in the earth's sheath, is the third most abundant element after oxygen and silicon. Due to its high chemical affinity to oxygen, it does not exist in a pure manner, but in oxidic compounds. Naturally, aluminium occurs in the form of corundum (Al_2O_3), hydrargillite ($Al(OH)_3$), boehmite (AlO(OH)) or in terms of myriad combinations with other metal oxides and hydroxides. The main representatives of the last-mentioned compounds are the alumosilicates like feldspar and micas as well as the weathering products of feldspar, the clays, which in turn effloresces to bauxites.

Atomic number	13
Classification	Boron group 13th
Electron configuration	[Ne] $3s^2$ $3p^1$
Atomic mass ($g \cdot mol^{-1}$)	26.982
Covalent radius (pm)	118
Melting point (K)	933.5
Density ($g \cdot cm^{-3}$)	2.7

Table 1: Characteristics of aluminium [14, 15].

Extraction

The industrial production of aluminium is based on two separate operations. At the first step pure Al_2O_3 is extracted from red bauxite by the Bayer-process, where iron(III)oxide and silicon oxide are removed. Afterwards the aluminium oxide is undergone to the fused-salt electrolysis whereby cryolite (Na_3AlF_6) functions as melting point-lowering agent. By this, the melting point is reduced to 940-980 °C. The fused-salt electrolysis works with currents up to 30 000 A with a current density of 0.4 A/cm^2 and an operating voltage of 4.5-5.0 V **[13]**.

Physical properties

Aluminium crystallizes in a cubic close packing (*cF4*) with the space group $Fm\bar{3}m$ **[16].** The Mohs hardness is 2.75 **[15]**. Due to the fact that aluminium is stainless, thermal and electric leading and mechanical easy malleable it represents the most important non-iron metal in technical applications.

Chemical properties

Based on its affinity to be trivalent, aluminium reacts with most non-metals by warming. Furthermore, aluminium forms alloys with almost all metals, reacts with free and ligated oxygen under oxygen-intake and with acids and bases under hydrogen development. Solid aluminium is passivated by a permanent oxid surface layer **[13]**.

2.2. Iron

Natural occurrence

Iron is the fourth most common element in the earth's sheath with a mass fraction of 4.7 %. In the lithosphere it mostly occurs in form of oxides, sulfides and carbonates. Iron-containing rocks, which were separated from magma, usually show the oxidation number II; in contrast, their weathering products presents the trivalent form. The main iron ores are magnetite ($FeO \cdot Fe_2O_3$), hematite (Fe_2O_3), siderite ($FeCO_3$), pyrite (FeS_2), wüstite ($Fe_{1-x}O$), chalcopyrite and bornite.

Atomic number	26
Classification	Iron group 8th
Electron configuration	[Ar] $3d^6$ $4s^2$
Atomic mass ($g \cdot mol^{-1}$)	55.845
Covalent radius (pm)	125
Melting point (K)	1811.2
Density ($g \cdot cm^{-3}$)	7.874

Table 2: Characteristics of iron [14, 15].

Extraction

Crude iron is produced by reduction of iron oxide containing ores with coke in blast furnace. Therefore, coke and a mixture of iron ores and ore burden are put inside the blast furnace in alternating layers. Ore burden is used to transfer admixtures of the ores into low melting calcium-aluminium-silicates (scoria). Based on the temperature gradient in the furnace between 1600 °C on the ground and about 250 °C on the top, several temperature dependent reactions are taking place. The products of the blast furnace are crude iron, scoria and furnace gas. The liquid crude iron still contains 2.5-4 % carbon, and varying concentrations of silicone (0.5-3 %), manganese (0.5-6 %), phosphor (0-2 %) and traces of sulphur **[13]**.

Physical properties

Iron occurs in three enatiotropic modifications, where the conversion temperatures are 906°C and 1401°C. The α-formation crystallizes in cubic body centered structure (cI2) with the space group $Im\bar{3}m$ and shows ferromagnetic properties **[13]**. γ-Iron illustrates a cubic close packing (cF4) with the space group $Fm\bar{3}m$ **[16]** and is paramagnetic. The δ-type shows a cubic body centered structure (cI2) with the space group $Im\bar{3}m$ **[16]** and paramagnetic behavior. At 768°C α-iron loses its ferromagnetic nature and becomes paramagnetic. The Mohs hardness is 4 **[15]**. Chemical pure iron plays a minor part in technical applications; in contrast, the carbonic iron compounds are by far the most important materials in industrial productions.

Chemical properties

In alkalis, on dry air, in air- and in carbon dioxide-free water, pure iron is stable against oxidation. This reliability is based on a thin oxide-layer, like in case of aluminum. This phenomenon is also the reason for the invulnerability of iron in concentrated sulfuric acid and nitric acid. However, in wet and carbon dioxide-rich air or in carbon dioxide- and aerated water the iron gets oxidized under development of iron (III) oxyhydroxide (FeO(OH)). In non oxidizing acids such as muriatic acid and dilute sulfuric acid it dissolves under hydrogen development and Fe(II) formation. Iron solubilises in water above 500°C and hot alkalis in reversible reactions. Under heating it also reacts with many non-metals such as B, C, Cl and P **[13]**.

2.3. Silicon

Natural occurrence

Silicon is the second most abundant element in the earth crust with a mass fraction of 26.3%. In consequence of its high oxygen affinity it is not found elementary but in form of salts. Thereby, the salts (silicate) are based on silicic acid ($m SiO_2 \cdot n H_2O$) which are derived from the anhydride $SiO_2.SiO_2$ occurs in form of quartz, pebble, berg crystal, amethyst and so on. Many silicon containing minerals are on the basis of magnesium-, calcium-, iron-, and aluminosilicates.

Atomic number	14
Classification	carbon group 14th
Electron configuration	[Ne] $3s^2$ $3p^2$
Atomic mass ($g \cdot mol^{-1}$)	28.086
Covalent radius (pm)	111
Melting point (K)	1687.2
Density ($g \cdot cm^{-3}$)	2.33

Table 3: Characteristics of silicon [14, 15].

Extraction

Technically, silicon is recovered by reduction of quartz with coke and temperatures above 2000°C in an arc-reduction-furnace. In this way the silicon gets a chemical purity of 98.5 w% in case of Si98 and 99.7 w% in case of Si99. Purest silicon is obtained by thermal reduction of silicochloroform ($HSiCl_3$) with hydrogen at 1000 °C or pyrolysis of cleanest silane (SiH_4) **[13]**.

Physical properties

α-silicon crystallizes in a cubic diamond structure (*cF8*) with the space group $Fd\overline{3}m$ **[16]**. Furthermore, several high-pressure modifications exist. By the use of increasing pressure the individual forms show growing density. Additionally, the co-ordination number of the silicon in the crystal system grows from 4 to 12 **[13]**. The Mohs hardness is 6.5 **[15]**. High-purity silicon is mostly used in semiconductor and solar cells technology.

Chemical properties

At temperatures above 1000°C Si scorches on the air to silicone oxide. Beneath this temperature the primary oxide-layer prevents this process. In water it will be converted under an exothermic reaction into hydrogen and SiO_2. In spite of its huge negative electrode potential from ε_0 = - 0.909 V, silicone is practical indissoluble in all acids. In contrast to this, it easily solves in hot alkalis under exothermic reactions in silicates and hydrogen **[13]**.

2.4. Titanium

Natural occurrence

Titanium is the 10th most element in the earth sheath and naturally occurs in oxidic compounds. The main titanium sources are iron containing ores, e.g. ilmenite ($FeTiO_3$). Further titanium sources are titanite ($CaTiO[SiO_4]$), perowskite ($CaTiO_3$) and titanium oxide (TiO_2). The last-mentioned mineral shows three different crystal structures types: the common rutile-typ, the tetragonal anatase-type and the rhombic brookite-type.

Atomic number	22
Classification	Titanium group 4th
Electron configuration	[Ar] $3d^2$ $4s^2$
Atomic mass ($g \cdot mol^{-1}$)	47.867
Covalent radius (pm)	136
Melting point (K)	1941.2
Density ($g \cdot cm^{-3}$)	4.507

Table 4: Characteristics of titanium [14, 15].

Extraction

The industrial production of titanium is based on the so-called Kroll-process. Therefore, chlorine gas is lead over a 1000 °C heated mixture of coke and titanium oxide. The resulting $TiCl_4$ is reduced by magnesium under an inert atmosphere and 1000 °C. The crude titanium sponge still holds 25 % $MgCl_2$, 10-20 % Mg. Almost pure titanium obtained by eluviations with aqua regia or removing$MgCl_2$ and Mg by vacuum-distillation. Afterwards it only contains traces of H, O, N, Cl, Mg, Fe, and Si, in a concentration area far below 0.2% **[13]**.

Physical properties

Basically, two different crystal modifications are known. α-Titanium crystallizes in hexagonal close packing unit cell (*hP2*) with the space group $P6_3/mmc$ **[16]**. However, β-titanium shows a cubic body centered structure (*cI2*) with the space group $Im\bar{3}m$ **[16]**. The conversion temperature amounts to 882.5°C **[13]**. The Mohs hardness is 6 **[15]**.

Chemical properties

Titanium shows a pronounced resistance to corrosion against atmospheric gases attributed to its permanent oxide-layer. At high temperatures it deflagrates turbulently. Titanium powder exhibits pyrophoric properties. In warm environment it reacts with almost all non-metals, e.g. with hydrogen to TiH_2 or halogens to TiX_4. The presence of traces of C, H, N and O makes titanium brittle **[13]**.

3. Literature

3.1. Binary system

3.1.1. Fe-Ti

Based on its technical applications, the iron-titanium phase diagram has been intensively investigated, over the whole composition range, for a long time.

The studies on the binary system can be retraced at least back to the beginning of the 20th century, when Lamort investigated the iron rich corner up to 21.51 wt.% titanium. In this area, only iron-rich alloys and the compound Fe_3Ti was found **[17]**. Jellinghaus confirmed the existence of Fe_3Ti and determined its crystal structure as Al_3Ti-type **[18]**. Witte and Wallbaum could not confirm the existence of a Fe_3Ti phase. However, the compound Fe_2Ti with $MgZn_2$ structure was reported **[19]**. Laves and Wallbaum described the phase $FeTi_2$, which was refuted by Ray and Dew-Hughes several years later **[20, 21, 22]**.

The first calculated phase diagram was done by Kaufmann and Nesor **[23]**. In 1981, Murray published the first assessed Fe-Ti phase diagram containing bibliographic information up to 1980 **[24]**. A reassessment of the Fe-Ti system was performed by Murray several years later **[25]**, as shown in Fig. 1.

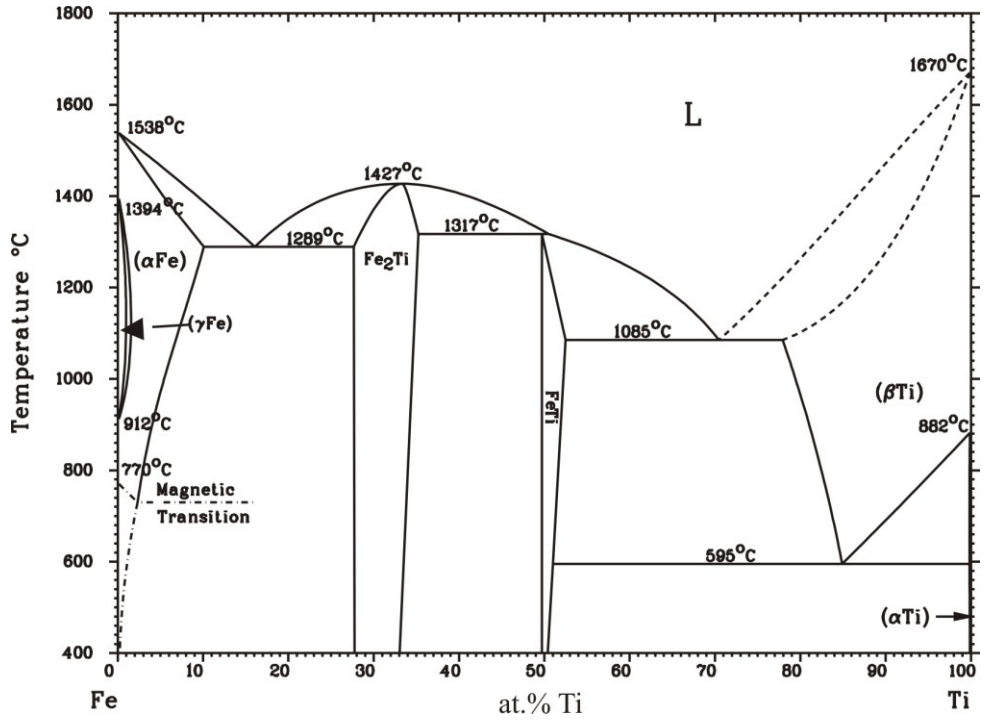

Fig. 1: Mirrored Fe-Ti phase diagram according to Murray [25].

The phase diagram shows two binary phases, whereby Fe_2Ti melts congruently at 1427 °C and FeTi forms in a peritectic reaction at 1317 °C. At 1085 °C FeTi has a maximum composition range of 48 to 50.2 at.% iron. Fe_2Ti exhibits a maximum homogeneity range of 64.5 to 72.5 at % iron. The bcc-type solid solution connects the α- and δ-iron and extends to approximately 10 at.% Ti. It includes a γ-loop between 912 and 1394 °C. The magnetic transition temperature of pure iron is reported to be at 770° C. Pure Ti is separated into α-Ti by temperatures below 882° C and β-Ti by temperatures above 882 °C. The homogeneity range of β-Ti extends to approximately 22 at.% Fe **[25]**. Relevant data for the Fe-Ti phase diagram are listed in Table 5 and 6.

Table 5: Binary phase equilibria of the Fe-Ti phase diagram [25].

Reaction	Composition (at.% Fe)			Temperature (°C)	Reaction type
δFe ↔ γFe		100		1394	allotropic
γFe ↔ αFe		100		911	allotropic
L ↔ αFe		100		1538	melting
L ↔ βTi		0		1670	melting
αTi ↔ βTi		0		882	allotropic
L ↔ Fe_2Ti		66.7		1427	congruent
L ↔ Fe_2Ti + (αFe)	84	72.4	90	1289	eutectic
L + Fe_2Ti ↔ TiFe	49.5	64.8	50.3	1317	peritectic
(βTi)↔ (αTi) + FeTi	15	0.004	49	595	eutectic
L ↔ (βTi) + TiFe	29.5	21	47.5	1085	eutectic

Table 6: Crystal structure data of the Fe-Ti phase diagram [25].

Phase	Composition (at.% Fe)	Pearson symbol	Space group	Strukturbericht designation	Structure type
ω	metastable	*hP*3	*P6/mmm*	…	ωMnTi
(γFe)	99.4 to 100	*cF*4	$Fm\bar{3}m$	*A*1	Cu
(αFe)	90 to 100	*cI*2	$Im\bar{3}m$	*A*2	W
Fe_2Ti	64.5 to 72.4	*hP*12	$P6_3/mmc$	*C*14	$MgZn_2$
FeTi	48 to 50.2	*cP*2	$Pm\bar{3}m$	*B*2	CsCl
(βTi)	0 to 22	*cI*2	$Im\bar{3}m$	*A*2	W
(αTi)	0 to 0.04	*hP*2	$P6_3/mmc$	*A*2	Mg

Based on new phase diagram data several CALPHAD-type reassessments have been published. Hari Kumar made a thermodynamic description by the least-square optimization of literature data and modeled the homogeneity range of the Laves phase Fe_2Ti using a 3-

sublattice model **[26]**. Jonsson reassessed the Fe-Ti system with the purpose to use it for extrapolations in the ternary systems Fe-Ti-N and Fe-Ti-C **[27]**. Dumitrescu et al. summarized certain CALPHAD-type assessments up to that point and considered that it is futile to make a superior assessment without new experimental information **[28]**. G. Cacciamani et al. refers to the Fe-Ti phase diagram by Hari Kumar, as shown in Fig. 2. The homogeneity range for the FeTi phase was calculated using a 3-sublattice model. Furthermore, he linked the Gibbs energy of the FeTi with the Gibbs energy of the disordered phases (*A*2) to correlate the order-disorder transformation between the ordered FeTi and the disordered bcc phases. Notably, the Gibbs energy of the disordered phase (*A*2) contains the magnetic contribution **[29]**. The major distinctions between the phase diagram by Murray **[25]** and the one by Hari Kumar **[29]** are the congruent melting point of Fe_2Ti, the peritectic reaction temperature of FeTi and the eutectic reaction temperature between FeTi and α-Ti. Moreover, the homogeneity range of Fe_2Ti differs. Bo et al. also agree with Kumar, excluding the specific heat capacities of Fe_2Ti and FeTi. They reassessed the binary system Fe-Ti with the purpose to use it for extrapolation in ternary or higher-order systems **[30]**.

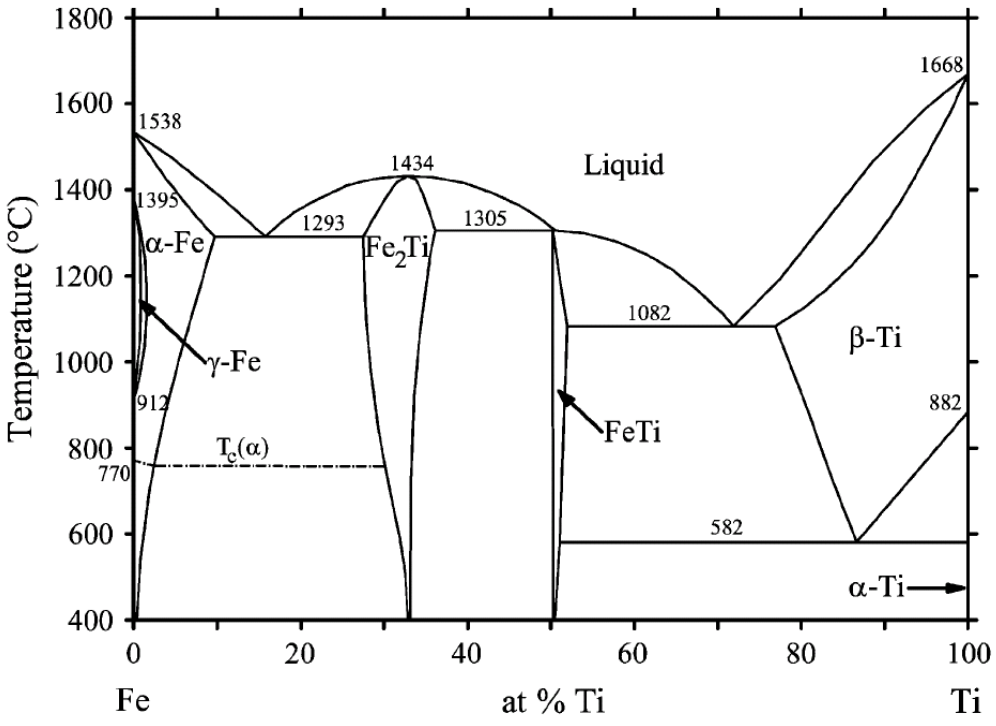

Fig. 2: Fe-Ti phase diagram according to Hari Kumar [29].

3.2. Ternary systems

3.2.1. Al-Fe-Ti

Early work on the ternary system Al-Fe-Ti was done by Nishimura and Matsumoto **[31]**. The first ternary compound with the composition of ~Al_2FeTi (τ_2) was reported by Markiv **[32]**. He was also the first one who presented an isothermal section at 800 °C. Thereby, two more ternary compounds with the composition $Al_{22}Fe_3Ti_8$ (τ_3) and $Al_{69}Fe_{25}Ti_6$ (τ_1) were related **[33]**. Dew-Hughes investigated the Ti-rich corner at 1000 °C. The existence of τ_2, as well as τ_3, has been confirmed **[22]**. A further isothermal section at 800 °C was published by Seibold. She also approved the compounds τ_2 and τ_3, but excluded the existence of τ_1. During her work a new compound with the stoichiometric composition (also denoted as τ_1) $TiAlFe_2$ was found **[34]**. It was Palm et al. who reported the first isotherm section over the whole composition range at 900 °C and 1000 °C **[35, 11]**. Furthermore, an isothermal section at 800 °C, which differentiates substantially from all published phase diagrams so far, was published by Palm et al. **[11]**. The ternary compounds τ_2 (Al_2FeTi) and τ_3 ($Al_{22}Fe_3Ti_8$) have been affirmed, but with different homogeneity ranges as reported before.

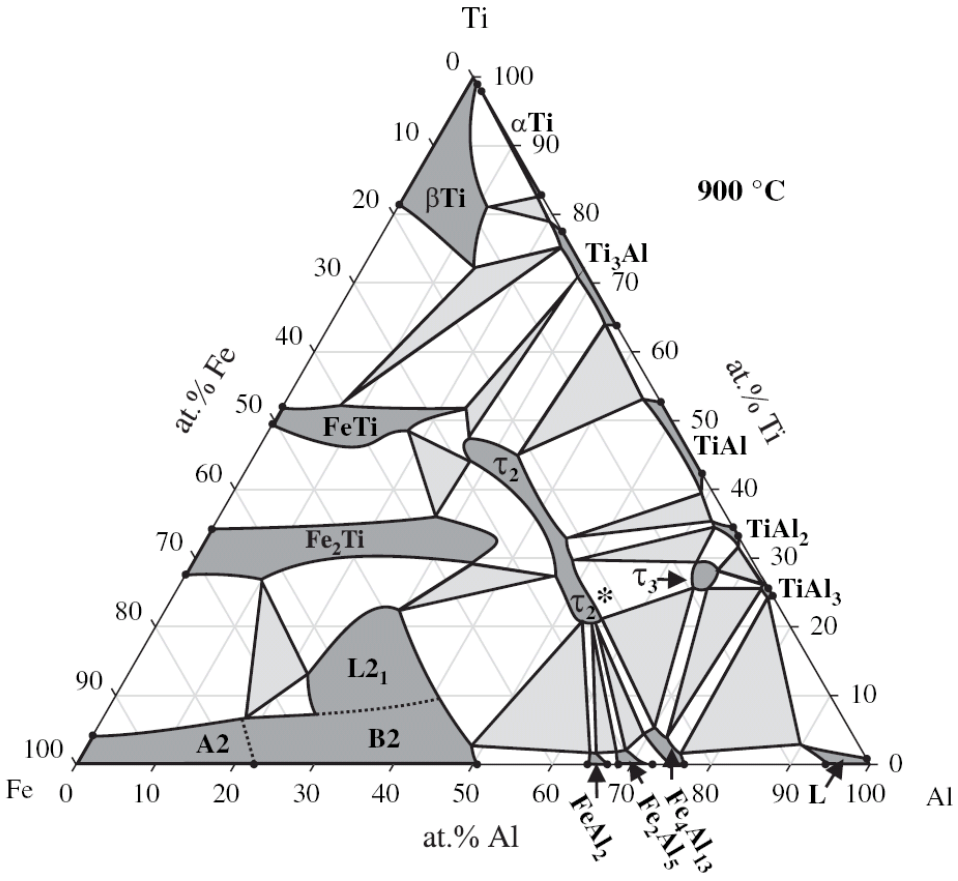

Fig. 3: Isothermal section of the system Al-Fe-Ti at 900 °C [36].

The compound Fe_2AlTi (τ_1) could not be verified by Palm et al. **[11]**. Palm and Lacaze assessed the isothermal sections of ternary system Al-Fe-Ti at 800 °C, 900 °C (shown in Fig. 3) and 1000 °C and presented an isotherm section at 1200 °C **[36]**. The isothermal section at 900 °C, as shown in Fig. 3, was used for the current investigations.

The ternary isothermal section at 900 °C shows two ternary compounds τ_2 and τ_3. τ_2 has a wide homogeneity range and occurs, conditionally on the composition, in two different polytypes **[11]**. At high titanium concentrations it crystallizes as $Mn_{23}Th_6$-type. However, in titanium poor part τ_2^* has a primitive tetragonal structure **[36]**. The homogeneity range of τ_3 extends between 4.8-9.7 at.% Fe, 63.9-66.6 at.% Al and 28.6-25.8 at.% Ti. The cubic phase τ_3 exhibits a $L1_2$ type structure **[36]**.

Furthermore, 16 three-phase fields, 30 two-phase fields and 17single-phase fields are described. An enormous solubility for Al in the Laves phase (Fe_2Ti), where it reaches about 35 at% at 900 °C and FeTi, is reported. The disordered phase β-Ti also shows a distinct high solubility for aluminum **[11, 36]**. The solid solubility of Ti in α-Fe (*A*2) and AlFe (*B*2) was reported to be around 10 at% at 900 °C. Second order transition lines segregate the A2/B2 and $B2/L2_1$ phase fields. The $L2_1$structure type may be formed in a ternary ordering of the binary $D0_3$ structure. Up to date, no clear distinction has been reported when this phase is denoted as $L2_1$ (Heusler-type) or $D0_3$ **[36]**. In the presented ternary system Al-Fe-Ti (Fig. 3) this phase is denoted $L2_1$, corresponding to the ternary ordering. However, throughout the current work the $D0_3$ denotation is used. The solid solubility for Ti in the DO_3 ordered phase Fe_3Al goes up to 23 at%. Due to the high solubility of titanium in DO_3, the DO_3/B2 transition temperature increases from 547°C in the binary system up to 1212°C in the ternary system **[36]**. The relevant crystal structure data for the ternary system Al-Fe-Ti are listed in Table 7.

Table 7: Crystal structure data for the ternary system Al-Fe-Ti. Data for the Fe-Ti phase diagram are given in Table 5 and 6 [36].

Phase	Pearson symbol	Space group	Strukturbericht designation	Prototype
Ti_3Al (α_2)	*hP*8	$P6_3/mmc$	DO_{19}	Ni_3Sn
TiAl (γ)	*tP*4	*P*4/*mmc*	$L1_0$	AuCu
$TiAl_2$	*tI*24	$I4_1/amd$	-	$HfGa_2$
$TiAl_3$ (h)	*tI*8	*I*4/*mmm*	DO_{22}	$TiAl_3$ (h)
$TiAl_3$ (l)	*tI*32	*I*4/*mmm*	-	$TiAl_3$ (l)
FeAl (α_2)	*cP*2	$Pm\bar{3}m$	*B*2	CsCl
Fe_3Al	*cF*16	$Fm\bar{3}m$	DO_3	BiF_3
$FeAl_2$	*aP*18	*P*1	-	$FeAl_2$
Fe_2Al_5	*oC**	*Cmcm*	-	Fe_2Al_5
$Fe_4Al_{13}(FeAl_3)$	*mC*102	*C*2/*m*	-	Fe_4Al_{13}
Al_2FeTi (τ_2)	*cF*116	$Fm\bar{3}m$	*D*8*a*	$Mn_{23}Th_6$
τ_2*	*tP**		-	-
Al_8FeTi_3 (τ_3)	*cP*4	$Pm\bar{3}m$	$L1_2$	$AuCu_3$

3.2.2. Fe-Si-Ti

Previous studies on the ternary system Fe-Si-Ti were done by Vogel and Schlüter, who investigated the iron-rich corner. They reported two ternary phases with the composition FeSiTi and Fe_7Si_6Ti **[37]**. An early isothermal section at 800 °C was given by Markiv et al., as shown in Fig. 4. It depicts five ternary compounds: $TiFeSi_2$, $Ti_{46}Fe_{10}Si_{44}$ (X'), $Ti_{45}Fe_{15}Si_{40}$ (X"), $Ti_{12}Fe_{52}Si_{36}$ (τ_3) and the already known FeSiTi. Furthermore, tests on the solid solutions were performed by Markiv et al. The Laves phase Fe_2Ti displays a homogeneity range up to 27 at.% Si. The solubilities of Fe in Ti_5Si_3 are expected to be about 4 at.%, the one for Ti in α-Fe 2-3 at.%. The crystal structure of FeSiTi and $TiFeSi_2$ were determined by X-ray structural analysis of single crystals to be orthorombic with a = 6.24 Å, b = 9.53 Å, c = 8.56 Å for $TiFeSi_2$ and hexagonal with a = 6.24 Å, c = 6.96 Å for FeSiTi. Markiv et al. supposed that τ_3 has a hexagonal structure. Therefore, the positions and relative intensities of the X-ray results were compared to the compound τ_3 in the Ti-Co-Si and the Ti-Ni-Si system **[38]**. A reinvestigation of the FeSiTi crystal structure was done by Jeitschko, who described an orthorhombic unit cell of the space group *Ima2* with the lattice parameters a = 6.997 Å, b = 10.830Å and c = 6.287Å **[39]**.

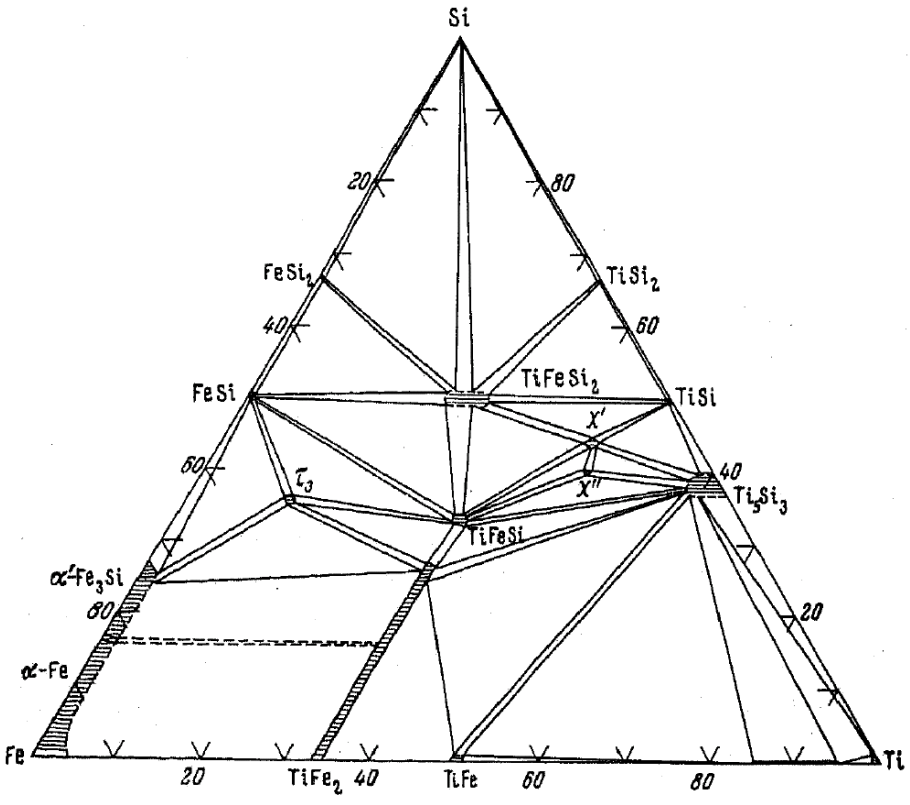

Fig. 4: Isothermal section of the system Fe-Si-Ti at 800 °C, done by Markiv [38].

A new structural report for $FeSi_2Ti$ was given by Steinmetz et al., in which it was determined to be of $MnSi_2Ti$-type, with the space group *Pbam* **[40]**. Weitzer et al. reported a hexagonal $Pd_{40}Sn_{31}Y_{13}$-structure type for the phase τ_3 (Fe_4Si_3Ti) with the space group *P6/mmm* **[41]**.

Löffler reinvestigated the ternary phase diagram for concentrations above 40 at.% Si by XRD and EPMA and presented three isothermal sections at 800°C, 900°C and 1000 °C **[12]**. A further investigation of the Fe-Si-Ti system, including an isothermal section at 900 °C, a liquidus projection and a reaction scheme, was given by Weitzer et al. **[41]**. For this work, the isotherm section at 900°C, as shown in Fig. 5, was taken.

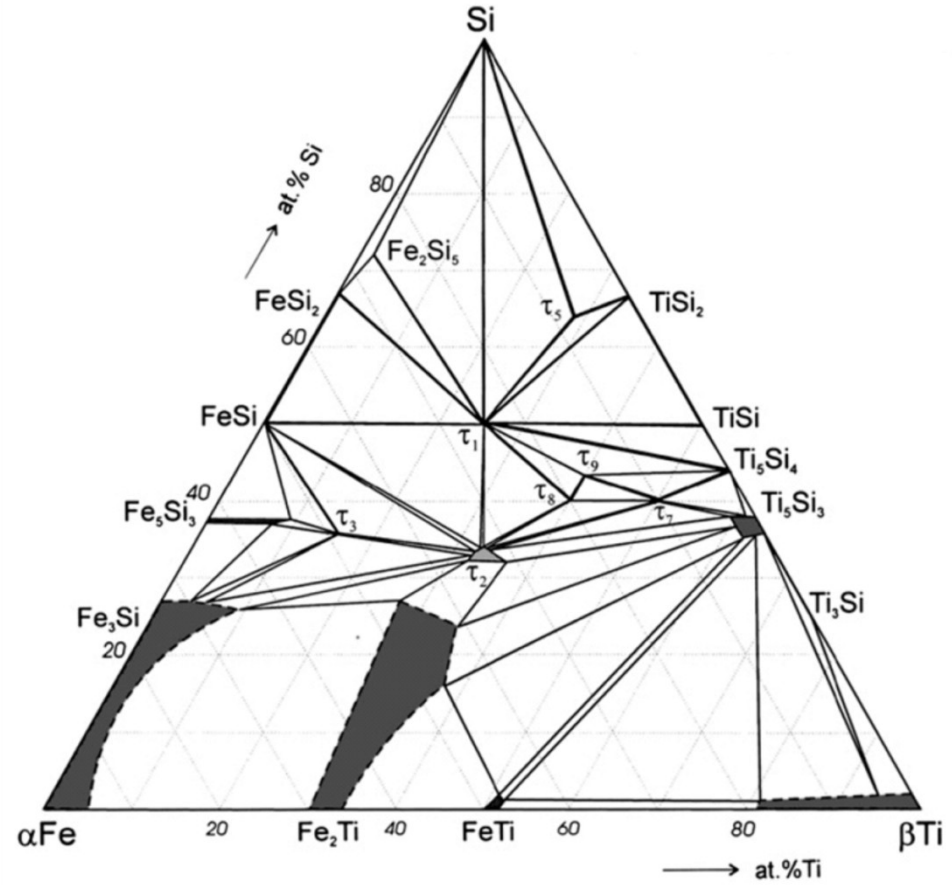

Fig. 5: Isothermal section of the system Fe-Si-Ti at 900 °C, done by Weitzer et al. [41].

The isothermal section at 900 °C shows seven ternary compounds. Thereby, only FeSiTi (τ_2) exists a homogeneity range of more than 1 at.%. Weitzer et al. reported a solubility of Si in Fe_2Ti (Laves-Phase) of more than 25 at.%. Fe_5Si_3 shows a solubility of 9.5 at.% Ti. The solubility of Ti in FeSi was found to be 1 at.%. The A2/B2/DO_3 phase field

depicts a maximum solubility of 9 at.% Ti **[41]**. The relevant crystal structure data for the ternary system Fe-Si-Ti are listed in Table 8 and 9.

Table 8: Crystal structure data of the binary Si-Ti and Fe-Si phase diagram [25].

Phase	Pearson symbol	Space group	Strukturbericht designation	Prototype
βTi	*cI*2	$Im\bar{3}m$	*A*2	W
Ti_3Si	*tP*32	$P4_2/n$	…	PTi_3
Ti_5Si_3	*hP*16	$P6_3/mcm$	$D8_8$	Mn_5Si_3
Ti_5Si_4	*tP*36	$P4_12_12$	…	Si_4Zr_5
TiSi	*oP*8	*Pmm*2	…	SiTi
	*oP*8	*Pnma*	*B*27	FeB
$TiSi_2$	*oF*24	*Fddd*	*C*54	$TiSi_2$
(Si)	*cF*8	$Fd\bar{3}m$	*A*4	C(diamond)
αFe	*cI*2	$Im\bar{3}m$	*A*2	W
α_2	*cP*2	$Pm\bar{3}m$	*B*2	CsCl
α_1	*cF*16	$Fm\bar{3}m$	DO_3	BiF_3
Fe_2Si	*hP*6	$P\bar{3}m1$	…	…
Fe_5Si_3	*hP*16	$P6_3/mcm$	$D8_8$	Mn_5Si_3
FeSi	*cP*8	$P2_13$	*D*20	FeSi
$\beta FeSi_2$	*tP*3	*P*4/*mmm*	…	…

Table 9: Crystal structure data and measured compositions of the ternary phases in Fe-Si-Ti [41].

Phase	Space group	Prototype	EDX data (at.%)		
			Fe	Si	Ti
τ_1-$FeSi_2Ti$	*Pbam*	$MnSi_2Ti$	24-25	49-50	25-26
τ_2-FeSiTi	*Ima*2	FeSiTi	31-33	33-35	33-35
τ_3-$Fe_{40}Si_{31}Ti_{13}$	*P*6/*mmm*	$Pd_{40}Sn_{31}Y_{13}$	49	35.5	15.5
τ_4	unknown	-	28	45.6	26.3
τ_5	unknown	-	7.4	64.3	28.3
τ_6	unknown	-	~12.5	~49	~38.5
τ_7	unknown	-	10	40	50
τ_8	unknown	-	20	40	40
τ_9	unknown	-	17	43	40

3.3. Quaternary system Al-Fe-Si-Ti

A limited number of literature data on the quaternary system Al-Fe-Si-Ti is available. Zakharov et al. reviewed the aluminium-rich corner, containing information in the concentration area of 10-14 at.% Si, 0-3 at.% Fe and 0-0.6 at.% Ti studied by DTA from 550 to 850 °C **[42]**. The iron-rich corner was investigated by Marker et al. at 900 °C. Thereby, three partial isothermal sections at 50 (Fig. 6), 60 (Fig. 7) and 70 at.% Fe were reported **[10]**. The single phase fields Fe_2Ti and $B2/DO_3$ were described in every section. At 50 and 60 at.% Fe the Laves phase ranges continuously from the ternary Fe-Si-Ti to the ternary Al-Fe-Ti system. Based on experimental data a large homogeneity range of the single phase field Fe_2Ti towards the titanium-poor side of the quaternary system was assumed. Thereby, two- and three-phase field samples showed titanium concentrations for the Laves phase Fe_2Ti up to 19 at.%. This observation was the reason for the investigation of the homogeneity range of the Laves phase Fe_2Ti towards the Ti-poor side of the quaternary system Al-Fe-Si-Ti. Therefore, three partial isothermal sections at 20, 25 and 33.3 at.% Ti at 900 °C were investigated.

Moreover, several two-phase and three-phase fields were shown in every section at the different iron concentrations. Also four-phase fields were obtained. A quaternary phase has not been reported so far **[10]**.

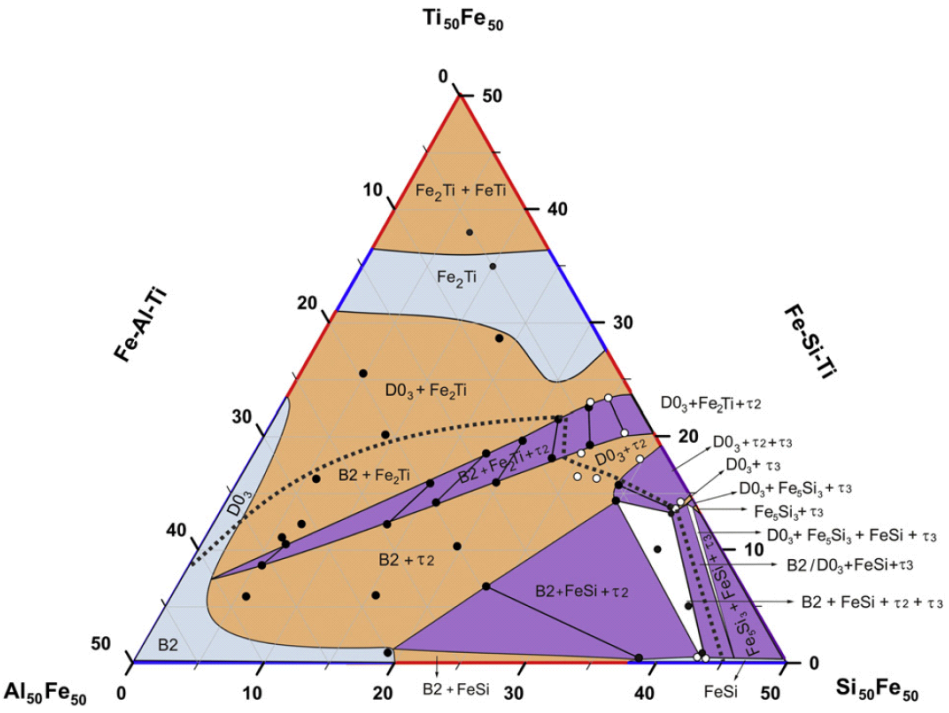

Fig. 6: Isothermal section at 50 at.% Fe of the Al-Fe-Si-Ti system at 900 °C, done by Marker et al. [10].

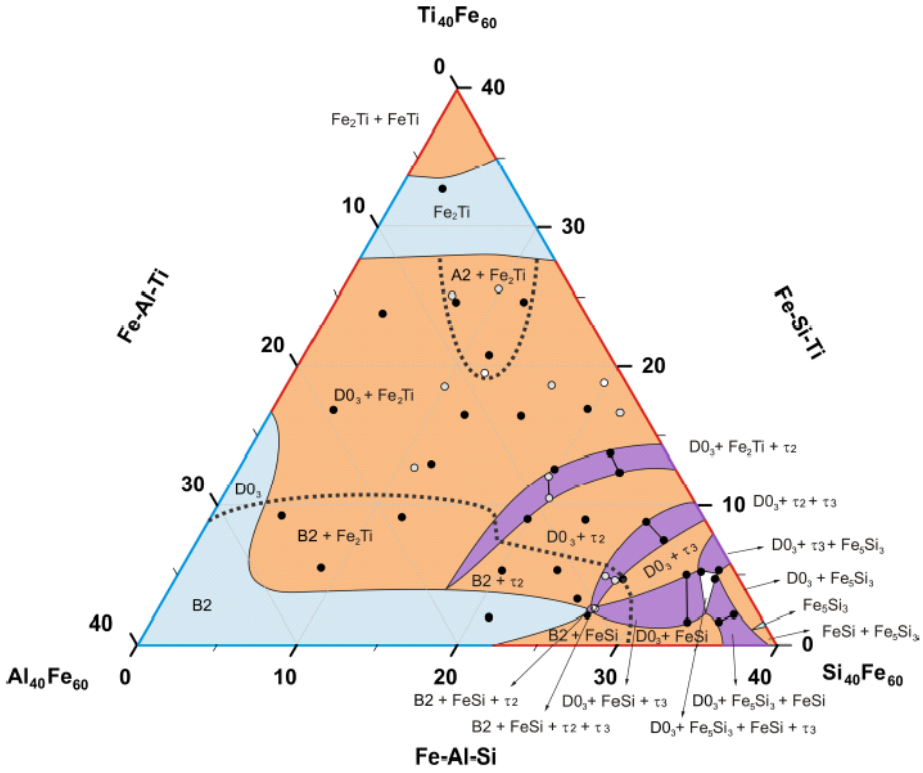

Fig. 7: Isothermal section at 60 at.% Fe of the Al-Fe-Si-Ti system at 900 °C, done by Marker et al. [10].

Furthermore, three partial liquidus projections at 50, 60 and 70 at.% Fe were given by Marker et al. Based on DTA data also certain vertical sections at constant iron concentrations have been presented **[9]**. A reinvestigation of the aluminium-rich corner of the quaternary system Al-Fe-Si-Ti was done by Li et al. Two isotherm section at 75 and 90 at.% Al were presented at 700 °C. Five four-phase fields at 75 at.% Al and two four-phase fields at 90 at.% Al were identified. The existence of a new ternary or quaternary compound in this area could be excluded **[43]**.

3.4. Laves phases

Early investigations on Laves phases were done by Friauf, Laves and Schulze **[44-48]**. The crystal structure of $MgZn_2$was first studied by Friauf in 1927 **[44]**. Laves gave the first overview containing properties and characteristics of this class of alloys **[45-47]**. It was Schulze **[48]** who introduced the term 'Laves Phase', which is commonly used today.

Up to date, more than 1400 binary and ternary Laves phases are known. Consequently, the Laves phases represent the largest group of intermetallic compounds **[1]**. Due to the fact that they are candidates for several functional as well as structural applications, a renewed interest in Laves phases started at the beginning of the 90's **[1, 4]**. Their non-structural applications are the utilization as wear resistance, super-conducting magnets or as hydrogen storage materials **[4]**. The last mentioned application plays a major role in the future development of rechargeable nickel-metal hydride batteries **[2, 3]**. For structural applications the high strength up to high temperatures is utilized. At ambient temperature the Laves phases show an enormous brittleness; its improvement was investigated by addition of ductile phases **[1]**.

Laves phases, showing topologically close-packed structures, appertain to the class of Frank-Kasper phases. They show the general composition AB_2. Thereby, the large A atoms are situated in the centre of a 16-atom polyhedron. However, the smaller B atoms occupy the centre of icosahedra. Consequently, the A atoms are coordinated by 16 (4 A and 12 B atoms), the B atoms by 12 (6 A and 6B atoms) atoms.

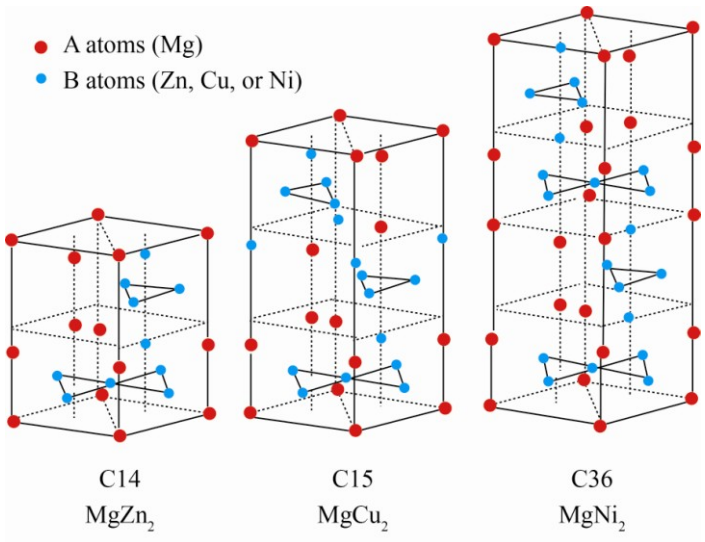

Fig. 8: Polytypes of the Laves phase structure according to Stein et al. [1].

Table 10: Crystallography of the three different Laves phase polytypes.

Polytypes	C14 type $MgZn_2$	C15 type $MgCu_2$	C36 type $MgNi_2$
Spacegroup	$P6_3/mmc$	$Fd\text{-}3m$	$P6_3/mmc$
Crystallographic positions	**Mg**: 4f (1/3, 2/3, z) **Zn**: 2a (0, 0, 0) 6h (x, 2x, 1/4)	**Cu**: 16d (5/8, 5/8, 5/8) **Mg**: 8a (0, 0, 0)	**Mg**: 4e (0, 0, z) 4f (1/3, 2/3, z) **Ni**: 4f (1/3, 2/3, z) 6g (1/2, 0, 0) 6h (x, 2x, 1/4)

Three different polytypes are described: the cubic $MgCu_2$ type (C15), the hexagonal $MgZn_2$ type (C14) and the hexagonal $MgNi_2$-type (C36). The three crystal structures exhibit a close structure relationship as shown in Fig. 8 and Table 10. The three prototypes can be built up by different stacking sequences of the same types of layers **[1]**. Furthermore, the C36-type is regarded to be an intermediate phase between the C14 and the C15-type phase **[7]**.

Specific requirements are known, which determine the stability of Laves phases. For a close-packing of spheres the radius ratio r_A/r_B has to be ≈ 1.225 (ideal radius ratio) **[1]**. Zhu et al. reported a connection between the average electron concentration factor (e/a) and the obtaining phase stability of $NbCr_2$-based Laves phases **[49]**. In this way, a designated prototype can be predicted, which, however, is not applicable for all systems **[1]**.

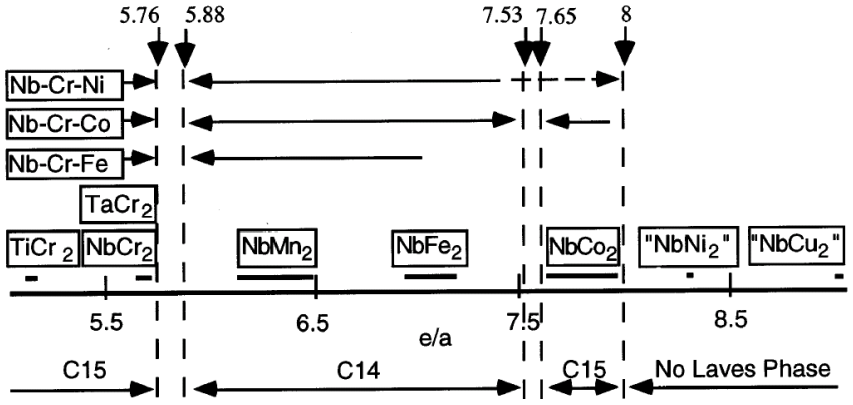

Fig. 9: Phase stability given by the average electron concentration (e/a) in $NbCr_2$-based alloys [49].

Binary Laves phases can show a large homogeneity range including the A-rich as well as the B-rich side of the stoichiometric compound **[1]**. Moreover, several binary Laves phases exhibit a large solubility of third elements without changing their crystal structure type. The

binary Laves phase (C14) Fe_2Ti shows a huge solubility for aluminium and silicon **[50]**. In case of aluminium, an increasing solubility with temperature from 33.5 at.% at 800 °C to 47 at.% at 1000 °C is reported **[11]**. Thereby, the range of solubility for titanium does not vary much. This means, confirmed by XRD investigations, that aluminium substitutes preferably for the two different iron positions **[11]**, also confirmed by Xinlin Yan et al. **[51]**. In the ternary system Fe-Si-Ti an extended homogeneity range of Fe_2Ti (C14) is described. The solid solution for silicon, which is around 27 at.%, shows a temperature independent behavior. Nevertheless, a temperature dependent solubility for titanium is reported **[12]**. The side occupancies of silicon in the Laves phase are not investigated up to now.

4. Theoretical background

4.1. Phase diagrams [52, 53, 54]

Phase diagrams are graphical representations, which describe the state of a materials system in thermodynamic equilibrium as function of temperature, pressure and composition. The phase describes a physical-homogeneous state of matter with a given chemical structure and composition. The three different states of matters solid, liquid and gaseous of a pure metal are the simplest examples.

Phase diagrams are necessary to understand the solidification processes and other reactions in order to predict the properties of materials. Important information for technical applications like welding, soldering and contacting of semiconductors can be derived from these graphical representations.

There are several reading or working rules, which have to be considered carefully. All rules in binary systems can also be applied on ternary or higher ordered systems. The foundation to understand phase diagrams is given by the Gibb's phase rule (1),

$$P + F = C + 2$$

which can be modified for condensed systems (p = constant; the pressure shows no significant effects on the equilibrium at conventional conditions):

$$P + F' = C + 1$$

P...number of phases

F...degrees of freedom; number of variables that can be varied independently

C...number of components

The Landau and Palatnik rule is necessary for construction of phase diagrams. It depicts the dimension of the borders between different phase fields and is given as: $r_1 = r - d^- - d^+$. r_1 describes the dimension of the border, r the dimension of the phase diagram. The number of phases, which are added during the transition from one phase field to another, are represented by d^+, the ones that are lost by d^-.

The Lever rule is another helpful tool for interpretation of phase diagrams. A diagram sketch, representing solid phases is given in Fig. 10. The two single phases α and β are separated by the two-phase field α+β. In this diagram, a sample with the composition C and the temperature T_1 is depicted. The composition C is located in the two-phase field α+β. By using an imaginary horizontal line (tie line), which connects the two single-phase fields through the two-phase field, the equilibrium between the both single-phase fields at the respective temperature (in this case T_1) can be described by this tie line. The Lever rule enables the determination of different αand β contributions for the compound C. (f^{α}, f^{β} = fraction of α and β, respectively).

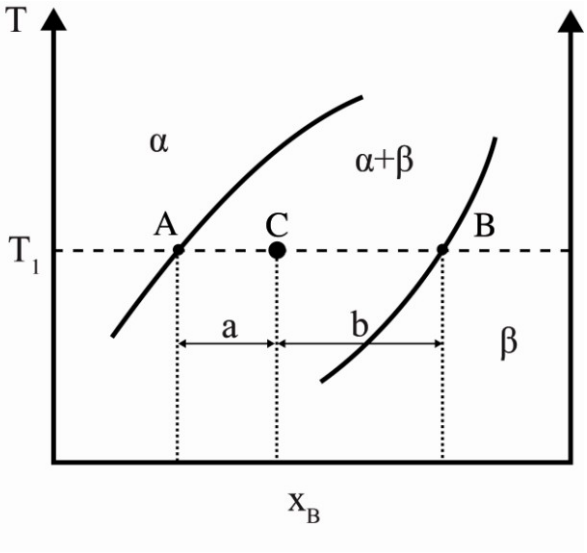

Fig. 10: Schematical depiction of the Lever rule.

$$f^{\alpha} = \frac{b}{a+b}\text{, while } f^{\beta} = \frac{a}{a+b}$$

In general, two different types of phase transformation exist. First order transformations like invariant reactions or congruent phase melting show a discontinuity of the first derivative of Gibbs energy. On the other hand, second order transformations like magnetic transformations display a discontinuity of the second derivative of Gibbs energy, the heat capacity c_p.

The one-component phase diagram, also known as unary phase diagram, can be represented as a one- or two-dimensional plot. Thereby, the behavior of an element is represented depending on temperature and/or pressure. For technical applications, phase diagrams with two or more components are in focus. In this case, the illustration of equilibrium conditions based on attendant compositions becomes more complicated. Binary phase diagrams are mostly figured as two-dimensional plots of composition and temperature at constant pressure. Ternary systems can be described by using a three-dimensional representation including the composition and the temperature at constant pressure (Fig. 11). In fact, the most ternary systems are illustrated as horizontal (isothermal) or vertical (isopleth) sections. That means that a second variable, in addition to the pressure has to be held constant.

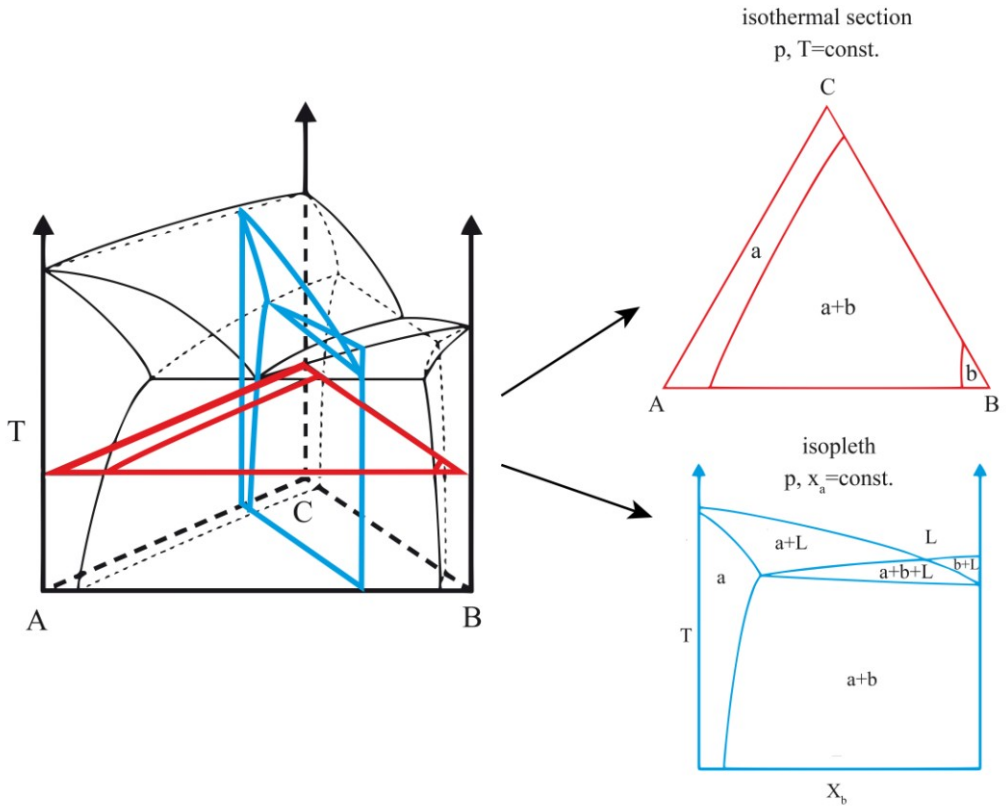

Fig. 11: Examples for an isothermal section and an isopleth in a ternary system.

Isothermal sections report the equilibrium conditions of a ternary system at constant pressure and constant temperature. Isopleths, on the other hand, show behavior of the ternary system at constant pressure and constant content of one component or constant concentration ratio of two components. Furthermore, another two-dimensional representation, the liquidus surface projection, has to be mentioned. In this case, the shape of the liquidus surface can be explained by using isothermal contour lines. In addition, various reaction paths, represented by monovariant lines, are given. Consequently, the sequences of solidification and primary crystallization fields, as well as their reaction type, can be read out.

Quaternary systems have a dependency on several variables, containing the components A, B, C and D, the pressure and the temperature. Therefore, a multidimensional representation for the equilibrium conditions is necessary. In fact, a quaternary system is represented by three variable compositions XA, XB, XC (XD= 1 – (XA+XB+XC)) and temperature. In such systems phase equilibria can be illustrated at constant temperature. By using a three-dimensional composition tetrahedron, a full isotherm section can be described. The three-dimensional order in form of a tetrahedron for a quaternary system A-B-C-D is shown in Fig. 12.

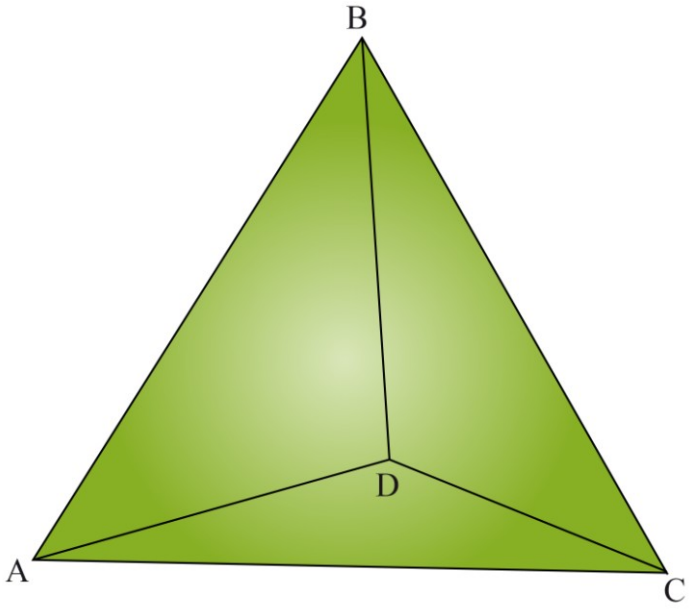

Fig. 12: Composition tetrahedron of a quaternary system A-B-C-D.

Several possibilities to present a two-dimensional section of a quaternary system are given. One example for an isothermal-isobaric section through a quaternary system is sketched in Fig. 13. A compound at x has a binary composition of 33.3 at.% B and 66.6 at.% A. All compounds along the three lines x-y, y-z and z-x are, corresponding to their binary and ternary systems, binary or ternary and the triangle x-y-z shows a composition of 33.3 at.% B.

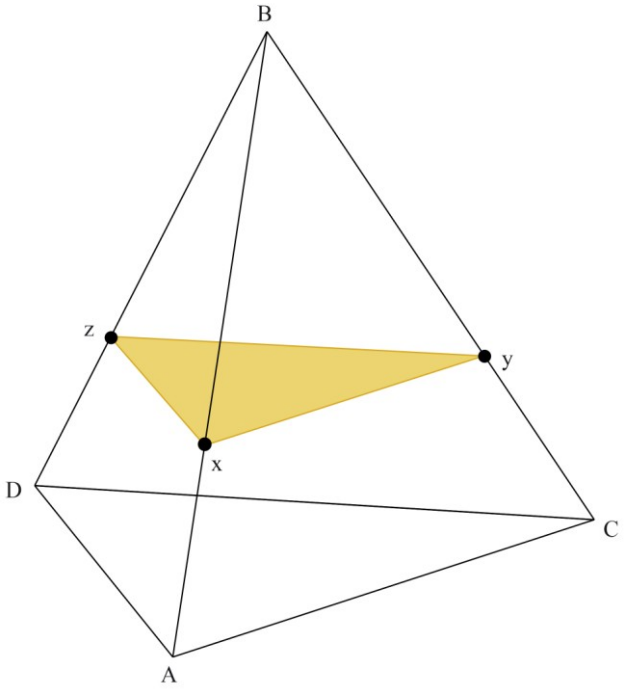

Fig. 13: Graphical representation of an intersection at 33 at.% B of a quaternary composition tetrahedron.

Two different types for a four-phase field in the plane, which basically has the form of an irregular tetrahedron, are known. One the one hand, the tetrahedron can intersect the plane section in form of a triangle, on the other hand, a quadrangular cut is possible, as shown in Fig. 14. However, the illustration of a three-phase-field in an isotherm-isobaric section in the plane is a line, the one of a two-phase field a point.

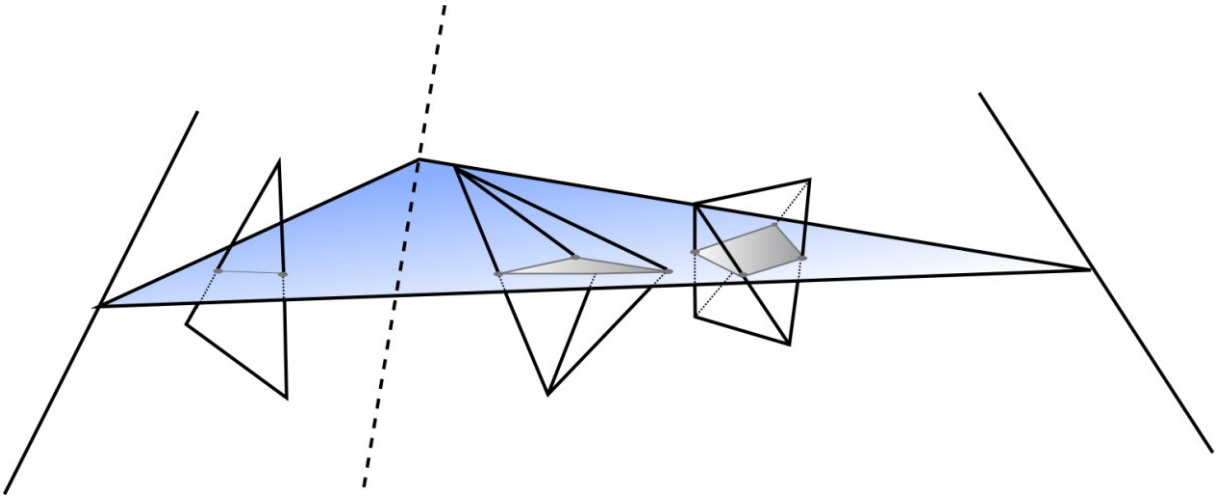

Fig. 14: Schematical representation of the intersection of a three- and four-phase equilibria with a two-dimensional section of a sketched quaternary system [53].

4.2. Methods

4.2.1. Optical microscopy [55, 56]

Reflected-light microscopy is used for magnified representation and analysis of opaque samples like metals and alloys. In general, reliable statements about the microstructure, the homogeneity of the sample, the number of phases and the relative amount of phases can be made. Furthermore, the microstructure reveals several important information (some are listed below):

- crystallization sequence
- reaction sequence and type of reactions
- grain sizes and grain size distribution
- segregation
- precipitation (solid-solid transitions)

The most common technique for investigations of microstructures is given by the bright field mode (Fig. 15). A bundle of parallel beams passes the beamsplitter. The resultant diffracted beams enter the objective, which focuses them on the sample. Reflected by the surface of the sample, the beam becomes collected back to the tube lens, where a real image is received. The contrast of this image is given based on the properties of the surface like roughness and colour.

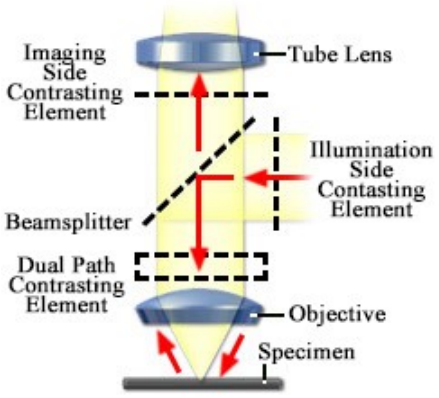

Fig. 15: Bright field imaging [56].

Reflected darkfield microscopy (Fig. 16) is used for the exploration of the relief in surfaces of materials. In this way the hardness of phases, the exist of cracks or holes as well as scratches, which occur from the surface polishing, can be observed. After passing a mirror system the beam enters a ring mirror and, subsequently, a dark channel system (objective).

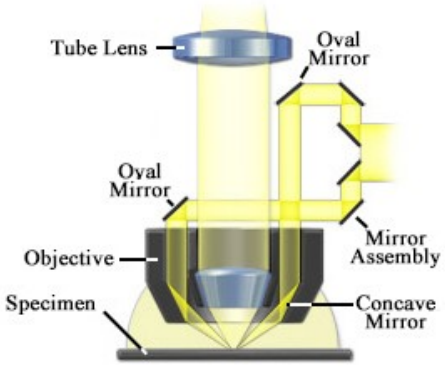

Fig. 16: Dark filed imaging [56].

Consequently, the light irradiates the surface of the sample at a low angle. Areas where scratches, cracks or holes exist, can direct the light back to the tube lens and be observed as bright fields. However, areas where the metals or alloys act as a perfect mirror (there are no surface irregularities), no light is reflected back and they appear as dark/black fields.

For studying minute elevation differences in surfaces, the differential interference contrast (DIC) mode is applied (Fig. 17). A polarized beam enters a bi-refringent prism (Nomarski prism), where it gets split into two orthogonal polarized beams. They are focused on the sample by an objective. A completely flat surface will not show any features. However, if there are minute height differences in the surface, the separated beams have different optical path lengths. After refection, the parallel beams have to pass the objective, the Nomarski prism and finally a second prism (analyzer), where interference produces a grey image, according to the optical path difference. By using a colour filter (lambda plate) the contrast can be improved.

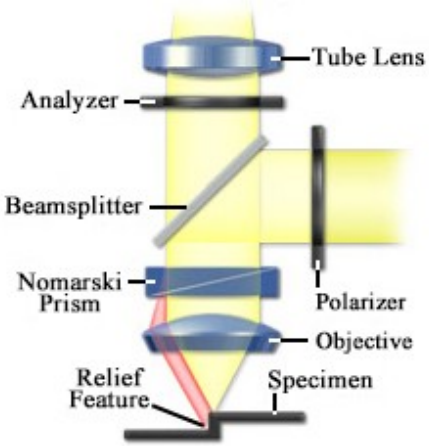

Fig. 17: DIC optics [56].

For investigation of alloys containing structures that change the state of polarization during the reflection process, the polarized reflected light microscopy is used (Fig. 18). The contrast accords to the optical properties and the orientation of the sample. In this way, it is possible to measure the grain size of polarizing phases. Furthermore, statements in terms of structure type, whether they show low or high symmetry can be discerned. In this optical configuration, the light primarily passes a polarizer. The linearly polarized light is focused on the sample surface where it is modified according to the optical properties of the material. After reflection, it enters an analyzer oriented at 90° to the polarizer. As a result, only depolarized light is able to cross the analyzer and reach the tube lens.

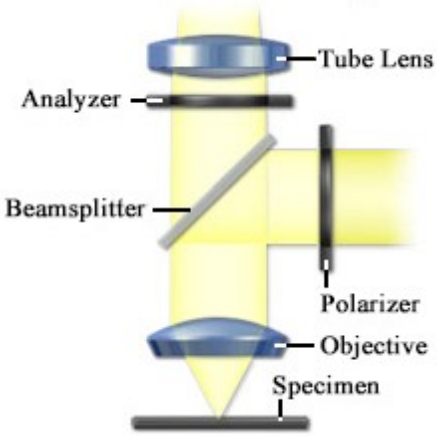

Fig. 18: Polarization optics [56].

4.2.2. Scanning electron microscopy (SEM) and electron probe microanalysis (EPMA) [55, 57]

Scanning electron microscopy (SEM) and electron probe microanalysis (EPMA) are analysis techniques that are applied for imaging of the surface as well as for qualitative and quantitative investigations of materials.

A schematic construction of a scanning electron microscope is shown in Fig. 19. In principal, electron column consists of an electron gun and several magnetic lenses, which focus the electrons through the evacuated tube on the specimen. The electrons are emitted by a heated cathode (tungsten filament or LaB_6tip) and accomplish energy in the range of 0.1-30 keV. By using electromagnetic lenses with tunable focal length, an electron beam of less than 1 μm accrues.

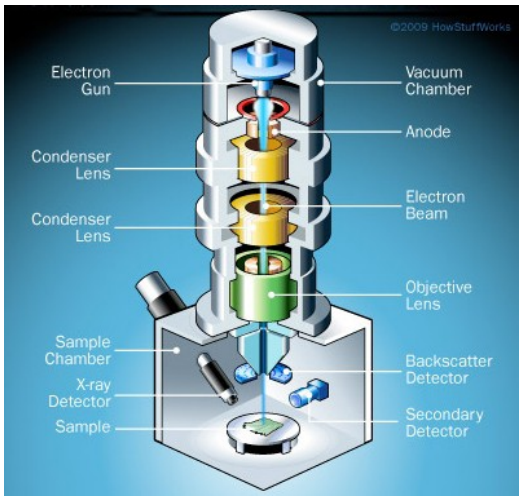

Fig. 19: Schematic construction of a SEM [58].

The interaction of the electron beam with the sample surface leads to several effects, as shown in Fig 20. The real interaction volumes for certain interactions depend on the material and the electron energy, so only a schematical sketch is presented (Fig. 20).

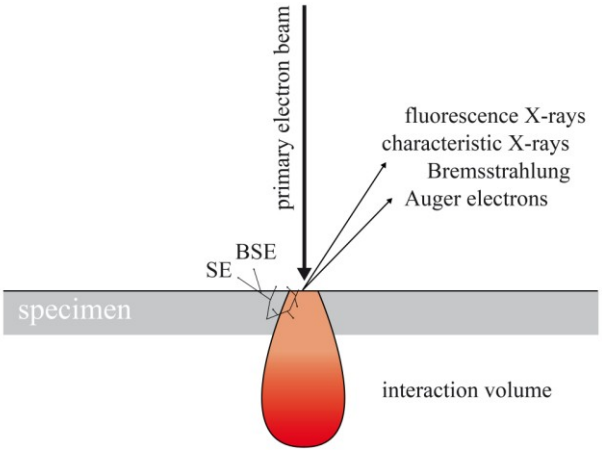

Fig. 20: Interaction of the primary electron beam with the specimen

Back scattered electrons (BSE) or secondary electrons (SE) are applied for imaging. Instead of reflected light microscopy, images with a much higher magnification and resolution are obtained by scanning the specimen surface with the electron beam line by line. Back

scattered electrons are a ‘reflector product’ of the primary electron beam. The primary electrons, thereby, interact with the high electron densities of atoms in the material. In this way, multiple elastic and inelastic scattering take place and electrons with energy of 80-90% of the primary electron beam escape. By using the BSE-mode the presence of different phases can be distinguished by different grey scales, which refers to the ‘mass contrast’. The ‘mass contrast’ is based on the back scatter coefficient which increases with increasing atomic number. Due to that fact, a phase with a large average atomic number shows a bright BSE image. This effect is decreasing for higher atomic numbers and may be overruled by the ‘orientation contrast’ for higher average atomic numbers.

Secondary electrons occur through the interactions between the primary electron beam and the slightly bound conduction band electrons in alloys or metals. According to the energy differences between the primary electrons (keV) and the specimen electrons (eV), secondary electrons (SE) are low energy electrons in the range of 3-5 eV. Consequently, they only appear in a small area near the surface. The contrast is given due to the topography of the sample surface, since more electrons can escape from edges.

By investigation of the characteristic X-ray radiation, qualitative as well as quantitative information with respect to the specimen can be obtained. Characteristic X-rays are determined by two different detection techniques. Therefore, the electron-dispersive spectroscopy (EDX) and the wavelength dispersive spectroscopy (WDX) have been established. In the EDX technique the energy of the X-ray photons (E) is counted by a solid state detector. Thereby, a photosensitive silicon layer converts the impinging photons into electron/hole pairs. The theoretical resolution for this method is given by the energy for the electron/hole formation of silicon (ε=3.8 eV). The maximum number of electron/hole pairs can be calculated by $n = E/\varepsilon$. EDX is characterized by a fast measurement time, whereby the whole X-ray spectrum is recorded simultaneously.

In WDX technique, the X-rays are monochromated by different orientated crystals. Different monochromator crystals are applied for different wavelength ranges, respectively. A conventional scintillation counter is used for processing the impinging wavelength. For detection of different wavelength, the crystal, as well as the detector, has to move along the focussing circle. Due to the fact that WDX measurements circumvent the overlap of spectral lines, a higher resolution, compared to EDX, is given. However, the movement of crystals and detector leads to a much longer measurement time.

For electron microanalysis a combination of EDX, for fast qualitative analysis and several WDX spectrometer, for simultaneous quantitative analysis of different alloys is appropriate. Therefore, calibration with standard materials has to be done. Additionally, upcoming matrix effects, which are unique for different materials, can be corrected by using the ZAF matrix correction:

$$\frac{C_x}{C_{(x)}} = [ZAF]_x \frac{I_x}{I_{(x)}} = [ZAF]_x k_x$$

$$k_x = \frac{C_x}{C_{(x)}} = \frac{I_x}{I_{(x)}}$$

C_x, $C_{(x)}$…mass concentration of x in sample or standard

I_x, $I_{(x)}$…intensity of characteristic line of x in sample or standard

Z…correction model for average atomic number of sample material

A…correction model for absorption of sample material

F…correction model for fluorescence of sample material

The mathematical correction of raw data enables quantitative data. The total weight percent, that certainly has to be around 100, is an important criterium for the quality of the measurement.

4.2.3. X-ray powder diffraction (XRD) [55, 59]

4.2.3.1. X-rays

X-rays are typically generated by using the X-ray tube, as shown in Fig. 21. By heating the cathode (also called electron gun) electrons are emitted and accelerated in an electric field (20-60 kV) to a water cooled anode, which usually consists of Cu, Co, Mo or Fe. After collision of the high-speed electrons with the anode, their kinetic is converted to X-ray radiation (less than 1%) and heat.

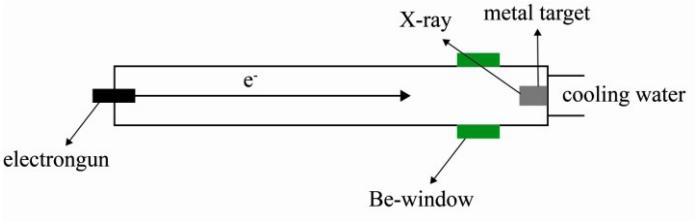

Fig. 21: Schematical depiction of an X-ray tube.

A schematic X-ray spectrum is given in Fig. 22. The X-ray spectrum shows two different phenomena, a continuous X-ray spectrum (also known as 'Bremsstrahlung' or white spectrum) and the characteristic X-ray lines. The continuous spectrum accrues from a series of collision between the bombarding electrons and the atoms of the target, whereby they lose their energy. Due to the fact that each electron loses its energy in a different way, a variety of different wavelengths results. The characteristic X-rays are obtained by an interaction of the incident electrons with the inner orbital electrons of the target atoms. A bombarding electron with adequate energy ejects an inner shell electron and creates an electron hole. This vacancies filled by an electron from an outer shell and an X-ray photon with characteristic wavelength is emitted. The energy of the X-ray is received from the difference in the electron energy levels and is a characteristic of the target material. The

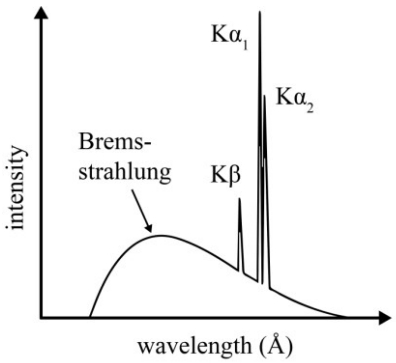

Fig. 22: X-ray spectrum.

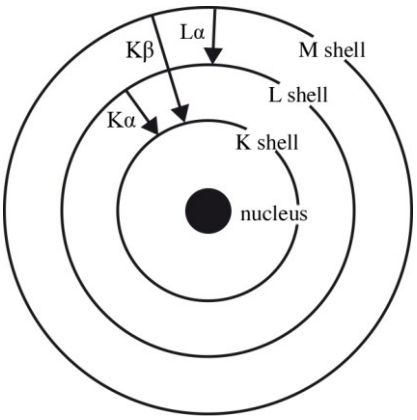

Fig. 23: Electron transition [59].

different characteristic X-ray lines are consistent with the electron transitions between different energy levels (Fig. 23). According to the Bohr model, all transitions that end at the K-shell are described as K with the footnote α, β etc., corresponding to the type of transition. K_α lines, thereby, arise from a transition of the L-shell to the K-shell, whereas K_β is referable to a transition of the M-shell. Based on the subshells, which exist in every shell expect the K-shell, the K_α splits up into two separate lines, the $K_{\alpha1}$ and the $K_{\alpha2}$. $K_{\alpha1}$ is emitted by the transition of the L_{III} to the K shell, however, $K_{\alpha2}$ results from the transition of L_{II}.

4.2.3.2. X-ray diffraction

If an isolated atom is hit by X-ray radiation, elastical scattering can be observed. This characteristic is based on the absorption and reemission of electromagnetic radiation, whereby the energy remains constant. The electrons around the nucleus are accounted for this phenomenon. When X-ray radiation gets scattered on the high electron densities of the atom, constructive interference can be observed, producing a diffracted beam. In crystalline solid the atoms can be counted as scattering centres. A crystal can be described as a grating, which is made up of atomic layers with a designated distance *d*. These layers correspond to the crystallographic planes, described by the Miller Indices *h, k* and *l*. For every crystal structure only one possibility, how the atoms and the appropriated lattice planes are ordered, exist. Diffraction occurs, if the distance of the gridlines in gratings is in the order of magnitude of the wavelength of X-ray radiation. A sketch for the interaction of X-rays with a crystalline solid is given in Fig. 24.

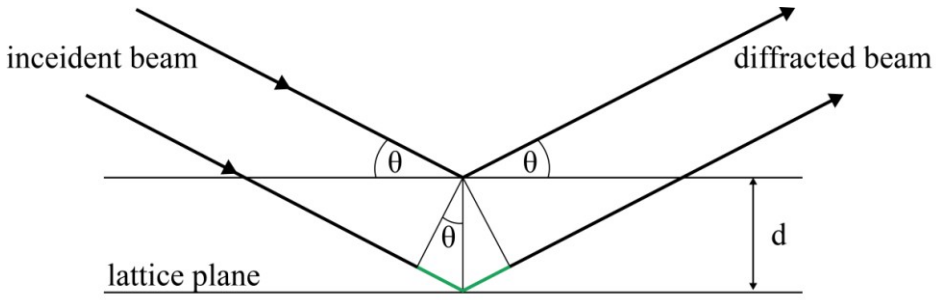

Fig. 24: Sketch of X-ray diffraction (Bragg-construction).

The two different X-rays, as shown in Fig. 24, have a different travelling path. The distance for one of them is about the green section larger, compared to the other one. If the green section is an integer multiple of the applied X-ray wavelength, constructive interference occurs and the diffracted beam can be detected. Different diffracted wavelengths from

different atomic lattice planes form a definite diffraction pattern that comprises information about the crystal structure. The geometrical construction in Fig. 24 leads to the Bragg equation:

$$2d_{hkl} \bullet sin\Theta = n\lambda$$

d is the distance between the crystallographic planes (*h,k,l*), Θ the angel of the incident beam, n is an integer and λ the wavelength of the incident X-ray. Positive inference and, consequently, diffraction can only be observed for radiation, which hits the plan in a uniquely defined angle, the Bragg angle. By measuring the angle Θ the distance between two atomic layers can be calculated, if the wavelength λ is already known.

The intensity of the diffracted X-rays is dependent on the atoms in the unit cell and is expressed by the structure factor F:

$$I_{hkl} \propto |F_{hkl}|^2$$

$$\text{full model: } I_{hkl} = |F_{hkl}|^2 \cdot p \cdot \left(\frac{1+cos^2 2\Theta}{sin^2\Theta cos\Theta}\right) \cdot e^{\frac{-B\, sin^2\Theta}{\lambda^2}}$$

F_{hkl}...structure factor

p…multiplicity factor

$\left(\frac{1+cos^2 2\Theta}{sin^2\Theta cos\Theta}\right)$:..Lorentz polarization factor

$e^{\frac{-B\, sin^2\Theta}{\lambda^2}}$…temperature factor

The structure factor contains the structure information appropriated to:

$$F_{hkl} = \sum_j f_j \cdot e^{2\pi i(hx_j + ky_j + lz_j)}$$

f_j represents the scattering factor of the atom j, occupying the positions x_j, y_j, and z_j. *h,k* and *l* correspond to the Miller indices of the reflection. The scattering factor depends on the atomic number, or rather the number of electrons of the atom, the wavelength λ and the diffraction angle Θ. It describes the efficiency of scattering of a single atom and can be defined as:

$$f = \frac{Amplitude\ of\ wave\ scattered\ by\ an\ atom}{Amplitude\ of\ wave\ scattered\ by\ one\ electron}$$

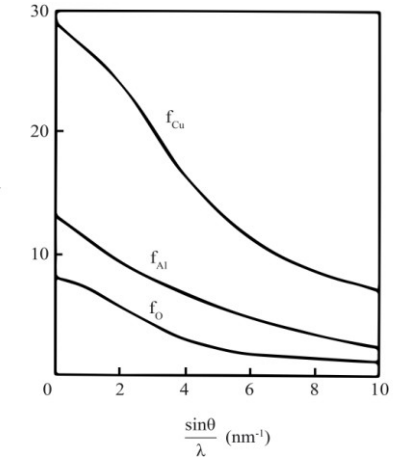

Fig. 25: Dependence of *f* on the scattering angle [59].

When the angle Θ=0, the scattering factor corresponds to the atomic number (*f*=Z), or rather to the total number of electrons. *f* is increasing with increasing atomic number and decreasing with increasing angle.

4.2.3.3. X-Ray Powder Diffraction

The instrumental setup of an X-ray powder diffractometer generally consists of an X-ray source, a specimen and X-ray detector, which are all disposed on a circumference of a circle, known as focusing circle. The Bragg-Brentano pseudo-focusing geometry enables two different measurement-methods. The most common one is the Θ/2Θ geometry, where the X-ray source is fixed while the detector and the specimen are moving simultaneously (see Fig. 26a.). If the specimen moves for an angle of Θ, the detector has to move 2Θ. On the other hand, by working with the Θ/Θ geometry, the specimen holder is fixed and the X-ray source, as well as the detector, has to move.

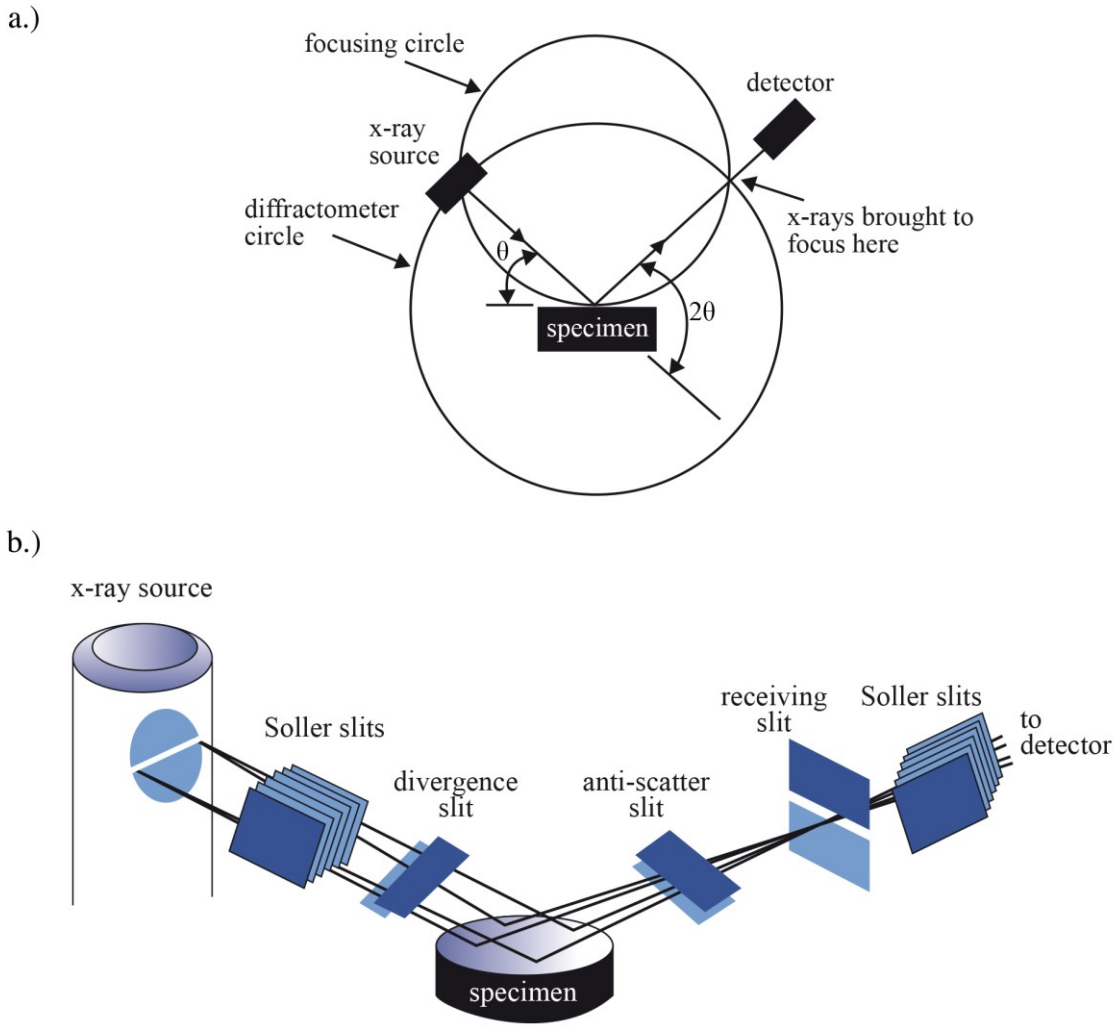

Fig. 26: a.) Θ/2Θ-geometry of an X-ray diffractometer; b.) Slits set-up of an X-ray diffractometer [59].

The incedent X-rays have to pass a number of slits before they hit the specimen, see Fig. 26b. The Soller slits are a series of closely spaced parallel metal plates, usually made of tantalum or molybdenum. In this way, the X-rays get define and collimate. A divergence slit confines the divergence of the incident radiation. After diffraction by the specimen, the X-rays pass another set of slits. The antiscatter slit improves the peak/background ratio. A receiving slit defines the width of the diffracted X-rays. Before the X-rays reach the detector, they have to pass another set of Soller slits and finally, if necessary a K_β radiation filter. The most common detectors are the scintillation counter, the energy dispersive solid state detector and the one dimensional or strip detector. The scintillation counter is based on the detection of fluorescence, which occur from the interaction between the incident X-rays with a Tl doped NaCl crystal. Incident X-ray photons thereby produce a flash of light in the visual range. The X-ray intensity is proportional to the amount of emitted light and is measured by a photomultiplier. Energy dispersive solid state detectors are based ona photosensitive silicon layer, where the impinging X-rays are converted into electron/hole pairs. The charge generated in the detector is proportional to the energy of the incident X-ray photons. The theoretical resolution for this method is given by the energy for the electron/hole formation of silicon (ε=3.8 eV). The one dimensional detector is given by a series of small strip detectors arranged along a line. A certain angel can be detected simultaneously by adding the signals of the different strips (increment: 0.01°), while the detector is moving on the circle.

4.2.3.4. Rietveld refinement

A powder X-ray diffraction pattern is represented as a two dimensional plot showing the intensity as a function of the diffraction angle. The main information can be read out of the position of the peaks, which depends on the unit cell dimensions and the intensity of the diffraction lines, that correspond to the atomic number, the occupation of lattice sites and etc., already discussed in 4.2.3.2.

To identify the phases of a measured pattern, their diffraction lines have to be compared with already known structure data from literature. By using the Rietveld refinement the calculated diffraction pattern can be fitted to the measured one. The Rietveld refinement is a mathematical method, which describes the whole pattern using structure-, profile- and instrument-related parameters. In a least square process, the calculated and the observed intensities were compared, using the quantity:

$$\chi_1^2 = \frac{\sum_i w_i \, (y_{oi} - y_{Ci})^2}{\sum_i w_i \, y_{oi}}$$

y_{Oi} is the observed and y_{Ci} the calculated intensity at the point *i;* w_i is a weight factor. The calculated intensity y_{Ci} is given by a function containing information about the background and terms with phase specific as well as instrument parameters:

$$y_{Ci} = y_{Bi} + S \cdot \sum_{hkl} |F_{hkl}|^2 \cdot p \cdot \left(\frac{1 + cos^2 2\theta_i}{sin^2 \theta_i cos\theta_i} \right) \cdot e^{\frac{-2Bsin^2\theta}{\lambda^2}} \cdot \Phi(2\theta_i - 2\theta_{hkl}) \cdot P_{hkl} \cdot A \cdot S_r \cdot E$$

S…scaling factor (for each phase)

Y_{Bi}…background at I

P_{hkl}…factor for the preferred orientation

S_r…function for surface roughness

A…absorption function

E…extinction factor

Φ…profile factor

The quality for a Rietveld refinement can be checked by the so called R-value. A smaller R-value corresponds to a better fitting between the observed and the calculated pattern. The weighted pattern R_{wp} is given as:

$$R_{wP} = \sqrt{\frac{\sum_i w_i \left| (y_{Oi} - y_{Ci}) \right|^2}{\sum_i w_i \, y_{Oi}^2}}$$

5. Experimental

5.1. Sample preparation

5.1.1. Sample selection

Based on the given work by Marker et al. **[10]**, where a large homogeneity range of Fe_2Ti towards the Ti-poor side was reported, three partial isothermal sections at 20, 25 and 33.3 at.% Ti at 900 °C were investigated. Thereby, the sample compositions were selected according to their **[10]** observed results and the homogeneity ranges for Fe_2Ti of the corresponding ternary systems, with the aim, to characterize the phase boundary of Fe_2Ti in the Al-Fe-Si-Ti system **[36, 41]**. Furthermore, samples in the Fe-Si-Ti system have been prepared to investigate the dependence of the site occupancies on the composition for Fe_2Ti by addition of Si as well as the behavior of the lattice parameters. To check the phase-equilibria on the Ti-rich side of the Laves phase in the Fe-Si-Ti system and to characterize $Fe_{10}Si_{40}Ti_{50}$ and $Fe_{20}Si_{40}Ti_{40}$, further samples were prepared. All sample compositions are given in Table. 11, Fig. 27 and Fig 28. The following basic materials have been used:

-Aluminium slug, 3.175 mm x 6.35 mm, 99.999%, Alfa Aesar

-Iron sheet, 0.5 mm, 99.95%, Fa. Johnson Matthey Chemicals

-Silicon lump, 0.1-2,5 cm, 99.9999%, Alfa Aesar

-Titanium rod, 6.4 mm x 25 cm, 99.7%, Alfa Aesar

The basic materials have been weighted with a semi-micro balance to a total sample mass of 1000 mg, except the sample PB058i (800 mg). Thereby, an error of ±0.5 mg and ±0.1 at.% was observed.

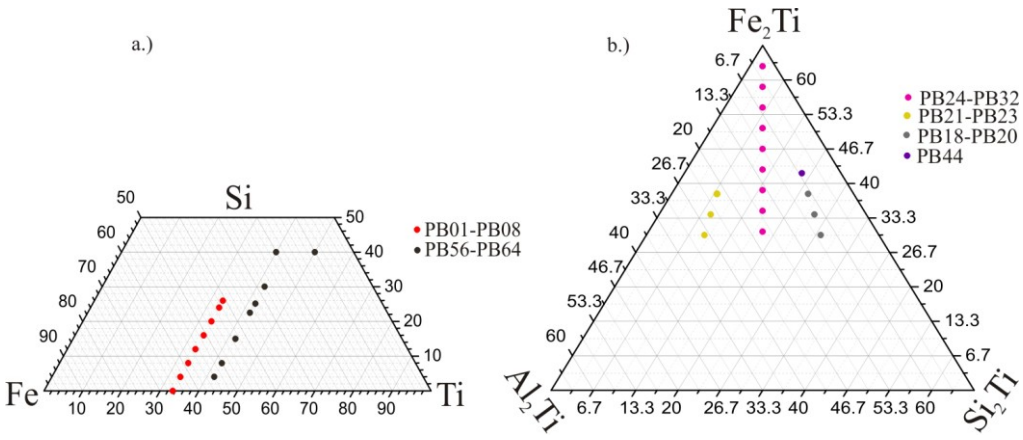

Fig. 27: Graphical representation of prepared samples in the Fe-Si-Ti system (a) and the 33.3 at% Ti section of the quaternary system Al-Fe-Si-Ti. The marking of graphic b.) was done by rounded figures.

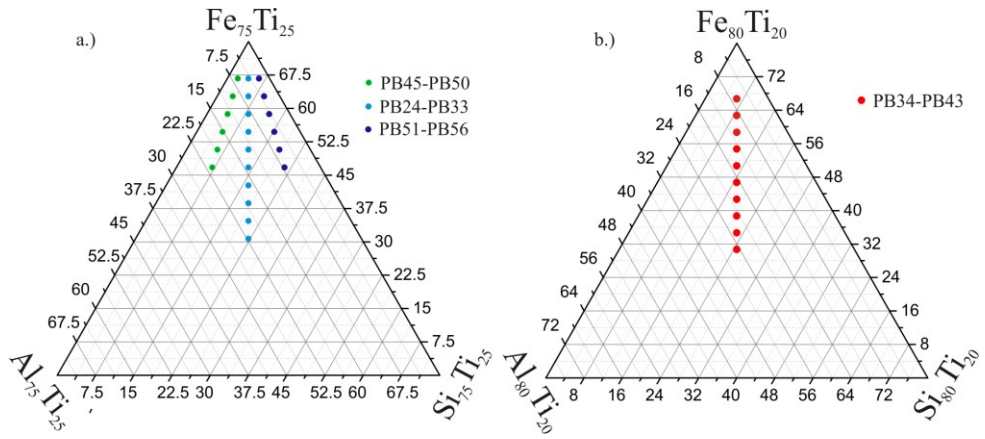

Fig. 28: Graphical representation of prepared samples at the 20 and 25 at.% Ti sections of the Al-Fe-Si-Ti system.

Table 11: Nominal and real composition of prepared samples.

Sample	Nominal composition (at.%)				Real composition (at.%)				Total mass (mg)
	Al	Fe	Si	Ti	Al	Fe	Si	Ti	
PB01	-	66.7		33.3	-	66.74		33.26	1000
PB02	-	62.7	4	33.3	-	62.75	3.95	33.30	1000
PB03	-	58.7	8	33.3	-	58.72	8.04	33.34	1000
PB04	-	54.7	12	33.3	-	54.74	12.09	33.33	1000
PB05	-	50.7	16	33.3	-	50.72	16.03	33.26	1000
PB06	-	46.7	20	33.3	-	46.73	20.02	33.31	1000
PB07	-	42.7	24	33.3	-	42.70	24.00	33.33	1000
PB08	-	40.7	26	33.3	-	40.67	26.02	33.32	1000
PB09	2	62.7	2	33.3	2.04	62.69	2.06	33.35	1000
PB10	4	58.7	4	33.3	4.02	58.72	4.03	33.29	1000
PB11	6	54.7	6	33.3	6.04	54.74	5.95	33.34	1000
PB12	8	50.7	8	33.3	7.99	50.66	7.98	33.33	1000
PB13	10	46.7	10	33.3	10.00	46.73	9.99	33.34	1000
PB14	12	42.7	12	33.3	12.04	42.70	12.00	33.34	1000
PB15	14	38.7	14	33.3	14.06	38.73	13.96	33.34	1000
PB16	16	34.7	16	33.3	15.94	34.73	15.99	33.34	1000
PB17	18	30.7	18	33.3	18.01	30.73	17.99	33.35	1000
PB18	7.175	38	21.525	33.3	7.210	38.01	21.571	33.26	1000
PB19	8.175	34	24.525	33.3	8.196	34.03	24.601	33.28	1000
PB20	9.175	30	27.525	33.3	9.207	29.98	27.539	33.32	1000
PB21	21.525	38	7.175	33.3	21.581	37.98	7.248	33.29	1000
PB22	24.525	34	8.175	33.3	24.460	33.98	8.208	33.28	1000
PB23	27.525	30	9.175	33.3	27.476	30.04	9.206	33.34	1000
PB24	4.15	66.7	4.15	25	4.19	66.70	4.20	24.98	1000
PB25	6.15	62.7	6.15	25	6.12	62.71	6.21	24.97	1000
PB26	8.15	58.7	8.15	25	8.15	58.72	8.16	25.03	1000
PB27	10.15	54.7	10.15	25	10.07	54.70	10.16	24.97	1000

Sample	Nominal composition (at.%)				Real composition (at.%)				Total mass (mg)
	Al	Fe	Si	Ti	Al	Fe	Si	Ti	
PB28	12.15	50.7	12.15	25	12.17	50.71	12.07	25.00	1000
PB29	14.15	46.7	14.15	25	14.19	46.73	14.16	24.98	1000
PB30	16.15	42.7	16.15	25	16.12	42.72	16.17	24.99	1000
PB31	18.15	38.7	18.15	25	18.21	38.68	18.16	25.04	1000
PB32	20.15	34.7	20.15	25	20.10	34.73	20.18	24.99	1000
PB33	22.15	30.7	22.15	25	22.09	30.70	22.18	25.04	1000
PB34	6.65	66.7	6.65	20	6.68	66.81	6.64	20.02	1000
PB35	8.65	62.7	8.65	20	8.71	62.70	8.70	20.04	1000
PB36	10.65	58.7	10.65	20	10.64	58.70	10.61	19.95	1000
PB37	12.65	54.7	12.65	20	12.68	54.70	12.72	19.96	1000
PB38	14.65	50.7	14.65	20	14.62	50.71	14.64	20.04	1000
PB39	16.65	46.7	16.65	20	16.72	46.69	16.66	19.98	1000
PB40	18.65	42.7	18.65	20	18.63	42.75	18.68	19.99	1000
PB41	20.65	38.7	20.65	20	20.69	38.72	20.62	19.97	1000
PB42	22.65	34.7	22.65	20	22.66	34.71	22.69	20.03	1000
PB43	24.65	30.7	24.65	20	24.61	30.70	24.64	19.96	1000
PB44	6.175	42	18.525	33.3	6.18	42.03	18.56	33.30	1000
PB45	6.225	66.7	2.075	25	6.287	66.71	2.071	25.02	1000
PB46	9.225	62.7	3.075	25	9.235	62.70	3.063	24.99	1000
PB47	12.225	58.7	4.075	25	12.271	58.72	4.108	25.03	1000
PB48	15.225	54.7	5.075	25	15.236	54.71	5.107	24.98	1000
PB49	18.225	50.7	6.075	25	18.241	50.71	6.130	25.04	1000
PB50	21.225	46.7	7.075	25	21.254	46.70	7.090	25.04	1000
PB51	2.075	66.7	6.225	25	2.085	66.73	6.254	25.01	1000
PB52	3.075	62.7	9.225	25	3.068	62.70	9.248	25.00	1000
PB53	4.075	58.7	12.225	25	4.068	58.71	12.233	25.00	1000
PB54	5.075	54.7	15.225	25	5.084	54.67	15.271	24.97	1000
PB55	6.075	50.7	18.225	25	6.080	50.71	18.299	24.99	1000
PB56	7.075	46.7	21.225	25	7.043	46.72	21.259	25.01	1000
PB57	-	10	40	50	-	10.01	39.95	50.00	1000
PB58	-	20	40	40	-	20.01	39.97	39.97	1000
PB58i	-	20	40	40	-	19.99	40.08	39.98	800
PB59	-	54	4	42	-	54.02	4.04	42.01	1000
PB60	-	50	8	42	-	49.97	8.01	42.03	1000
PB61	-	43	15	42	-	43.02	15.05	42.02	1000
PB62	-	35.5	22.5	42	-	35.51	22.53	42.01	1000
PB63	-	33	25	42	-	33.02	25.07	42.02	1000
PB64	-	28	30	42	-	28.01	29.96	42.01	1000

*Calculated from the weighted masses of each sample.

5.1.2. Arc furnace

All weighted samples were molten in an arc furnace (Johanna Otto GmbH, model: MAM 1), shown in Fig. 29. The main setup is given by a cylindrical chamber, which basically consists of two electrodes at the ends. The first one is represented by a thorium oxide doped tungsten tip at the top, which functions as anode. On the other side, a cooled copper plate serves as cathode. Additionally, an argon connection (argon 5.0, >99.999 Vol.%) as well as a vacuum pump entry are applied to remove oxygen and to provide a protective gas. By touching a tungsten-rod with the tungsten tip, situated at the cooled copper plate, the arc ignites. Temperatures up to 3000°C can be reached, regulated by the input current. A zirconium pearl primarily was molten to ensure that also the last oxygen traces were removed and that oxidation during the melting process of the samples can be excluded. Afterwards the weighted elements, which were situated in indentations on the copper plate, were fused to pills. Each sample was molten twice, whereby they were turned upside-down, just to ensure that the distribution of the components in the sample is homogenous. After every melting step the samples were checked for mass losses.

Fig. 29: Arc furnace.

5.1.3. Equilibration

For equilibration of the different samples, the quaternary as well as the ternary samples were annealed at certain temperatures for several days, see Table 12. For this purpose, all samples, except PB58i, were placed into alumnia crucibles and further sealed under vacuum in quartz glass tubes (Fig. 30). The aluminia crucibles were used to exclude reactions of the samples with the quartz glass at high temperatures. The quartz glass tubes, which were already closed at one side, were evacuated and flushed with argon several times before they were sealed at around $7*10^{-3}$mBar by using

Fig. 30: Sealed samples.

an H_2/O_2 flame. The sample PB58i was sealed into a tantalum crucible and annealed at 1400 °C for two hours by using an induction furnace.

The samples PB9-PB43, already annealed as pills, were also annealed as powder pellets. Therefore, around 400 mg of each sample were powdered by using a tungsten carbide mortar, sieved with 0.18 mm mesh size and then pressed by a hydraulic press with about 15kN for 6 minutes. The 7 mm Ø pellets were sealed under vacuum in quartz glass tubes, as described before. Three successive annealing procedures were applied to reach sintering. The associated annealing programs are given in Tab. 13.

All samples were annealed corresponding to their programs in a conventional muffle furnace. To freeze the thermodynamic equilibria at the respective temperature, they were quenched in cold water after annealing. For pending investigations the samples were crushed by using a tungsten carbide mortar. One piece was powdered for X-ray diffraction measurements; another one was embedded in a kind of resin for metallographic investigations. The different analyzing methods and the annealing conditions of each sample are given in Tab. 12.

Table 12: Annealing conditions and analytical methods for each sample.

Sample	Annealing temperature (°C)	Annealing time	Analyzing methods		
			LOM	XRD	SEM
PB01	900	2 weeks	X	X	X
PB02	900	2 weeks	X	X	X
PB03	900	2 weeks	X	X	X
PB04	900	2 weeks	X	X	X
PB05	900	2 weeks	X	X	X
PB06	900	2 weeks	X	X	X
PB07	900	2 weeks	X	X	X
PB08	900	2 weeks	X	X	X
PB09*	900	2 weeks	X	X	X
PB10*	900	2 weeks	X	X	X
PB11*	900	2 weeks	X	X	X
PB12*	900	2 weeks	X	X	X
PB13*	900	2 weeks	X	X	X
PB14*	900	2 weeks	X	X	X
PB15*	900	2 weeks	X	X	X
PB16*	900	2 weeks	X	X	X
PB17*	900	2 weeks	X	X	X

Sample	Annealing temperature (°C)	Annealing time	Analyzing methods		
			LOM	XRD	SEM
PB18*	900	2 weeks		X	X
PB19*	900	2 weeks		X	X
PB20*	900	2 weeks		X	X
PB21*	900	2 weeks	X	X	X
PB22*	900	2 weeks		X	X
PB23*	900	2 weeks		X	X
PB24*	900	2 weeks	X	X	X
PB25*	900	2 weeks	X	X	X
PB26*	900	2 weeks	X	X	X
PB27*	900	2 weeks	X	X	X
PB28*	900	2 weeks	X	X	X
PB29*	900	2 weeks	X	X	X
PB30*	900	2 weeks	X	X	X
PB31*	900	2 weeks		X	X
PB32*	900	2 weeks		X	X
PB33*	900	2 weeks		X	X
PB34*	900	2 weeks	X	X	X
PB35*	900	2 weeks	X	X	X
PB36*	900	2 weeks	X	X	X
PB37*	900	2 weeks	X	X	X
PB38*	900	2 weeks	X	X	X
PB39*	900	2 weeks	X	X	X
PB40*	900	2 weeks	X	X	X
PB41*	900	2 weeks		X	X
PB42*	900	2 weeks		X	X
PB43*	900	2 weeks		X	X
PB44	900	2 weeks	X	X	X
PB45	900	2 weeks	X	X	X
PB46	900	2 weeks	X	X	X
PB47	900	2 weeks	X	X	X
PB48	900	2 weeks	X	X	X
PB49	900	2 weeks	X	X	X
PB50	900	2 weeks	X	X	X
PB51	900	2 weeks	X	X	X
PB52	900	2 weeks	X	X	X
PB53	900	2 weeks	X	X	X
PB54	900	2 weeks	X	X	X
PB55	900	2 weeks	X	X	X
PB56	900	2 weeks	X	X	X

Sample	Annealing temperature (°C)	Annealing time	Analyzing methods		
			LOM	XRD	SEM
PB57	900/1100	2 weeks	X	X	X
PB58	900/1100	2 weeks	X	X	X
PB58i**	1400	2 hours	X	X	X
PB59	900	2 weeks	X	X	X
PB60	900	2 weeks	X	X	X
PB61	900	2 weeks	X	X	X
PB62	900	2 weeks	X	X	X
PB63	900	2 weeks	X	X	X
PB64	900	2 weeks	X	X	X

*Powder pellets were made

**Annealed with an induction furnace

Table 13: Annealing conditions for the powder pellets.

Samples	Temperature program
PB009*-PB017*	**900°C** for 2 weeks
PB009*-PB017*	**1050°C**, 24 h; **900°C→1050°C**, 8 h; **900°C** for 2 weeks
PB009*-PB043*	**1100°C**, 72 h; **1100°C→900°C**, 144 h; **900°C** for 2 weeks

5.1.4.Embedding

For metallographic investigations, a piece of each sample was embedded. Therefore, sample pieces with flat surfaces were placed in the cylinder of a LaboPress (by Struers) and covered with phenolic hot mounting resin with carbon filler (PolyFast by Struers). The resin was heated to 180°C under a pressure of 15kN for five minutes, and then cooled for three minutes with water. By using silicon carbide sandpapers with a mesh size between 240 and 1200 the received cylinders were ground with a grinding machine (LaboPol-6 by Struers, Fig. 31). In the final step they were polished with a corundum powder (particle size of about 0.3 µm; MicroPolish II by BUEHLER) to get a smooth surface without scratches, which is essential for further microscopic studies. The dark-field mode of an optical microscope was applied to exclude all kinds of scratches.

Fig. 31: LaboPol-6 by Struers.

Fig. 32: Embedded samples.

5.1.5. Challenges of sample preparation procedure

The second melting step in the arc furnace treatment was the most difficult part of the practical work. Almost one sixth of the samples burst as they got in contact with the arc for the second time, due to the internal thermal expansion stress. When the fragments of the samples were few and big enough to be collected with twizzers, they were remelted and no further treatments were necessary, as the mass loss was lower than 1%. In the case of finely dispersed fragments, the sample had to be prepared once more. Consequently, a long heat-treatment duration of about 10 seconds after melting at the first arc-melting process was executed to ensure a decent mixing of the pure elements.

The mass loss of the pills after the annealing step can be neglected. But several glass tubes were tarnished and showed different shades of grey, orange and black after annealing. Also half of the pills were covered with a thin black layer, which could easily be removed by using a SiC sandpaper (1200). The mass loss after grinding the pills was around 1-10 mg. Reasons for this phenomenon could be:

-the application of already used alumnia crucibles, which still were contaminated although they were cleaned with hot aqua regia and further heated out at 1100 °C.

-quartz glass pieces or dust, which fell into the crucible during the sealing process, got in contact with the sample. In this case, by reaction with Al and Ti, the gaseous species SiO accrues at high temperatures. This species can subsequently react with other parts of the sample not directly in contact with SiO_2.

-contamination of oxygen or nitrogen during the arc furnace treatment.

The mass loss of the pellets after the annealing step where in a range of 0-11 mass%. Most of them were also covered with a thin black layer. Furthermore, some of the pellets showed bright metallic shiny spots at the bottom, which perhaps indicates partial melting due to the high temperature. Due to the fact that the pellets were not sintered during the first annealing conditions, two more programs at higher initial temperature were applied to reach sintering. By using spot tests the progress of each program was examined. The mass loss can be traced back to the high temperatures and the long annealing process.

Surface grindings of the powdered and pressed samples, except PB9-PB23 could be produced. The grindings showed several holes, but it was possible to investigate the different phases of each pellet by scanning electron microscopy.

5.2. Sample Analysis

5.2.1. X-ray powder diffraction

Fig. 33: Bruker D8 Discover Serie 2.

Phase identification and the refinement of structure parameters of each sample was performed by using X-ray powder diffraction. During this work a 'Bruker D8 Discover Series 2' diffractometer with Bragg-Brentano pseudo focusing geometrie and Θ/2Θ arrangement was used (Fig. 33). Detection was done by a silicon strip detector (LynxEye; measurement time: 1h) and an energy dispersive solid state detector (Sol-X; measurement time: 4h). The Sol-X detector was especially applied for high iron concentration in order to improve the peak/background ratio caused by the X-ray fluorescence of iron. The utilized X-ray radiation arises from a copper X-ray tube, working with an accelerating voltage of 40kV and an electronic current of 40mA. To exclude K_β radiation a Ni-filter was used. A small piece of every sample was powdered with a tungsten carbide mortar. The received powder was transferred to a silicon single crystal using Vaseline as binding agent. The silicon single crystals, which functions as sample holder, are finally affixed on the auto sampler of the diffractometer. Measurements at the diffractometer were done by using the software DIFFRAC^{plus} XRD commander.

The evaluation of the obtained diffraction patterns was done with the software TOPAS3 by Bruker. Structural information, therefore, was taken from literature like the Pearson's handbook of crystallographic and the database ICSD.

The refinement was done in the following order:

1. Loading of measurement parameters and instrumental data
2. Background correction
3. Loading of structure files for expected structures

4. Refinement and fitting of structural parameters (sequence):
    a. Scale factor
    b. Lattice parameters
    c. Crystal size
    d. Occupation of atom sites (especially in case of Fe_2Ti)
    e. Coordinates of the atom sites
    f. Temperature factor
    g. Sample displacement
5. R_w-value checking

In the first step the measurement and instrumental parameters as well as the structure were loaded. Once the background correction was performed, the refinement and fitting of the structural parameters were applied. The scale factor, lattice parameters and crystal size of the regarding peak phase were refined. These parameters were kept in refining mode during the whole Rietveld refinement. For all samples containing the Laves phase Fe_2Ti the simple site occupation model $(Fe,Al,Si)_2(Fe,Al,Si)_6(Ti,Fe)_4$ was used. More details will be explained in chapter 6. Prior the occupation of all atomic sites was refined. In the next step, the coordinates of atom sites were refined. As the intensity of certain reflections is strongly dependent on the occupation and coordinates of the sites, the temperature factor refinement carried out, after these parameters were fixed. The temperature factor was refined in such a way that there is no difference in occupation of the iron positions (2a and 6h) between Fe and (Al+Si). However, the temperature factor for the Ti position (4f) was refined separately. Prior to the final refinement, the sample displacement was set free, just before all of the above mentioned parameters were left free. Finally, the R_w-values were checked. In case of unsatisfactory results the refinement was repeated.

5.2.2. Reflected-light microscopy

A Zeiss Axiotech 100 microscope (Fig. 34) was used for investigations of the microstructure and the behavior of homogeneity of selected samples. Therefore, the usual imaging modes like dark and bright field imaging, as well as the polarization optic have been utilized by magnifications of 50, 100, 200 and 500.

Fig. 34: Zeiss Axiotech 100.

5.2.3. Scanning electron microscopy

The embedded samples were investigated with the scanning electron microscope (SEM) Zeiss Supra 55 VP (Fig. 35). Thereby, an acceleration voltage of 20 kV and a 120 µm bezel was used. For imaging of the surface a secondary electron detector as well as a back scatter detector was applied. For EPMA an energy dispersive detector (EDX) calibrated with the pure elements Al, Fe, Si and Ti was deployed. All different phases in each sample were measured at least ten times in different grains, to exclude the measurement errors. During the EPMA measurements a systematic error regarding the Ti and Fe concentration was encountered. Presumably, the observed systematical deviation was generated during the ZAF correction, which cannot be optimally applied on the quaternary system Al-Fe-Si-Ti. The error is estimated to lie in a range between 0.5-1 at.%.

Fig. 35: Zeiss Supra 55 VP [60].

6. Results and discussion

6.1. Partial isothermal sections at different Ti-concentrations

6.1.1. 33.3 at.% Ti

The partial isothermal section at 33.3 at.% Ti of the quaternary system Al-Fe-Si-Ti is presented in Fig. 36. It contains the composition of all prepared samples at the 33.3 at.% Ti section annealed at 900 °C, the relevant phase equilibria of the ternary systems Al-Fe-Ti and Fe-Si-Ti and a schematical depiction of the behavior of the single phase field Fe_2Ti and the two-phase field Fe_2Ti+Al_2FeTi. The X-ray powder diffraction data as well as the SEM results for every sample are given in Table 14. All given results were calculated from sample pills.

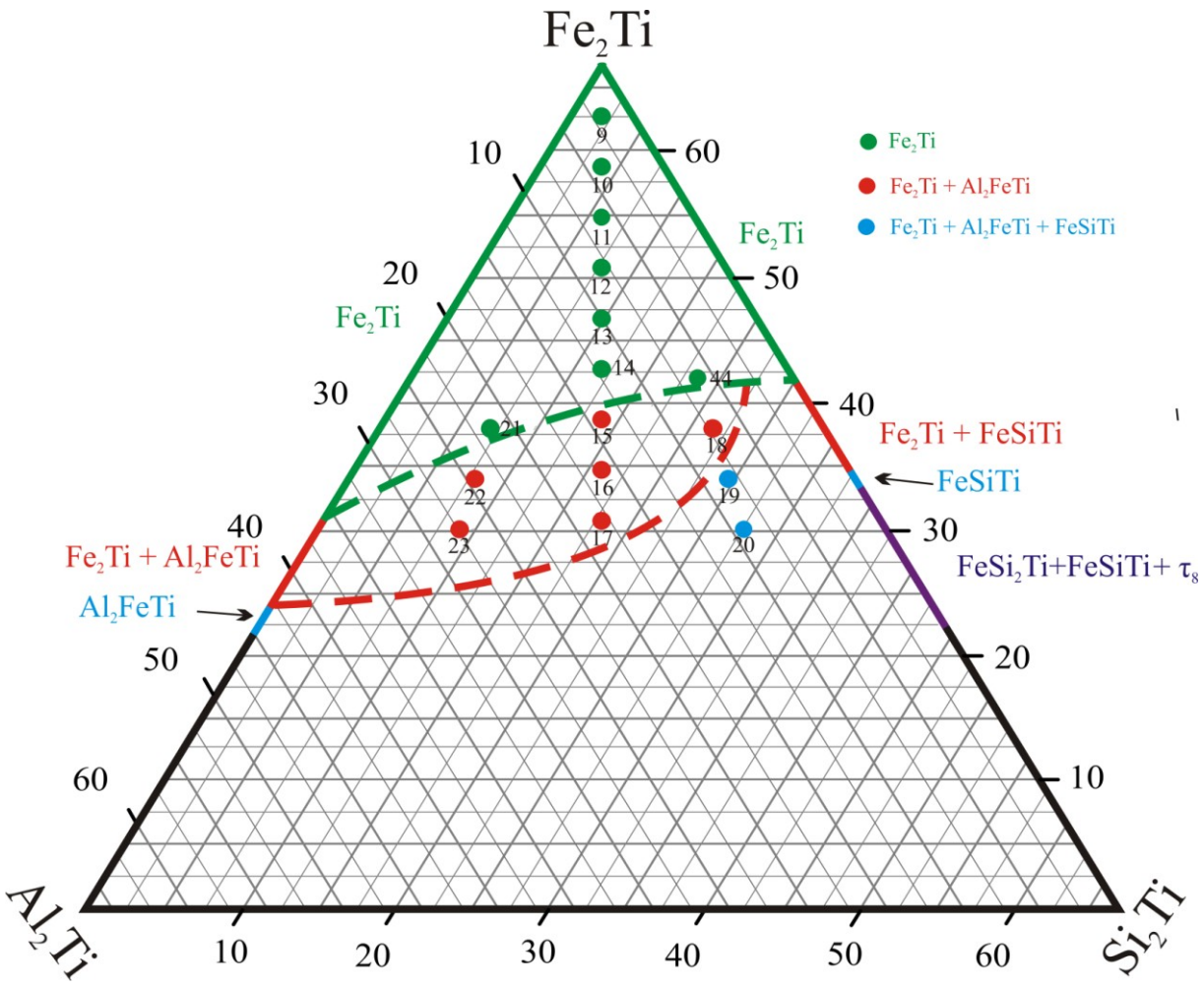

Fig. 36: Partial isothermal section of the quaternary system Al-Fe-Si-Ti at 33.3 at.% Ti annealed at 900 °C.

Table 14: XRD and SEM results of the partial isothermal section at 33.3 at.% Ti at 900 °C of the quaternary system.

Sample/ nom. comp. (at.%)	Phase analysis			SEM			
	Phase	XRD Lattice parameter (Å)	XRD %	Al (at.%)	Fe (at.%)	SI (at.%)	Ti (at.%)
PB9 $Al_2Fe_{62.7}Si_2Ti_{33.3}$	Fe_2Ti	*a* = 4.8020(5)	99*	2.1	61.2	2.8	33.9
		c = 7.8299(1)					
PB10 $Al_4Fe_{58.7}Si_4Ti_{33.3}$	Fe_2Ti	*a* = 4.8104(10)	99*	3.9	57.1	5.4	33.6
		c = 7.8342(2)					
PB11 $Al_6Fe_{54.7}Si_6Ti_{33.3}$	Fe_2Ti	*a* = 4.8218(1)	99*	5.9	53.8	6.3	34.0
		c = 7.8410(3)					
PB12 $Al_8Fe_{50.7}Si_8Ti_{33.3}$	Fe_2Ti	*a* = 4.8341(1)	99*	6.0	49.7	10.4	33.9
		c = 7.8442(3)					
PB13 $Al_{10}Fe_{46.7}Si_{10}Ti_{33.3}$	Fe_2Ti	*a* = 4.8473(1)	99*	8.7	46.3	11.2	33.8
		c = 7.8466(3)					
PB14 $Al_{12}Fe_{42.7}Si_{12}Ti_{33.3}$	Fe_2Ti	*a* = 4.8621(2)	99*	10.0	42.6	13.4	34.0
		c = 7.8449(6)					
PB15 $Al_{14}Fe_{38.7}Si_{14}Ti_{33.3}$	Fe_2Ti	*a* = 4.8776(1)	97	11.9	38.9	15.0	34.2
		c = 7.8449(3)					
	Al_2FeTi	*a* = 11.9608(4)	3	32.3	24.2	7.1	36.4
PB16** $Al_{16}Fe_{34.7}Si_{16}Ti_{33.3}$	Fe_2Ti	*a* = 4.8641(9)	73	9.9	38.2	17.9	34.0
		c = 7.7973(2)					
	Al_2FeTi	*a* = 11.9372(3)	27	29.3	23.4	11.2	36.1
PB17** $Al_{18}Fe_{30.7}Si_{18}Ti_{33.3}$	Fe_2Ti	*a* = 4.8520(1)	55	8.1	37.4	20.9	33.6
		c = 7.7473(2)					
	Al_2FeTi	*a* = 11.9094(3)	45	28.8	24.6	13.1	33.5
PB18** $Al_{7.175}Fe_{38}Si_{21.525}Ti_{33.3}$	Fe_2Ti	*a* = 4.8534(1)	96	5.9	38.2	22.0	33.9
		c = 7.7469(2)					
	Al_2FeTi	*a* = 11.909(3)	4	15.9	17.7	21.8	44.6
PB19** $Al_{8.175}Fe_{34}Si_{24.525}Ti_{33.3}$	Fe_2Ti	*a* = 4.8537(1)	58	6.8	36.9	22.8	33.5
		c = 7.7467(3)					
	Al_2FeTi	*a* = 11.8872(5)	13	-	-	-	-
	FeSiTi	*a* = 7.0051(4)	29	0.8	31.8	32.6	34.8
		b = 10.8989(8)					
		c = 6.2664(4)					

Sample/ nom. comp. (at.%)	Phase analysis			ESEM			
	Phase	XRD Lattice parameter (Å)	XRD %	Al (at.%)	Fe (at.%)	SI (at.%)	Ti (at.%)
PB20** **$Al_{9.175}Fe_{30}Si_{27.525}Ti_{33.3}$**	Fe_2Ti	*a* = 4.8539(6)	11	15.6	31.4	20.4	32.6
		c = 7.7685(2)					
	Al_2FeTi	*a* = 11.8859(3)	26	37.6	24.7	11.1	26.6
	FeSiTi	*a* = 7.0205(1)	63	1.0	30.9	32.8	35.3
		b = 10.8836(3)					
		c = 6.2959(2)					
PB21 **$Al_{21.525}Fe_{38}Si_{7.175}Ti_{33.3}$**	Fe_2Ti	*a* = 4.9095(7)	99*	20.7	37.9	7.1	34.3
		c = 7.9348(2)					
PB22 **$Al_{24.525}Fe_{34}Si_{8.175}Ti_{33.3}$**	Fe_2Ti	*a* = 4.9129(10)	80	21.6	36.0	8.5	34.0
		c = 7.9273(2)					
	Al_2FeTi	*a* = 11.9868(4)	20	35.5	23.5	5.9	35.1
PB23** **$Al_{27.525}Fe_{30}Si_{9.175}Ti_{33.3}$**	Fe_2Ti	*a* = 4.9009(1)	47	19.0	36.6	10.9	33.5
		c = 7.9053(3)					
	Al_2FeTi	*a* = 11.9668(3)	53	35.7	23.6	6.7	34.0
PB44 **$Al_{6.175}Fe_{42}Si_{18.525}Ti_{33.3}$**	Fe_2Ti	*a* = 4.8428(2)	99*	5.5	41.7	18.9	33.9
		c = 7.7754(4)					

*Traces of FeTi were found

**Traces of an unknown structure, probably due to impurities or oxygen contamination.

Table 15: Relevant crystal structure data of the binary and ternary phases for the partial isothermal section at 33.3 at.% Ti at 900 °C.

Phases	Lattice parameters (Å)	Structure type	Strukturbericht designation	Space group	Reference
Fe_2Ti	*a* = 4.787	$MgZn_2$	C14	*P*63/*mmc*	**[61]**
	c = 7.815				
FeTi	*a* = 2.976	CsCl	B2	$Pm\bar{3}m$	**[62]**
FeSiTi	*a* = 6.997	FeSiTi	-	*Ima*2	**[39]**
	b = 10.83				
	c = 6.287				
Al_2FeTi	*a* = 11.99	$Mn_{23}Th_6$	$D8_a$	$Fm\bar{3}m$	**[32]**

In the presented partial isothermal section (Fig. 36) the Laves phase Fe_2Ti shows a large solid solubility for Al and Si. The phase boundary was schematically drawn according to the already known solid solubilities of Fe_2Ti for Al and Si **[36, 41]**, and the received results during this work.

All samples prepared in this section are more or less homogenous. However, the samples PB9-PB14, PB21 and PB44, which are situated in the single-phase field Fe_2Ti, contain traces of FeTi. This XRD results were confirmed by SEM investigations, where minimum amounts of FeTi were observed on the boundaries of the grains. In most cases it was not possible to measure the FeTi contaminations due to their small size with an observed average diameter of less than 3 µm.

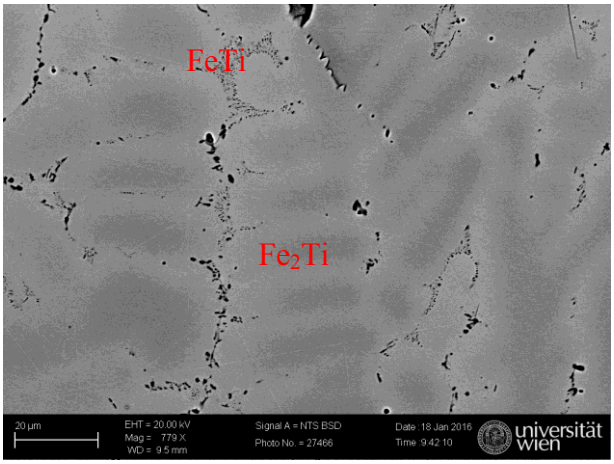

Fig. 37: SEM-image of PB9, showing Fe_2Ti and traces of FeTi. Also the effect of grain segregation can be observed (different shades of grey within the grains).

The samples PB15 and PB22 show two phases. They both contain the Laves phase and the ternary phase Al_2FeTi, which is in good agreement to the two-phase field Fe_2Ti and τ_2 of the ternary system Al-Fe-Ti **[36]**. In both samples the amount of the Laves phase outweighs the other one. The samples PB16-PB18 and PB23 are also in the two phase equilibrium Fe_2Ti and Al_2FeTi, but show three additional unidentified lines.

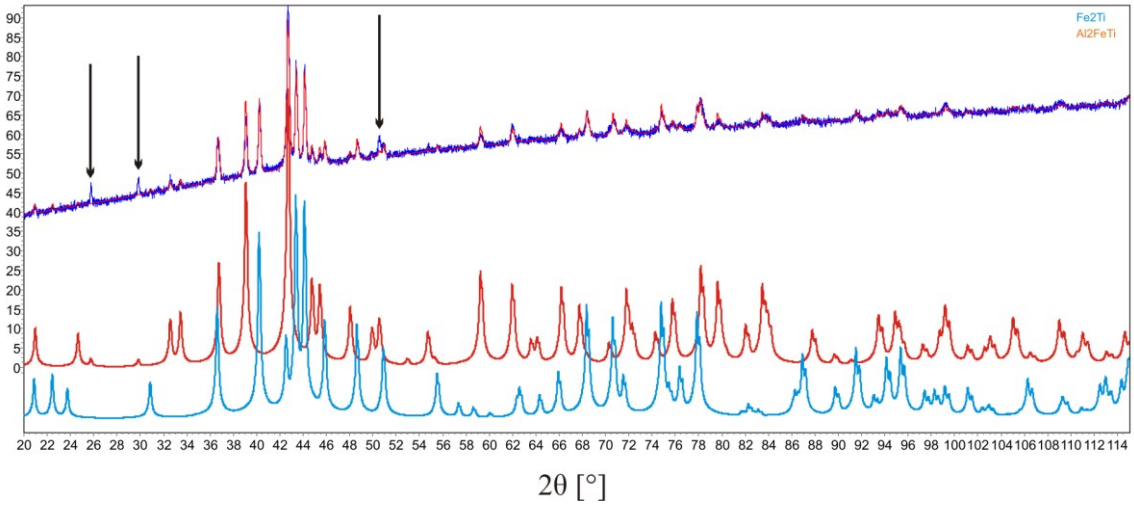

Fig. 38: XRD-pattern of sample PB23, showing the calculated structures and the yet unknown diffraction peaks, marked with black arrows.

It was not possible to characterize this unknown structure by SEM investigations. The three additional peaks assigned to the unknown structure (see Fig. 38) were most pronounced in the XRD-pattern of sample PB23. In all other XRD-patterns the observed intensities were much lower, whereby the diffraction line at 2Θ=26°shows the highest intensity. The samples PB19 and PB20 are in a three-phase equlibria. They exhibit the Laves phase, Al_2FeTi (τ_2) from the ternary system Al-Fe-Ti, FeSiTi (τ_2) from the ternary system Fe-Si-Ti and the additional unidentified reflexes, which were also found in PB16-PB18 and PB23. The corresponding XRD-pattern for sample PB20 is given in Fig. 39. The results of the two- and three-phase containing samples show, that the Al_2FeTi phase was measured up to a concentration of more than 27 at.% Si (PB20) in this isothermal section at 33.3 at.% Ti.

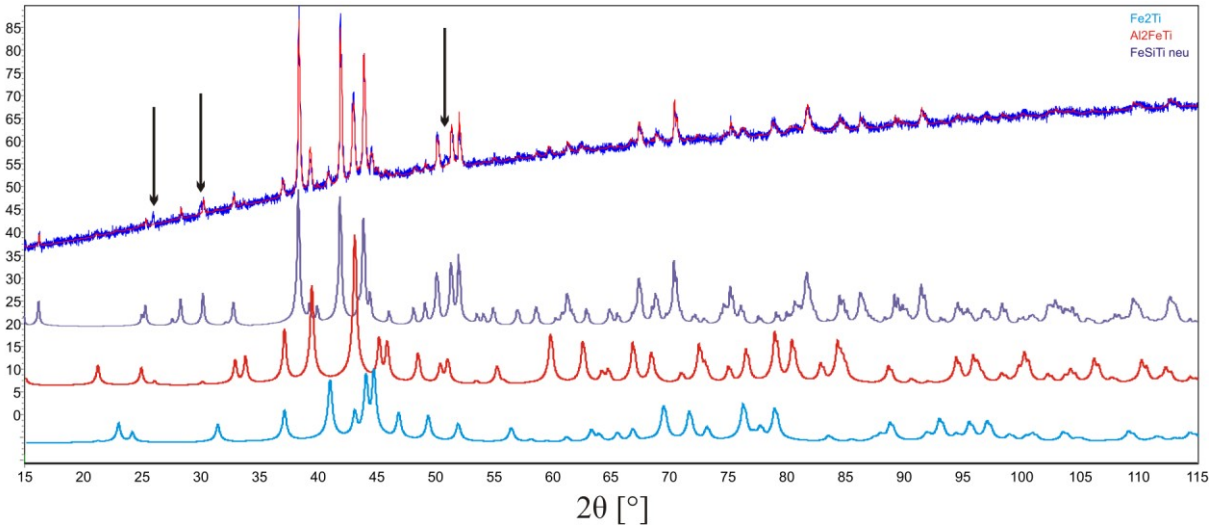

Fig. 39: XRD-pattern of PB20, showing the calculated structures and the yet unknown diffraction peaks, marked with black arrows.

Grain segregation was observed in all samples situated in the single-phase field Fe_2Ti. This effect was investigated in more detail on the sample PB9. A large grain was selected and measured by line-scans with SEM. The observed results are given in Fig. 40. It shows that the Fe concentration and the Al concentration behave similar, their concentrations decrease towards the grain center. However, the Ti-concentrations stays constant, while the Si concentration shows an increasing behavior towards the grain center. It can be deduced, that primarily Fe_2Ti enriched with Si crystallizes. (The quality of the Rietveld refinements is reduced due to severe line broadening causes by grain segregation. Grain segregation also has a negative effect on the quality of the SEM-measurements.)

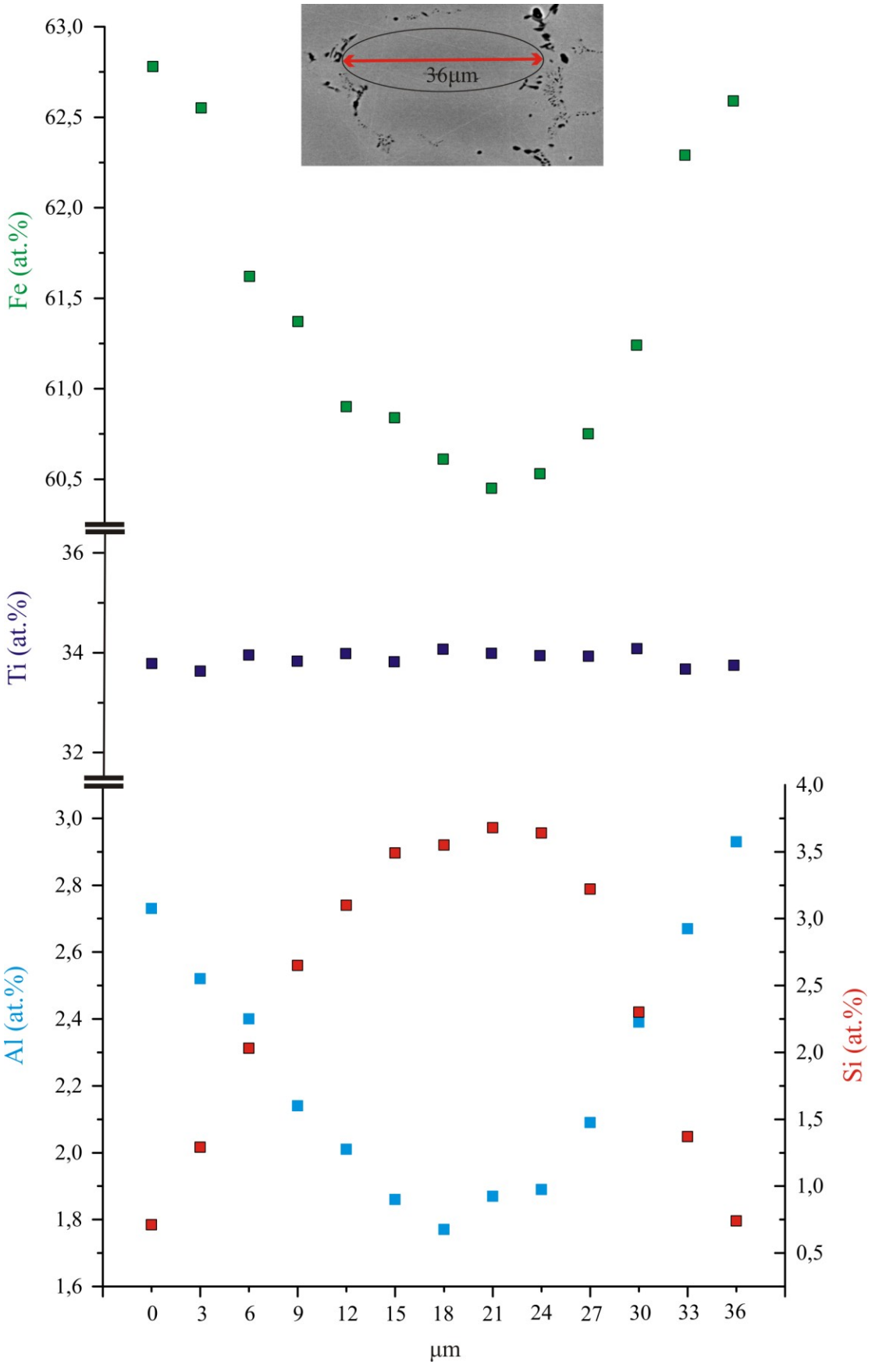

Fig. 40: Grain segregation effect, measured in PB9.

The $MgZn_2$-type structure of Fe_2Ti has three different crystallographic positions, whereby the 2*a* and the 6*h* positions are occupied by Fe-atoms and the 4*f* position by Ti. Fe_2Ti shows a homogeneity range in the binary system, especially towards the Fe-rich side **[25]**. This phenomenon occurs because Fe can substitute Ti on the 4*f* site **[63]**. Studies on the ternary system Al-Fe-Ti reported the occupation of the Fe positions 2*a* and 6*h* by Al-atoms with preference of the 2*a* site **[51]**. For the quaternary system Al-Fe-Si-Ti at 33.3 at.% Ti a simple site occupation model (a) was used $(\mathbf{Fe},Al,Si)_2(\mathbf{Fe},Al,Si)_6(\mathbf{Ti})_4$. Due to the fact, that Al and Si have similar scattering factors, it is not possible to distinguish between these two elements in XRD measurements.

Table 16: Comparison of refined and nominal compositions.

Sample/ nom. comp. (at.%)	Model	Al+Si	Fe	Ti
		(at.%)	(at.%)	(at.%)
PB9 $\mathbf{Al_2Fe_{62.7}Si_2Ti_{33.3}}$	a	2	64.7	33.3
PB10 $\mathbf{Al_4Fe_{58.7}Si_4Ti_{33.3}}$	a	6.1	60.6	33.3
PB11 $\mathbf{Al_6Fe_{54.7}Si_6Ti_{33.3}}$	a	10.4	56.3	33.3
PB12 $\mathbf{Al_8Fe_{50.7}Si_8Ti_{33.3}}$	a	15.6	51.1	33.3
PB13 $\mathbf{Al_{10}Fe_{46.7}Si_{10}Ti_{33.3}}$	a	19.5	47.2	33.3
PB14 $\mathbf{Al_{12}Fe_{42.7}Si_{12}Ti_{33.3}}$	a	20.3	46.4	33.3

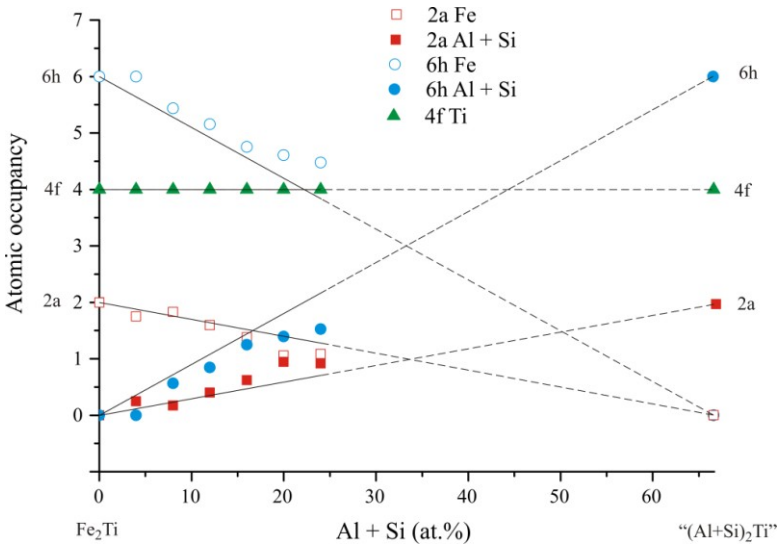

Fig. 41: Site occupancies in the Laves phase Fe_2Ti of the quaternary system Al-Fe-Si-Ti at 33.3 at.% Ti vs. nom. comp. of (Al+Si).

The refined compositions obtained by Rietveld refinement (Table 16), show especially in the Al/Si poor and in the Al/Si rich sample a deviation from the nominal composition. In the range of 12 at.% (Al+Si) (1:1) and higher, the values are reasonably accurate. In Fig. 41 the dependence of the site occupancies of the Laves phase Fe_2Ti on the composition is given based on Rietveld refinement data. An approaching linearity of the dependence of the site occupancy with the composition is represented. Thereby, the occupancy of the 2*a* position with (Al+Si)-atoms shows an average positive deviation and an average negative deviation for the 6*h* Fe position. This characteristic is most pronounced for low concentrations of (Al+Si), when only the 2*a* Fe-position is occupied with (Al+Si), and at high (Al+Si) contents (>20 at.%) of the Laves phase. All results were plotted against the nominal composition of each sample. The data obtained from SEM could not be used because of grain segregation of the Fe_2Ti samples.

Based on XRD-data, obtained by Rietveld refinements, the lattice parameters *a* and *c* as well as the volume of the Laves phase for the samples PB9-PB15 were plotted against the amount of (Al+Si), see Fig. 42. To show the further behavior of each parameter the data of the first two-phase field sample was included, marked with an open square. The lattice parameters *a* and *c* increase with increasing (Al+Si) concentration. The volume shows a linear increase with increasing amounts of (Al+Si). Compared to the behavior of the mentioned parameters in the Laves phase in the systems Al-Fe-Ti **[51]** and Fe-Si-Ti, given in 6.3., the lattice parameters as well as the volume of the Laves phase Fe_2Ti in the quaternary system Al-Fe-Si-Ti behave similar to the Al-Fe-Ti system.

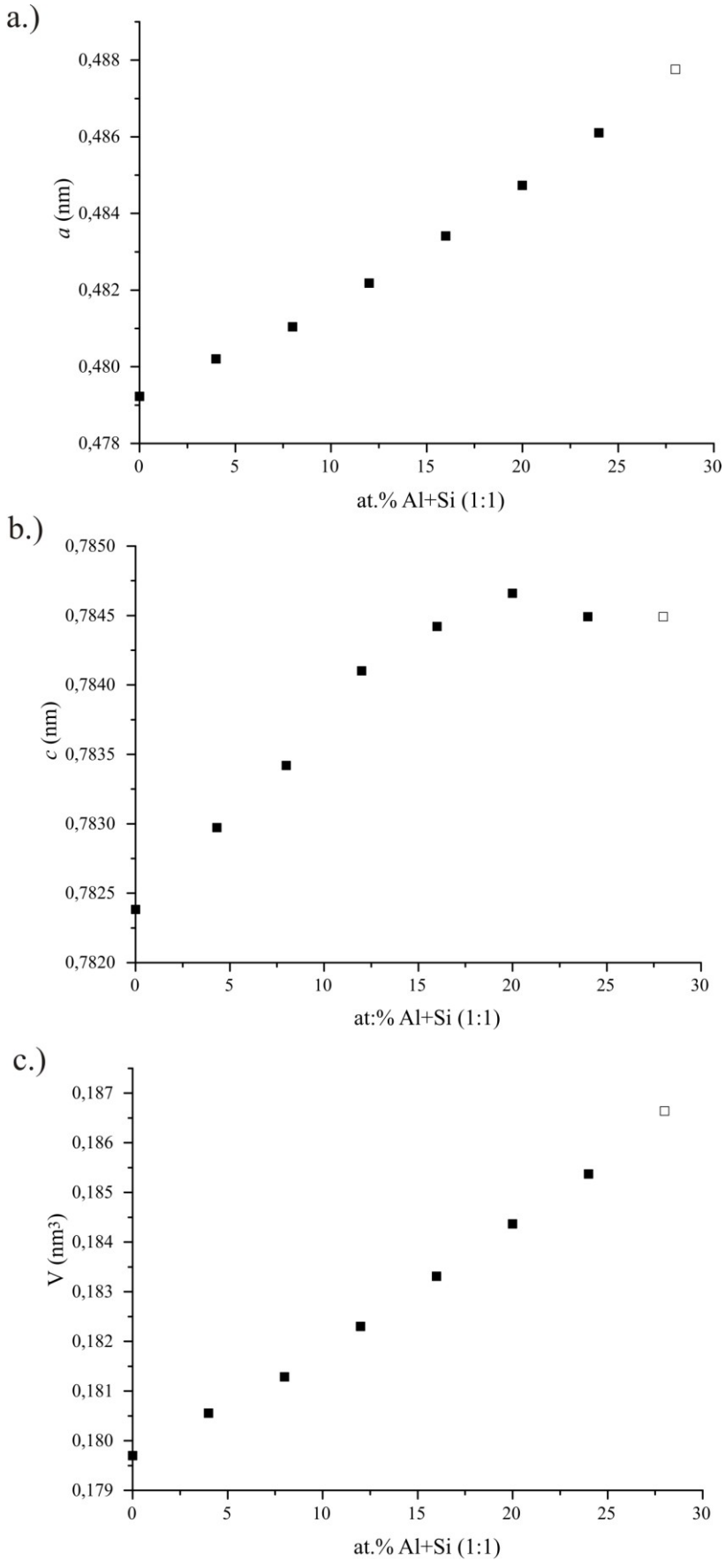

Fig. 42: Lattice parameters *a* and *c* as well as the volume of the Laves phase Fe_2Ti vs. nom. comp. of (Al+Si).

6.1.2. 25 at.% Ti

The partial isothermal section at 25 at.% Ti of the quaternary system Al-Fe-Si-Ti is presented in Fig. 43. It contains the composition of all prepared samples at the 25 at.% Ti section annealed at 900 °C, the relevant phase equilibria of the ternary systems Al-Fe-Ti and Fe-Si-Ti, a schematical depiction of the two-phase fields A2/$D0_3$+Fe2Ti and $D0_3$+Fe_2Ti as well as of the four-phase field B2+Fe_2Ti+FeSiTi+Al_2FeTi. The X-ray powder diffraction and the relevant SEM results for every sample are given in Table 17. The different bcc-based modifications in the Fe-rich part of the ternary systems Al-Fe-Ti and Fe-Si-Ti are denoted through this thesis as A2 for (αFe); B2 for (AlFe); $D0_3$ for (Fe_3Al), (Fe_3Si) and the ternary ordered $L2_1$ (Heusler phase) of the ternary system Al-Fe-Ti.

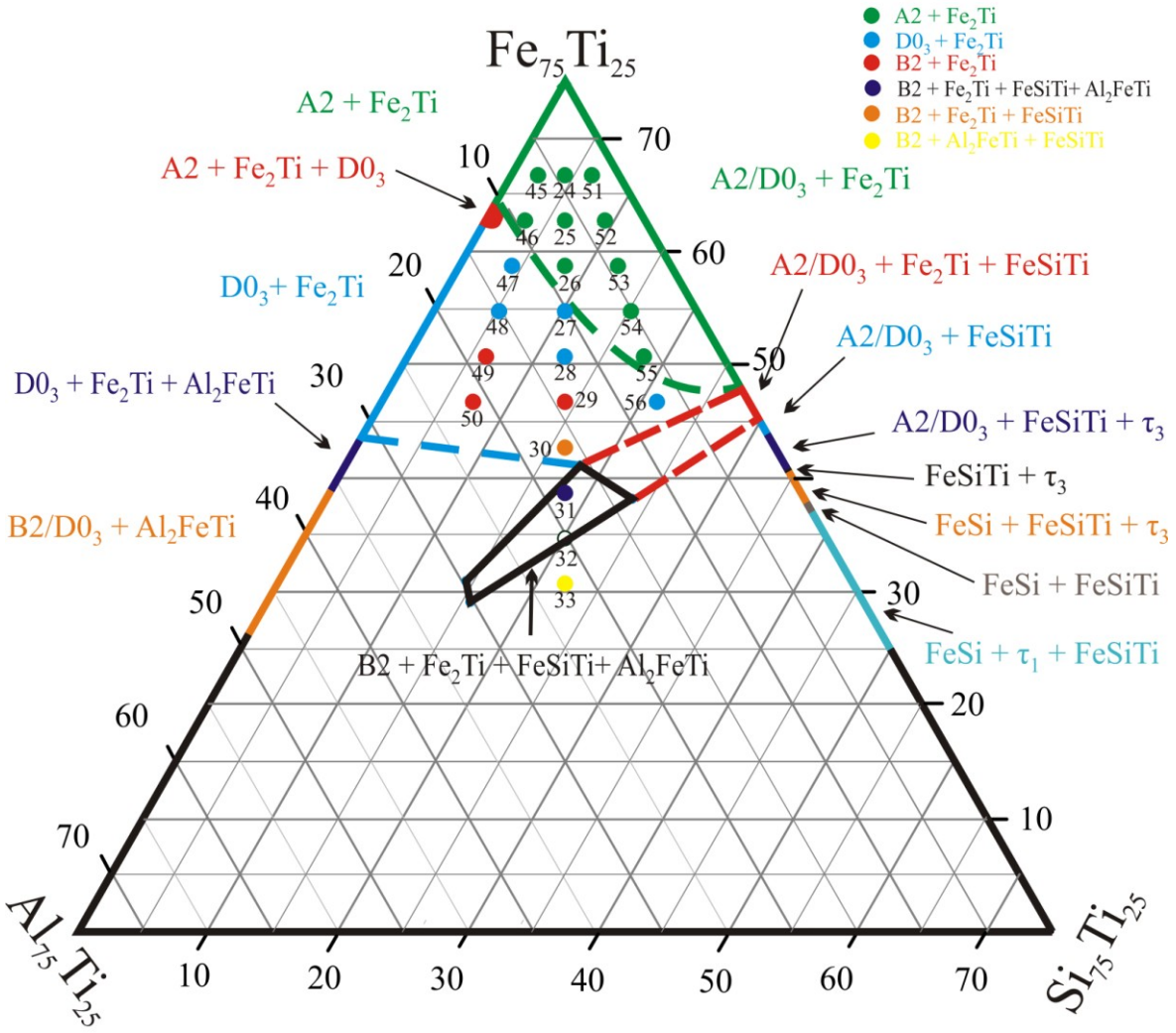

Fig. 43: Partial isothermal section of the quaternary system Al-Fe-Si-Ti at 25 at.% Ti annealed at 900 °C. No distinction between A2/B2/$D0_3$ in the two-phase field A2/$D0_3$+Fe_2Ti is given in the system Fe-Si-Ti, according to the literature. All samples in this two-phase field show A2 and Fe_2Ti. PB32, marked with an open circle, did not reach equilibrium.

Table 17: XRD and SEM results of the partial isothermal section at 25 at.% Ti at 900 °C of the quaternary system.

Sample/ nom. comp. (at.%)	Phase analysis			SEM			
	Phase	XRD Lattice parameter (Å)	XRD %	Al (at.%)	Fe (at.%)	SI (at.%)	Ti (at.%)
PB24 $Al_{4.15}Fe_{66.7}Si_{4.15}Ti_{25}$	Fe_2Ti	a = 4.7841(8)	89	3.4	62.4	5.2	29
		c = 7.7949(2)					
	A2	a = 2.8932(2)	11	10.5	84.8	0	4.7
PB25 $Al_{6.15}Fe_{62.7}Si_{6.15}Ti_{25}$	Fe_2Ti	a = 4.7871(9)	90	4.7	59.2	7.4	28.7
		c = 7.7940(2)					
	A2	a = 2.8993(2)	10	15.5	78.8	0.2	5.5
PB26 $Al_{8.15}Fe_{58.7}Si_{8.15}Ti_{25}$	Fe_2Ti	a = 4.7925(9)	89	5.7	55.8	9.5	29
		c = 7.7931(2)					
	A2	a = 2.9068(2)	11	21.2	71.4	0.2	7.2
PB27 $Al_{10.15}Fe_{54.7}Si_{10.15}Ti_{25}$	Fe_2Ti	a = 4.7966(8)	88	7	52.8	11.9	28.3
		c = 7.7843(2)					
	$D0_3$	a = 5.8181(3)	12	25.4	60.4	1.4	12.8
PaBe28 $Al_{12.15}Fe_{50.7}Si_{12.15}Ti_{25}$	Fe_2Ti	a = 4.8076(9)	81	6.7	48.6	15.3	29.4
		c = 7.7731(2)					
	$D0_3$	a = 5.8327(2)	19	27.9	55.2	2.1	14.8
PB29 $Al_{14.15}Fe_{46.7}Si_{14.15}Ti_{25}$	Fe_2Ti	a = 4.8224(8)	83	8.9	44.8	17.1	29.2
		c = 7.7630(2)					
	B2	a = 2.9200(1)	17	34.7	52.0	1.6	11.7
PB30 $Al_{16.15}Fe_{42.7}Si_{16.15}Ti_{25}$	Fe_2Ti	a = 4.8392(9)	82	9.1	41.7	19.3	29.9
		c = 7.7589(2)					
	B2	a = 2.9203(2)	15	38.0	50.7	1.7	9.6
	FeSiTi*	a = 6.9956(3)	3	-	-	-	-
		b = 10.8174(7)					
		c = 6.2914(4)					
PB31 $Al_{18.15}Fe_{38.7}Si_{18.15}Ti_{25}$	Fe_2Ti	a = 4.8396(9)	68	8.6	39.0	22.4	30
		c = 7.7408(2)					
	B2	a = 2.9177(2)	11	42.5	48.8	2.3	6.4
	Al_2FeTi	a = 11.8397(9)	14	36	28.5	12.0	23.5
	FeSiTi*	a = 7.0015(2)	7	-	-	-	-
		b = 10.8203(3)					
		c = 6.2852(2)					

Sample/ nom. comp. (at.%)	Phase analysis			SEM			
	Phase	XRD Lattice parameter (Å)	XRD %	Al (at.%)	Fe (at.%)	SI (at.%)	Ti (at.%)
PB33** $Al_{22.15}Fe_{30.7}Si_{22.15}Ti_{25}$	B2	a = 2.9074(2)	-	46.4	47.1	3.5	3.0
	Al_2FeTi	a = 11.7966(4)	-	37.0	25.1	14.7	23.2
	FeSiTi	a = 7.0389(3) b = 10.8777(7) c = 6.2641(4)	-	2.0	31.2	32.8	34.0
PB45 $Al_{6.225}Fe_{66.7}Si_{2.075}Ti_{25}$	Fe_2Ti	a = 4.7888(7) c = 7.8033(2)	88	5.3	63.7	2.4	28.6
	A2	a = 2.8975(4)	12	13.2	81.6	0.0	5.2
PB46 $Al_{9.225}Fe_{62.7}Si_{3.075}Ti_{25}$	Fe_2Ti	a = 4.7960(6) c = 7.8085(1)	93	8.2	60.4	3.5	27.9
	A2	a = 2.9050(3)	7	19.1	74.4	0.0	6.5
PB47 $Al_{12.225}Fe_{58.7}Si_{4.075}Ti_{25}$	Fe_2Ti	a = 4.7987(8) c = 7.8094(2)	79	8.0	58.2	5.4	28.4
	$D0_3$	a = 5.8396(2)	21	23.6	57.7	0.6	18.1
PaBe48 $Al_{15.225}Fe_{54.7}Si_{5.075}Ti_{25}$	Fe_2Ti	a = 4.8055(1) c = 7.8105(3)	68	8.6	54.4	7.9	29.1
	$D0_3$	a = 5.8536(2)	32	24.3	53.9	1.0	20.8
PB49 $Al_{18.225}Fe_{50.7}Si_{6.075}Ti_{25}$	Fe_2Ti	a = 4.8211(2) c = 7.8101(3)	52	10.4	49.1	11.0	29.5
	B2	a = 2.9320(9)	47	25.7	51.6	1.1	21.6
PB50 $Al_{21.225}Fe_{46.7}Si_{7.075}Ti_{25}$	Fe_2Ti	a = 4.8523(1) c = 7.8328(3)	63	15.3	43.5	11.5	29.7
	B2	a = 2.9342(10)	37	28.5	50.2	1.1	20.3
PB51 $Al_{2.075}Fe_{66.7}Si_{6.255}Ti_{25}$	Fe_2Ti	a = 4.7822(6) c = 7.7885(1)	89	1.6	61.4	7.6	29.4
	A2	a = 2.8835(2)	11	6.3	89.3	0.2	4.2
PB52 $Al_{3.075}Fe_{62.7}Si_{9.225}Ti_{25}$	Fe_2Ti	a = 4.7829(6) c = 7.7798(1)	88	2.0	57.7	11.0	29.3
	A2	a = 2.8898(2)	12	10.0	84.6	0.8	4.6
PB53 $Al_{4.075}Fe_{58.7}Si_{12.225}Ti_{25}$	Fe_2Ti	a = 4.7853(8) c = 7.7665(2)	91	2.2	54.2	14.3	29.3
	A2	a = 2.8943(2)	9	14.4	80.6	1.0	4.0
PaBe54 $Al_{5.075}Fe_{54.7}Si_{15.225}Ti_{25}$	Fe_2Ti	a = 4.7908(9) c = 7.7474(2)	91	2.5	50.4	17.6	29.5
	A2	a = 2.9013(2)	9	19.6	75.3	1.5	3.6

Sample/ nom. comp. (at.%)	Phase analysis			SEM			
	Phase	XRD Lattice parameter (Å)	XRD %	Al (at.%)	Fe (at.%)	SI (at.%)	Ti (at.%)
PB55 $Al_{6.075}Fe_{50.7}Si_{18.225}Ti_{25}$	Fe_2Ti	a = 4.7965(9)	90	3.1	47.7	20.3	28.9
		c = 7.7255(2)					
	A2	a = 2.8930(3)	10	23.7	65.2	4.4	6.6
PB56** $Al_{7.075}Fe_{46.7}Si_{21.225}Ti_{25}$	Fe_2Ti	a = 4.8088(9)	90	3.4	43.7	23.1	29.7
		c = 7.7028(2)					
	$D0_3$	a = 5.7706(5)	10	27.8	58.7	7.4	6.1

*Could not be measured by SEM

**Traces of an unknown structure, probably due to impurities or oxygen contamination.

Table 18: Relevant crystal structure data of the binary and ternary phases for the partial isothermal section at 25 at.% Ti at 900 °C.

Phases	Lattice parameters (Å)	Structure type	Strukturbericht designation	Space group	Reference
αFe	a = 2.8665	W	A2	$Im\bar{3}m$	**[64]**
AlFe	a = 2.889	CsCl	B2	$Pm\bar{3}m$	**[65]**
Fe_3Al	a = 5.791	BiF_3	$D0_3$	$Fm\bar{3}m$	**[66]**
Fe_3Si	a =0.565	BiF_3	$D0_3$	$Fm\bar{3}m$	**[67]**
Fe_2Ti	a = 4.787 c = 7.815	$MgZn_2$	C14	$P63/mmc$	**[61]**
FeTi	a = 2.976	CsCl	B2	$Pm\bar{3}m$	**[62]**
FeSiTi	a = 6.997 b = 10.83 c = 6.287	FeSiTi	-	$Ima2$	**[39]**
Al_2FeTi	a = 11.99	$Mn_{23}Th_6$	$D8_a$	$Fm\bar{3}m$	**[32]**

In the presented partial isothermal section (Fig. 43) two different two-phase fields were observed. They both contain the Laves phase Fe_2Ti and a bcc modification of the Fe-rich corner of the corresponding ternary systems. Their phase boundaries were schematically drawn according to data of the ternary systems **[36, 41]**, and the received results during this work.

It is known from literature that the B2 structure (CsCl-type, $Pm\bar{3}m$) is formed in a second order transition from the disordered A2 structure (W-type, $Im\bar{3}m$). Thereby, the corners of the cubic cell are occupied by Fe-atoms and in the center of the unit cell by Al- or Fe-atoms. A second order transition of B2 forms the $D0_3$ structure (BiF_3-type, $Fm\bar{3}m$), whereby the unit cell parameters are doubled **[68]**. Ternary ordering of the $D0_3$ structure forms the $L2_1$ structure ($AlCu_2Mn$-type, $Fm\bar{3}m$). In this ordering the two Fe-positions 4a and 8c of the $D0_3$ structure are occupied by different mixtures of atoms. The $L2_1$ structure type has been presented in the Al-Fe-Ti system **[11]**. Furthermore, it is already known that the order/disorder transition cannot always be suppressed on quenching.

All samples containing the A2, B2 or $D0_3$ were carefully investigated by XRD to determine the correct structure. The main problem in analyzing the corresponding XRD powder diffraction patterns is, that the main diffraction lines of these three structures are identical. Identification of each structure type is only possible based on relatively weak diffractions lines (Fig. 44). In multi-phase samples, where these phases were found in low concentration, a differentiation is almost impossible. In the current work, no differentiation between the $D0_3$ and the $L2_1$-structure was done and all samples containing one of these structures were denote $D0_3$.

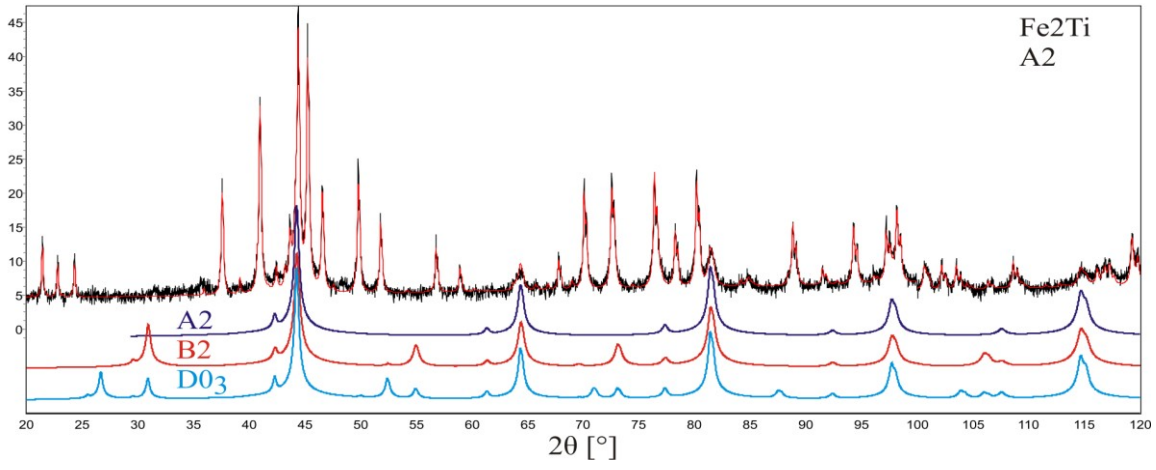

Fig. 44: XRD-pattern of PB24, showing the refined structures and the differences of the diffraction peaks for A2/B2/$D0_3$.

All samples prepared in this section, except PB32, were homogenous according to the SEM data. The samples PB24-PB29, PB45-PB50 and PB51-PB56 contain the Laves phase and either A2, B2 or $D0_3$. XRD-results report in most cases a distribution from 9:1 between the Fe_2Ti and the additional phase. At concentrations of 16.3 at.% (Al+Si, with a ratio of 3:1) the amount of the Laves phase decreases steadily. According to the phase equilibria $D0_3$+Fe_2Ti of the ternary system Al-Fe-Ti, three samples (PB29, PB49 and PB50) showed the unexpected B2 structure. It is assumed that the B2 phase is not at equilibrium at this respective concentration and temperature, but rather has formed during quenching. As the A2/B2/$D0_3$ phases are related by second order transitions metastable equilibria are probable. The transition changes between the bcc-modifications in the quaternary system are not clarified and transition changes by quenching the samples cannot be excluded.

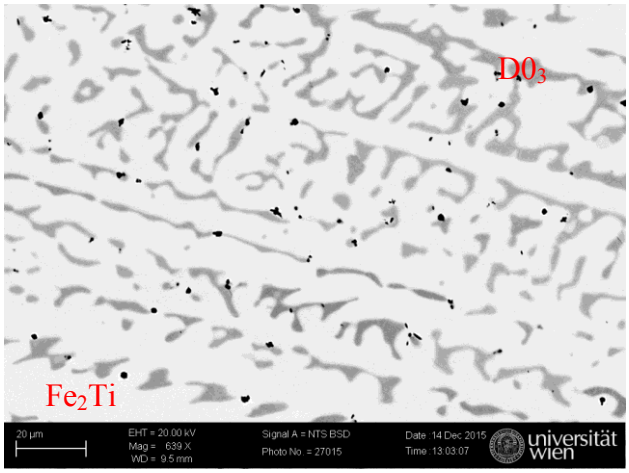

Fig. 45: SEM-image of PB27, showing Fe_2Ti and $D0_3$.

The sample PB30 showed a three-phase equilibrium. It contains Fe_2Ti, B2 and FeSiTi (τ_2) from the ternary system Fe-Si-Ti, which is in good agreement with the three phase field A2/$D0_3$+Fe_2Ti+FeSiTi, if a potential transition change of A2/B2/$D0_3$ is considered. The samples PB33 is also in three-phase equilibrium. It contains B2, Al_2FeTi (τ_2) and FeSiTi (τ_2), but show additional unidentified lines, which were already discussed in detail in 6.1.1. PB31 is in four-phase equilibrium and shows the Laves phase Fe_2Ti, B2, Al_2FeTi (τ_2) from the ternary system Al-Fe-Ti and FeSiTi (τ_2) from the ternary system.

The reported huge homogeneity range of the Laves phase Fe_2Ti towards the Ti-poor part of the quaternary system Al-Fe-Si-Ti proposed by Marker et al. **[10]**, can be already excluded by the presented partial isothermal section at 25 at.% Ti. In this section the Laves phase can only be observed in two-, three- and four-phase equilibria. Thereby, the SEM-results of the two-phase field samples (PB24-PB29, PB45-PB50 and PB51-PB55) show a maximal expansion of the Laves phase Fe_2Ti towards the Ti-poor side in a range of 27.9-29.5 at.% Ti. Furthermore, XRD-results report a distribution between the Fe_2Ti and the additional phase in a range of 1:9 to around 1:1. The observed homogeneity range of Fe_2Ti compared to the reported one by Marker et al. **[10]** is presented in Fig. 46.

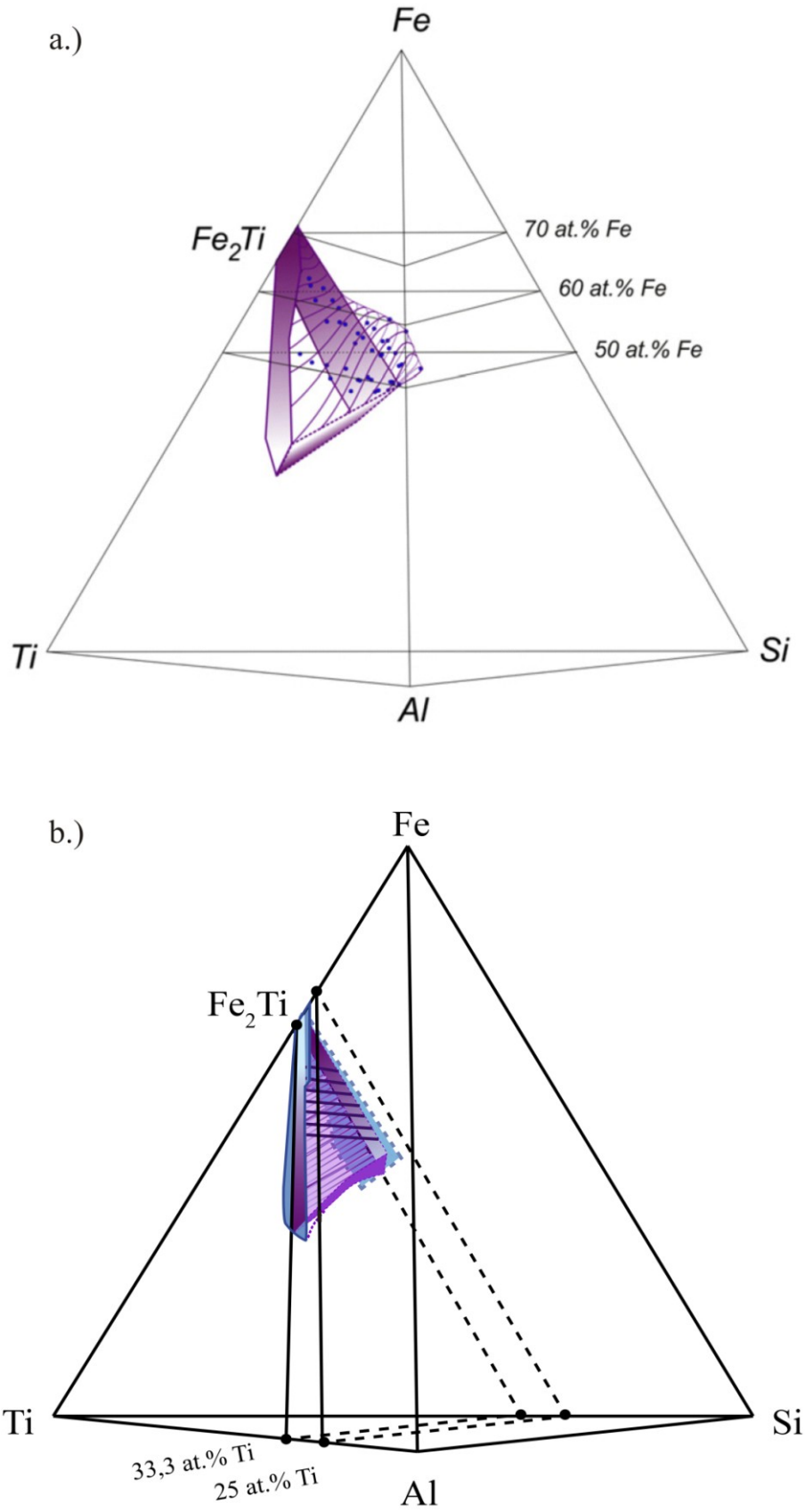

Fig. 46: a.) Homogeneity range of the Laves phase Fe_2Ti in the system Al-Fe-Si-Ti given by Marker et al. [10]; b.) Schematical depiction of the homogeneity range of the Laves phase Fe_2Ti in the system Al-Fe-Si-Ti as observed in the current work.

The already known data about the crystallographic positions and their occupancy of the Laves phase Fe_2Ti were already given in 6.1.1. Based on this data, the model (b) (**Fe**,Al,Si)$_2$(**Fe**,Al,Si)$_6$(**Ti**,Fe)$_4$, according to **[10],** should have been used. Refinements with this model (b) showed that the (**Ti**,Fe)$_4$ position was only occupied by Ti. For the investigations of the dependence of the site occupancies on composition for the Laves phase Fe_2Ti by addition of (Al+Si) the model (c) (**Fe**,Al,Si)$_2$(**Fe**,Al,Si)$_6$(**Ti**,Al,Si)$_4$ was used. In fact, the model c contradicts all known data for the occupancy mechanism of the crystallographic positions of the Laves phase Fe_2Ti based on binary and ternary investigations, but showed much better results. Using this model for the ternary systems Al-Fe-Ti and Fe-Si-Ti would cause a replacement of the Fe-atoms on the 4f position by Al- or Si-atoms. Additionally, it is not possible working with refinement models where more than two elements are situated at one crystallographic position. It would be necessary to apply model c on the ternary systems, to get an idea how it fits there. No literature data for using such a model for the Rietveld refinement in ternary systems for the Laves phase Fe_2Ti are reported up to date.

However, the model c was applied by fixing the Ti position 4*f* to a certain percentage for Ti and (Al+Si), respectively. Therefore, the SEM-results of the Laves phase Fe_2Ti of two-phase fields samples (PB24-PB29) were taken. Consequently, the 4*f* position was fixed with 87.5% Ti-atoms and 12.5% (Al+Si)-atoms, which corresponds to a Ti amount of 29 at.%. Due to the fact that no grain segregation for the Fe_2Ti phase was observed and consequently, the deviation of the measured compositions by SEM was minor, all results were plotted against the measured amount for (Al+Si). The observed dependence of the site occupancies on composition for the Laves phase Fe_2Ti by addition of different amounts of (Al+Si) is given in Fig. 47. The refined compositions (XRD) of each sample, compared with the measured ones (EDX) are listed in Table 19.

The deviation between the refined and the measured compositions is in a range between 0.1-3.7 at.% for (Al+Si). Except for PB29, all other calculated amounts for (Al+Si) are higher than the measured ones. Thereby, the Fe concentration, except in PB28 and PB29, decreases at constant Ti amount for each sample. Additionally, minor deviations especially for the Fe and Ti concentrations are observed, because of the used model for all samples.

Table 19: Comparison of refined (XRD) and measured (EDX) compositions.

Sample/ nom. Comp. (at.%)	Operation	(Al+Si) (at.%)	Fe (at.%)	Ti (at.%)
PB24 $Al_{4.15}Fe_{66.7}Si_{4.15}Ti_{25}$	EDX	8.6	62.4	29
	XRD	12	59	29
PB25 $Al_{6.15}Fe_{62.7}Si_{6.15}Ti_{25}$	EDX	12.1	59.2	28.7
	XRD	14.7	56.3	29
PB26 $Al_{8.15}Fe_{58.7}Si_{8.15}Ti_{25}$	EDX	16.2	55.8	29
	XRD	19.9	51.1	29
PB27 $Al_{10.15}Fe_{54.7}Si_{10.15}Ti_{25}$	EDX	19	52.8	28.2
	XRD	19.3	51.7	29
PaBe28 $Al_{12.15}Fe_{50.7}Si_{12.15}Ti_{25}$	EDX	22	48.6	29.4
	XRD	22.1	48.9	29
PB29 $Al_{14.15}Fe_{46.7}Si_{14.15}Ti_{25}$	EDX	26	44.8	29.2
	XRD	24.9	46.1	29

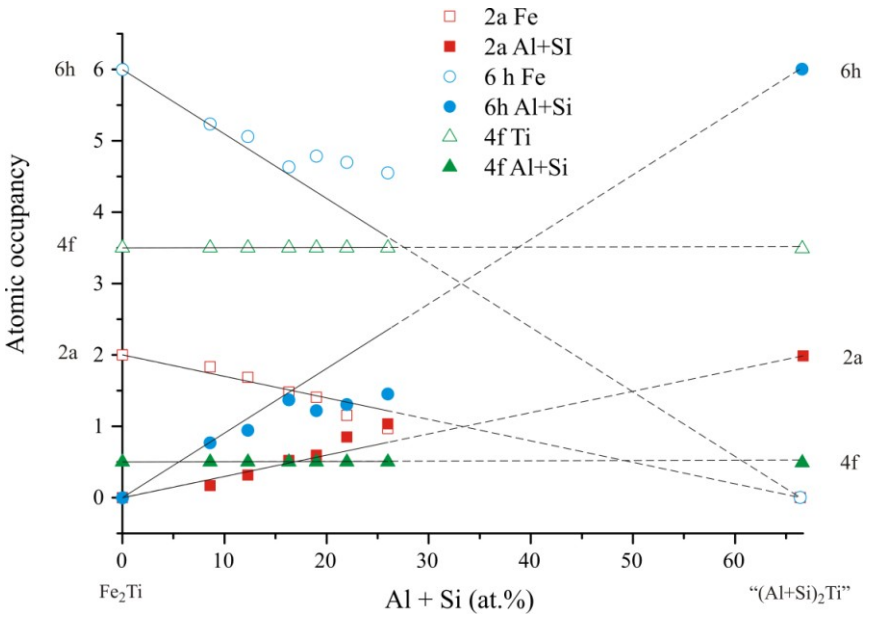

Fig. 47: Site occupancies in the Laves phase Fe_2Ti of the quaternary system Al-Fe-Si-Ti at 25 at.% Ti vs. measured comp. of (Al+Si).

Fig. 47 depicts the different behaviors for the occupancy of each crystallographic site of the Laves phase Fe_2Ti by addition of further elements. In model (c), the Ti amount was fixed to 87.5% and the (Al+Si) amount to 12.5% for position 4*f*, which is represented by a constant behavior in Fig. 47. The (Al+Si)-atoms show an average negative deviation from linearity up to 12.1 at.% (Al+Si) for the occupancy of the 2*a* position. An average positive

deviation from linearity is observed for higher amounts of (Al+Si). The occupancy of the 6*h* position for Al+Si describes a linear behavior up to 16.2 at.% (Al+Si) with a slight negative deviation, while a huge negative deviation is represented at higher amounts of the further elements. This results are mostly in good agreements with those of the 33.3 at.% Ti-section, where a negative deviation for the occupancy of the 6*h* position and a positive one for the 2*a* position for (Al+Si) at (Al+Si) concentrations up to 24 at.% was observed.

Based on Rietveld refinement data of the XRD-patterns of PB24-PB30 the lattice parameters *a* and *c* as well as the volume of the Laves phase were plotted against the amount of (Al+Si), see Fig 48. The results of the first multi-phase field were also included, marked with an open square. The lattice parameter *a* is increasing with increasing amounts of the additional elements, while the lattice parameter *c* shows a decreasing behavior. The lattice parameter *c* decreases at a lower rate than *a* increases, which can also be observed by the increasing volume with advancing amounts of (Al+Si). Compared to the results of the Laves phase Fe_2Ti at the 33.3 at.% Ti section, only the lattice parameter *c* shows a reverse trend.

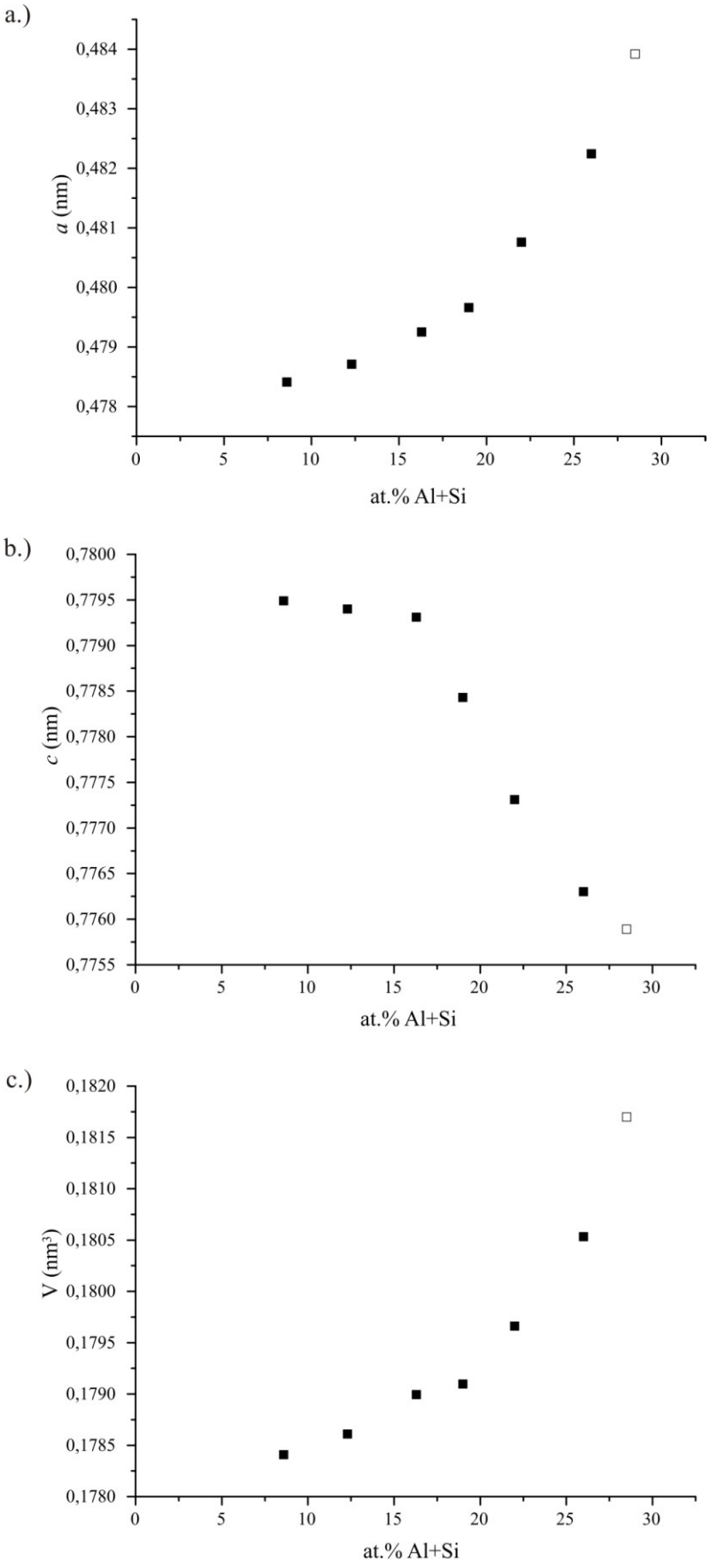

Fig. 48: Lattice parameters *a* and *c* as well as the volume of the Laves phase Fe_2Ti vs. measured comp. of (Al+Si).

6.1.3. 20 at.% Ti

The partial isothermal section at 20 at.% Ti of the quaternary system Al-Fe-Si-Ti is presented in Fig. 49. It contains the composition of all prepared samples at the 20 at.% Ti section annealed at 900 °C, the relevant phase equilibria of the ternary systems Al-Fe-Ti and Fe-Si-Ti, a schematical depiction of the two-phase fields A2/$D0_3$+Fe_2Ti and $D0_3$+Fe_2Ti as well as of the four-phase field B2+Al_2FeTi+FeSiTi+'$Al_4Fe_5Si_6Ti_5$'. The X-ray powder diffraction data and relevant SEM results for every sample are given in Table 20. The label for the different bcc-based modifications in the Fe-rich part of the ternary systems Al-Fe-Ti and Fe-Si-Ti is given as mentioned before.

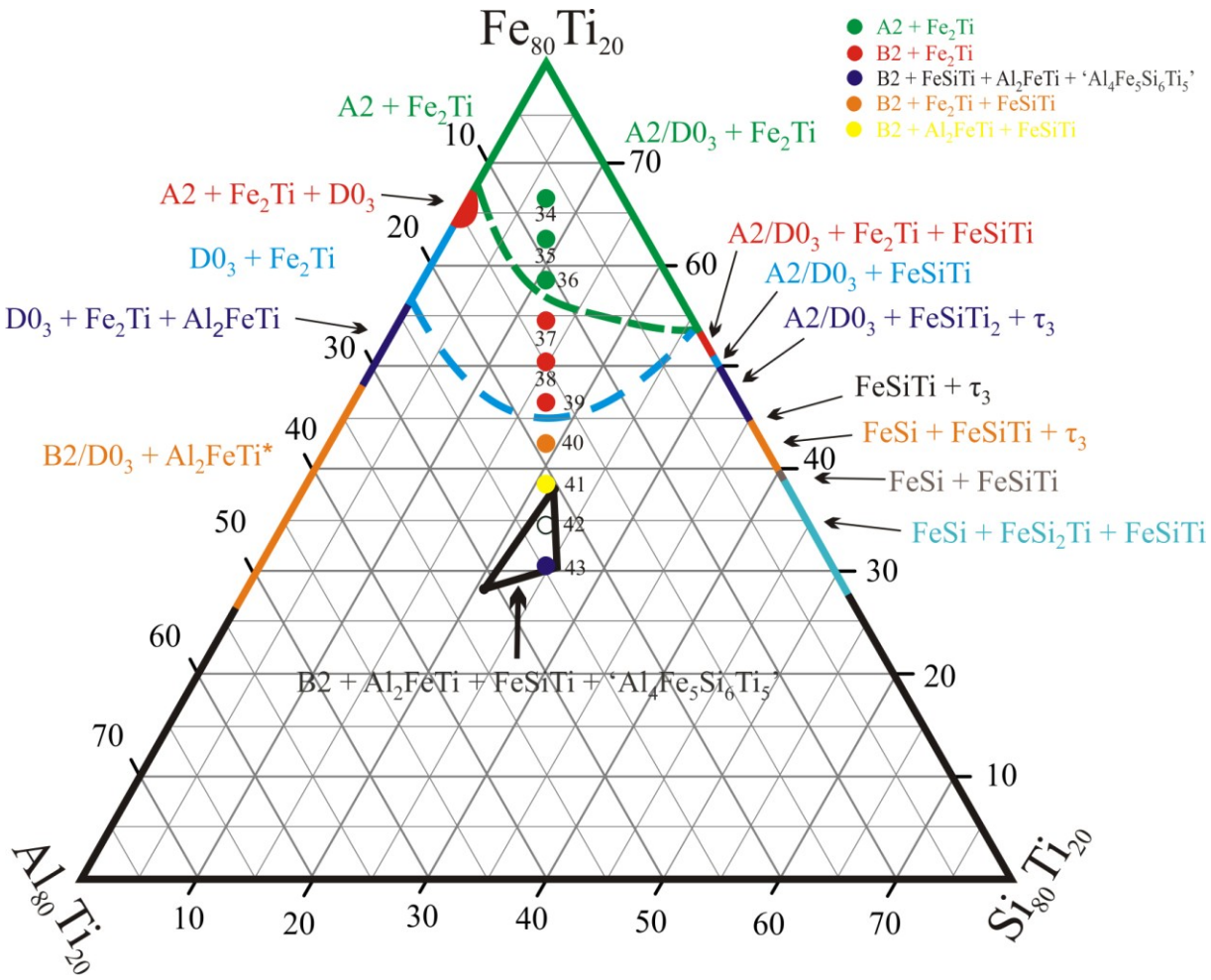

Fig. 49: Partial isothermal section of the quaternary system Al-Fe-Si-Ti at 20.at% Ti annealed at 900 °C. No distinction between A2/B2/$D0_3$ in the two-phase field A2/$D0_3$+ Fe_2Ti is given in the system Fe-Si-Ti, according to the literature. All samples in this two-phase field show A2 and Fe_2Ti. PB42, marked with an open circle, did not reach equilibrium.

Table 20: XRD and SEM results of the partial isothermal section at 20 at.% Ti at 900 °C of the quaternary system.

Sample/ nom. comp. (at.%)	Phase analysis			SEM			
	Phase	XRD Lattice parameter (Å)	XRD %	Al (at.%)	Fe (at.%)	SI (at.%)	Ti (at.%)
PB34 $Al_{6.65}Fe_{66.7}Si_{6.65}Ti_{20}$	Fe_2Ti	*a* = 4.7831(2)	75	3.8	58.4	9.4	28.4
		c = 7.7830(3)					
	A2	*a* = 2.8966(2)	25	13.3	82.0	0.5	4.2
PB35 $Al_{8.65}Fe_{62.7}Si_{8.65}Ti_{20}$	Fe_2Ti	*a* = 4.7856(1)	75	4.3	54.8	12.4	28.5
		c = 7.7743(3)					
	A2	*a* = 2.9009(2)	25	17.8	77.4	0.7	4.1
PB36 $Al_{10.65}Fe_{58.7}Si_{10.65}Ti_{20}$	Fe_2Ti	*a* = 4.7907(1)	71	5.1	51.7	15.0	28.2
		c = 7.7620(3)					
	A2	*a* = 2.9100(2)	29	23.0	71.2	1.1	4.7
PB37 $Al_{12.65}Fe_{54.7}Si_{12.65}Ti_{20}$	Fe_2Ti	*a* = 4.7964(1)	72	5.1	48.7	17.8	28.4
		c = 7.7431(2)					
	B2	*a* = 2.9045(2)	28	27.5	64.7	2.3	5.5
PB38 $Al_{14.65}Fe_{50.7}Si_{14.65}Ti_{20}$	Fe_2Ti	*a* = 4.8049(1)	70	5.6	45.7	20.4	28.3
		c = 7.7260(2)					
	B2	*a* = 2.9032(2)	30	32.0	58.4	3.3	6.3
PB39 $Al_{16.65}Fe_{46.7}Si_{16.65}Ti_{20}$	Fe_2Ti	*a* = 4.8157(9)	67	6.5	42.6	22.6	28.3
		c = 7.7068(2)					
	B2	*a* = 2.9027(2)	33	37.0	53.2	4.0	5.8
PB40 $Al_{18.65}Fe_{42.7}Si_{18.65}Ti_{20}$	Fe_2Ti	*a* = 4.967(2)	4	8.0	43.3	21.3	27.4
		c = 7.233(6)					
	B2	*a* = 2.9112(2)	50	37.2	52.2	3.4	7.2
	FeSiTi	*a* = 7.0037(5)	46	2.6	34.8	30.9	31.7
		b = 10.812(1)					
		c = 6.2862(6)					
PB41 $AL_{20.65}Fe_{38.7}Si_{20.65}Ti_{20}$	B2	*a* = 2.9022(1)	34	46.2	47.6	3.7	2.5
	Al_2FeTi	*a* = 11.762(2)	8	38.0	29.1	14.4	18.5
	FeSiTi	*a* = 7.0143(2)	58	1.2	32.6	32.7	33.5
		b = 10.8186(3)					
		c = 6.2817(2)					
PB43 $Al_{24.65}Fe_{30.7}Si_{24.65}Ti_{20}$	B2	*a* = 2.8900(3)	-	43.8	47.5	6.9	1.8
	Al_2FeTi	*a* = 11.709(2)	-	31.0	27.1	21.2	20.7
	FeSiTi	*a* = 7.049(2)	-	2.7	30.9	32.7	33.7
		b = 10.868(8)					
		c = 6.265(4)					
	'$Al_4Fe_5Si_6Ti_5$'	unknown structure	-	18.8	25.6	30.5	25.1

In the presented partial isothermal section at 20 at.% Ti (Fig. 49) two different two-phase fields are shown. They both contain the Laves phase Fe_2Ti and a bcc modification of the Fe-rich corner of the corresponding ternary systems. Their phase boundaries were schematically drawn according to the already known data of the ternary systems **[36, 41]**, and the received results during this work. Due to the fact that the homogeneity range of the Laves phase can already be described by the partial isothermal section at 25 at.% Ti no further samples were prepared in this section, except the given ones. Consequently, the phase boundaries were drawn based on only few samples.

All samples prepared in this section, except PB42, were homogenous, according to the SEM data. The samples PB34-PB39 are situated either in the two-phase field A2+Fe_2Ti or $D0_3$+Fe_2Ti, see Table 20. The distribution between the two phases for these samples is around 7:3, given by XRD-data. Thereby, the samples PB37-PB39 showed the unexpected B2 structure compared to the two-phase equilibra $D0_3$+Fe_2Ti of the ternary system Al-Fe-Ti, which was already discussed in 6.1.2.

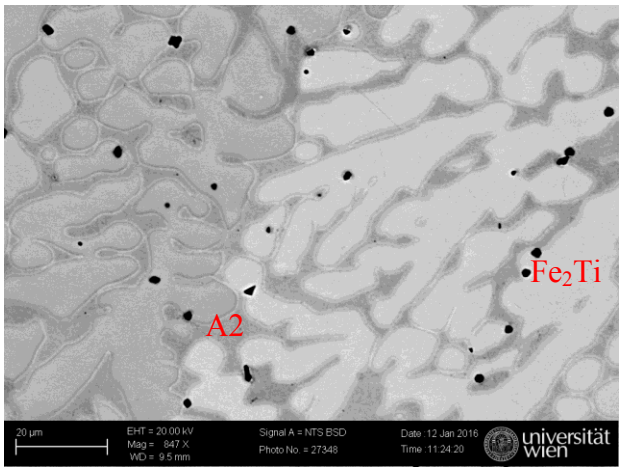

Fig. 50: SEM-image of PB36, showing Fe_2Ti and A2

The samples PB40 and PB41were observed to be in three-phase equilibria. They both contain FeSiTi (τ_2) from the ternary system Fe-Si-Ti, B2 and either Fe_2Ti for PB40 or Al_2FeTi (τ_2) from the ternary system Al-Fe-Ti for PB41. The sample PB43 is situated in a four-phase equilibrium. It shows the two ternary phases FeSiTi (τ_2) and Al_2FeTi (τ_2), B2 as well as an unknown structure (further referred to as $Al_4Fe_5Si_6Ti_5$), whose composition could be measured by SEM, see Table 20. Compared to the observed unknown structure in 6.1.1. and 6.1.2., the XRD-pattern of PB43 shows especially in 2Θ=20-50 a large number of additional diffraction lines, their occurrence are still under investigation. A SEM-image as well as the corresponding XRD-pattern is given in Fig. 51 and Fig. 52.

The homogeneity range of the Laves phase Fe_2Ti towards the Ti-poor side of the quaternary system Al-Fe-Si-Ti could already be confined by the 25 at.% Ti-section. In this section at 20 at.% Ti the Laves phase certainly can only exist in two- and three-phase

equilibria. SEM-results of the two-phase field samples (PB34-PB39) show a maximal expansion of the Laves phase towards the Ti-poor side in arange between 28.3-28.5 at.%, which is in good agreement with the results from 6.1.2. Moreover, the XRD-results show a distribution between the Laves phase Fe_2Ti and the additional phase of about 7:3, see Table 20.

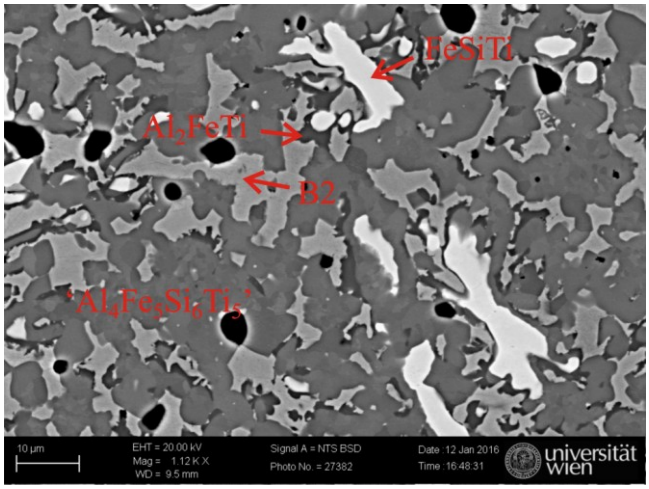

Fig. 51: SEM-image of PB43, showing the four phases B2, Al_2FeTi, FeSiTi and '$Al_4Fe_5Si_6Ti_5$'.

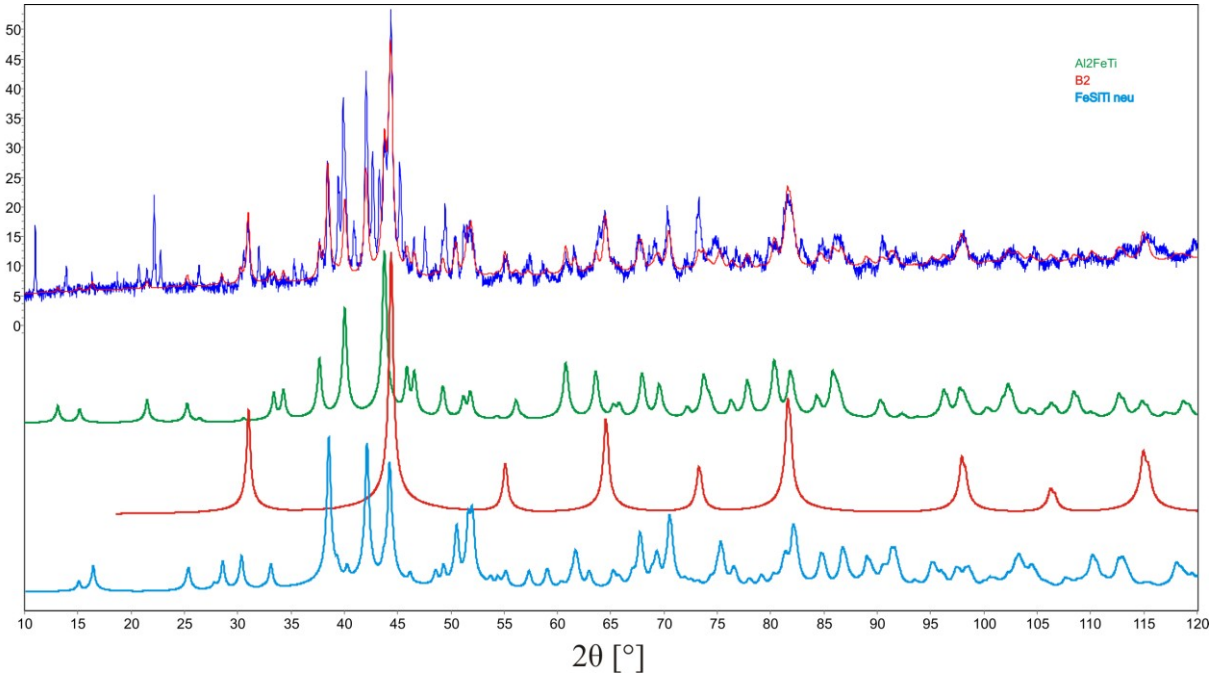

Fig. 52: XRD-pattern of sample PB43, showing the calculated structures and the diffraction lines of '$Al_4Fe_5Si_6Ti_5$'.

6.2. Powder pellets

As discussed before, the Laves phase showed pronounced grain segregation in many samples. This is problematic for the Rietveld refinement, as it causes severe line broadening, which cannot be modeled correctly with the fundamental parameter approach used here. It was tried to solve this problem by pressing powder pellets, which were re-annealed in an additional step.

35 powder pellets (PB9-PB43) were prepared and annealed with three consecutive different temperature programs, see Table 12. After the last annealing step, at which temperatures up to 1100 °C were reached, more than half of the powder pellets showed sintering effects. However, the expected decrease of the diffraction line width was only observed in a few samples.

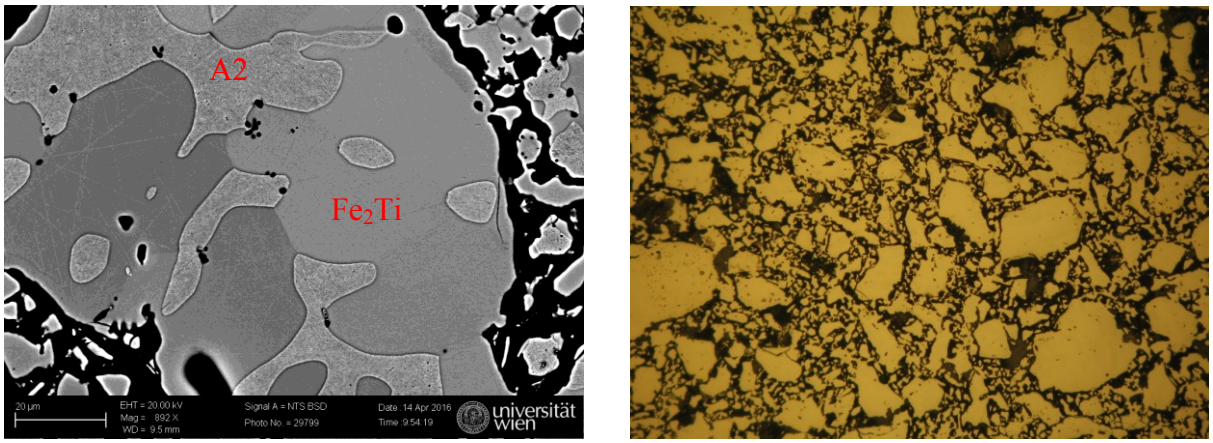

Fig. 53: Sample 24 (powder pellet); left: SEM-image; right: LOM-image.

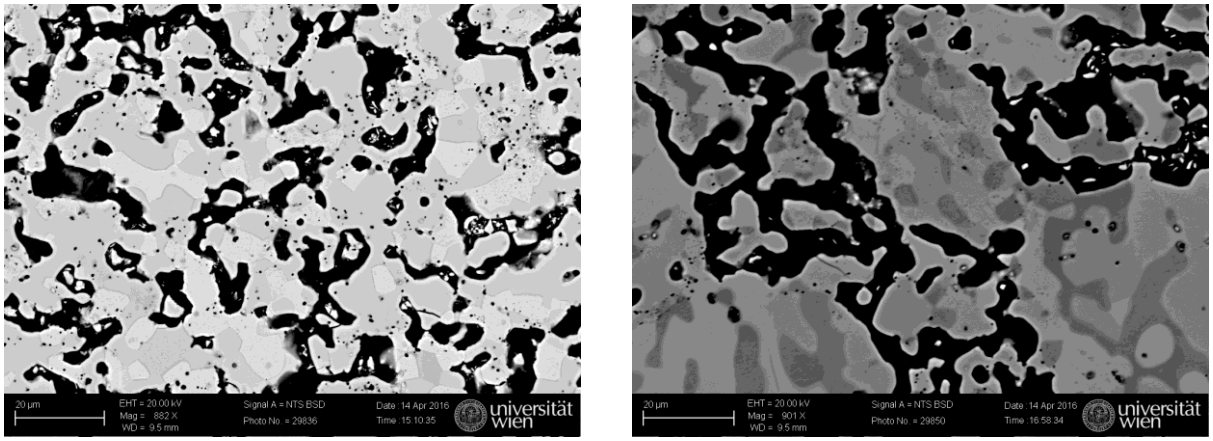

Fig. 54: SEM-images; left: PB34 (powder pellet); right: PB39 (powder pellet).

Good sintering was observed in the samples PB24-PB43. PB9-PB23, which are situated in the 33.3 at.% Ti section did not sintered well. So it was possible to produce surface grindings of the samples at the 20 and the 25 at.% Ti section, which were later on investigated by LOM and SEM. The results of the SEM-measurements showed an average negative deviation for the Al and Ti concentration and an average positive deviation for the Fe and Si concentration in each sample compared to the SEM-results of the pills. Selected samples for this observation are given in Table 21.

Table 21: Comparison of the composition of selected sample between the pills and the pellets.

Sample/ nom. comp. (at.%)	Phases	Form	Al	Fe	Si	Ti
			(at.%)	(at.%)	(at.%)	(at.%)
PB24 $Al_{4.15}Fe_{66.7}Si_{4.15}Ti_{25}$	Fe_2Ti	pill	3.4	62.4	5.2	29.0
		pellet	1.2	63.5	6.1	29.2
	A2	pill	10.5	84.8	0.0	4.7
		pellet	3.1	92.5	0.5	3.9
PB26 $Al_{8.15}Fe_{58.7}Si_{8.15}Ti_{25}$	Fe_2Ti	pill	5.7	55.8	9.5	29.0
		pellet	2	57.1	13.3	27.6
	A2	pill	21.2	71.4	0.2	7.2
		pellet	9.3	86.9	1.5	2.3
PB34 $Al_{6.65}Fe_{66.7}Si_{6.65}Ti_{20}$	Fe_2Ti	pill	3.8	58.4	9.4	28.4
		pellet	1.3	57.3	13.9	27.5
	A2	pill	13.3	82.0	0.5	4.2
		pellet	6.1	88.8	2.4	2.7
PB36 $Al_{10.65}Fe_{58.7}Si_{10.65}Ti_{20}$	Fe_2Ti	pill	5.1	51.7	15.0	28.2
		pellet	2.9	53.5	17.0	26.6
	A2	pill	23.0	71.2	1.1	4.7
		pellet	14.7	80.4	2.6	2.3

It was found that the mass loss of the powder pellets after annealing were in a range between 0-11 mass%. Moreover some of the pellets showed bright metallic shiny spots at the bottom, which perhaps indicate partial melting at these high temperatures. Also the used quartz glass tubes were misted up with metallic shiny coating. Because of these observations, the powder pellets were not investigated further.

6.3. Fe-Si-Ti

The partial isothermal section of the ternary system Fe-Si-Ti is presented in Fig. 55, according to **[41]**. It contains the composition of all prepared samples annealed at 900 °C. The X-ray powder diffraction data as well as the SEM results for every sample are given in Table 22.

Investigations on the ternary system Fe-Si-Ti were primarily done to study the dependence of the site occupancies on the composition for the Laves phase Fe_2Ti by the addition of different amounts of Si at a constant Ti amount of 33.3 at.%. The phase equilibria at the Ti-rich side of the Laves phase were checked by a sample series at 42 at.% Ti. Furthermore, the two ternary phases τ_7 and τ_8, reported by **[41]**, with a nominal composition of $Fe_{10}Si_{40}Ti_{50}$ (τ_7) and $Fe_{20}Si_{40}Ti_{40}$ (τ_8) were prepared, to determine their structure, respectively.

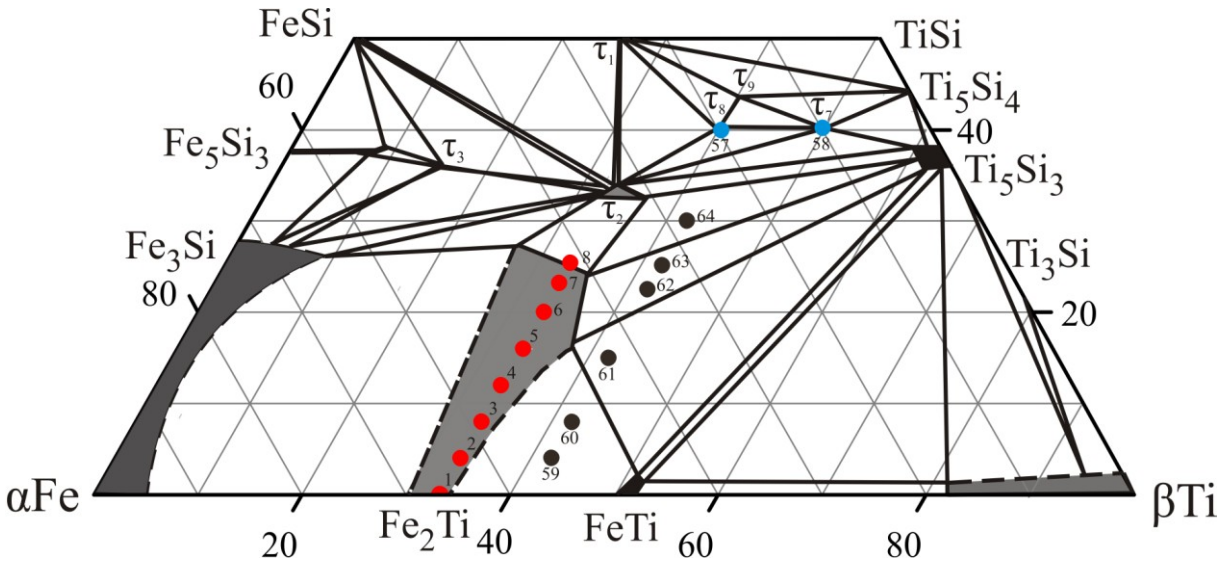

Fig. 55: Partial isothermal section of the ternary system Fe-Si-Ti, according to Weitzer et al. [41].

Table 22: XRD and SEM results of the partial isothermal section at 900 °C of the ternary system.

Sample/ nom. comp. (at.%)	Phase analysis			SEM		
	Phase	XRD Lattice parameter (Å)	XRD %	Fe (at.%)	SI (at.%)	Ti (at.%)
PB01 $Fe_{66.7}Ti_{33.3}$	Fe_2Ti	a = 4.7925(5)	100	66.1	-	33.9
		c = 7.8238(1)				
PB02 $Fe_{62.7}Si_4Ti_{33.3}$	Fe_2Ti	a = 4.7922(6)	99*	60.7	5.3	34
		c = 7.8169(1)				
PB03 $Fe_{58.7}Si_8Ti_{33.3}$	Fe_2Ti	a = 4.7935(6)	99*	57.2	8.8	34
		c = 7.8078(1)				
PB04 $Fe_{54.7}Si_{12}Ti_{33.3}$	Fe_2Ti	a = 4.7966(6)	99*	52.5	13.6	33.9
		c = 7.7932(1)				
PaBe05 $Fe_{50.7}Si_{16}Ti_{33.3}$	Fe_2Ti	a = 4.8019(7)	99*	49.9	16	34.1
		c = 7.7714(2)				
PB06 $Fe_{46.7}Si_{20}Ti_{33.3}$	Fe_2Ti	a = 4.8080(5)	99*	45.7	20.3	34
		c = 7.7492(1)				
PB07*** $Fe_{42.7}Si_{24}Ti_{33.3}$	Fe_2Ti	a = 4.8157(5)	-	42.3	23.8	33.9
		c = 7.7165(1)				
PB08*** $Fe_{40.7}Si_{26}Ti_{33.3}$	Fe_2Ti	a = 4.8184(5)	-	40.9	25.4	33.7
		c = 7.7018(1)				
PB57 $Fe_{10}Si_{40}Ti_{50}$	τ_7	unknown structure	-	9.0	39.7	51.3
	τ_8	unknown structure	-	19.6	40.3	40.1
	Ti_5Si_3	-	-	1.7	37.7	60.6
PB58 $Fe_{20}Si_{40}Ti_{40}$	τ_7	unknown structure	-	10.2	39.6	50.2
	τ_8	unknown structure	-	20.0	39.1	40.9
	FeSiTi	-	-	31.8	34.1	34.1
PB58i $Fe_{20}Si_{40}Ti_{40}$	τ_7	unknown structure	-	10.6	39.4	50.0
	τ_8	unknown structure	-	19.6	39.2	41.2
	Ti_5Si_3	-	-	4.8	36.8	58.4
PB59 $Fe_{54}Si_4Ti_{42}$	Fe_2Ti	a = 4.8029(1)	54	57.1	7.3	35.6
		c = 7.8221(3)				
	FeTi	a = 2.9783(10)	46	48.6	0.6	50.8
PB60 $Fe_{50}Si_8Ti_{42}$	Fe_2Ti	a = 4.8130(1)	55	51.6	12.3	36.1
		c = 7.8098(3)				
	FeTi	a = 2.9795(10)	45	47.4	1.5	51.1

Sample/ nom. comp. (at.%)	Phase analysis			SEM		
	Phase	XRD Lattice parameter (Å)	XRD %	Fe (at.%)	SI (at.%)	Ti (at.%)
PB61 $Fe_{43}Si_{15}Ti_{42}$	Fe_2Ti	a = 4.8276(10)	64	47.0	15.5	37.5
		c = 7.8095(2)				
	FeTi**	a = 2.9829(2)	25	-	-	-
	Ti_5Si_3**	a = 7.431(2)	11	-	-	-
		c = 5.170(3)				
PB62 $Fe_{35.5}Si_{22.5}Ti_{42}$	Fe_2Ti	a = 4.8202(10)	72	46.1	17.9	36.0
		c = 7.7806(2)				
	Ti_5Si_3	a = 7.4388(4)	28	3.0	35.8	61.2
		c = 5.1448(4)				
PB63 $Fe_{33}Si_{25}Ti_{42}$	Fe_2Ti	a = 4.8173(7)	74	44.1	19.9	36.0
		c = 7.7515(1)				
	Ti_5Si_3	a = 7.4404(2)	26	4.3	35.0	60.7
		c = 5.1455(2)				
PB64 $Fe_{28}Si_{30}Ti_{42}$	Fe_2Ti	a = 4.8194(8)	50	42.0	22.2	35.8
		c = 7.7220(2)				
	Ti_5Si_3	a = 7.4354(3)	27	3.9	36.4	59.7
		c = 5.1383(3)				
	FeSiTi	a = 6.9884	23	29.9	32.7	37.4
		b = 10.9479(6)				
		c = 6.3277(3)				

*Traces of FeTi were found

**Could not be measured by SEM

***unknown impurity phase

Table 23: Relevant crystal structure data of the binary and ternary phases for the partial isothermal section.

Phases	Lattice parameters (Å)	Structure type	Strukturbericht designation	Space group	Reference
Fe_2Ti	a = 4.787	$MgZn_2$	C14	$P6_3/mmc$	**[61]**
	c = 7.815				
FeTi	a = 2.976	CsCl	B2	$Pm3m$	**[62]**
FeSiTi	a = 6.997	FeSiTi	-	$Ima2$	**[39]**
	b = 10.83				
	c = 6.287				
Si_3Ti_5	a = 7.448	Mn_5Si_3	$D8_8$	$P6_3/mmc$	**[69]**
	c = 5.114				

All samples prepared in the ternary system Fe-Si-Ti are more or less homogeneous. The samples PB2-PB8, which are situated in the single-phase field Fe_2Ti, contain traces of FeTi. This phenomen already occurred in the partial isothermal section at 33.3 at.% Ti of the quaternary system Al-Fe-Si-Ti. XRD results showed an average amount of less than 1 % of FeTi. The given SEM-image (Fig. 56) is similar to the one of PB9, presented in 6.1.1. It also depicts small areas of FeTi contamination on the boundaries of the grains. For the investigation of the dependence of the site occupancies on the composition for the Laves phase Fe_2Ti by addition of Si, this observation can be neglected, as FeTi was found only in a minor amount.

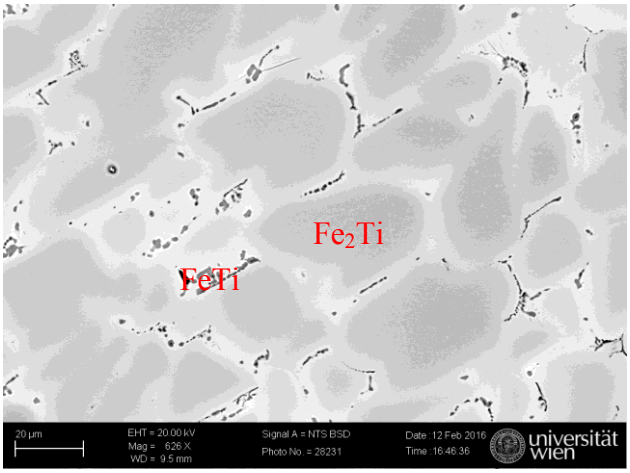

Fig. 56: SEM-image of PB3, showing Fe_2Ti and traces of FeTi. Also the effect of grain segregation can be observed.

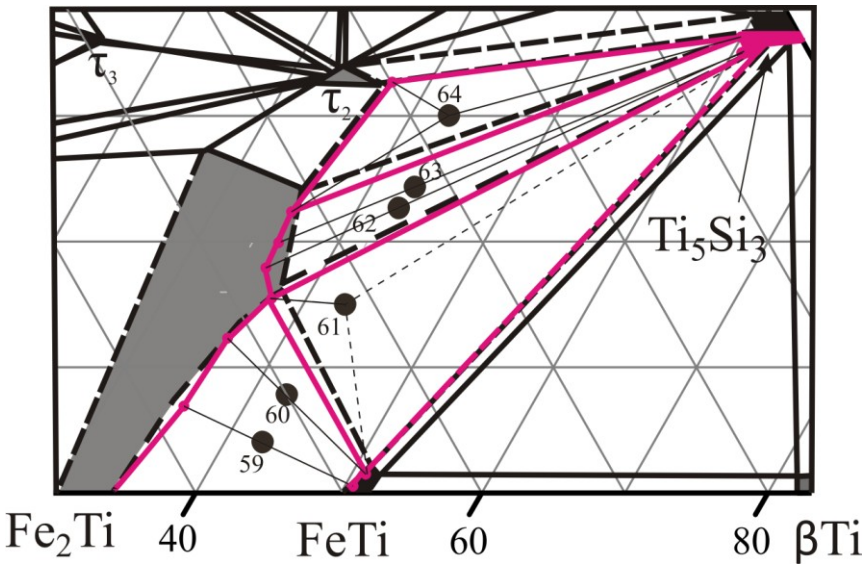

Fig. 57: Comparison of a partial section of the Fe-Si-Ti system at 900 °C, done by Weiter et al. [41], and observed in this work (marked pink).

The phase equilibra on the Ti-rich side of the Laves phase Fe_2Ti presented by Weitzer et al. **[41]** could be approximately confirmed, see Fig. 57. Along the sample series at a constant Ti amount of 42 at.% up to a Si concentration of 30 at.% the two two-phase fields Fe_2Ti+FeTi and Fe_2Ti+Ti_5Si_3 as well as the two three-phase fields Fe_2Ti+FeTi+Ti_5Si_3 and Fe_2Ti+Ti_5Si_3+FeSiTi were observed. The respective XRD and SEM results are given in Table 22. The major differences between the partial sections of the ternary system Fe-Si-Ti reported

by Weitzer et al. **[41]** and the one given in the current work are the solid solubilities of the phases Ti_5Si_3 and Fe_2Ti. The solid solubility for Ti_5Si_3 compared to **[41]**, was found to be about 2 at.% larger with respect to the Fe-concentration. The solid solubility of the Fe_2Ti phase at Si-concentrations below 15.5 at.% differs by max. 1 at.% with respect to the Ti-concentration. At Si-concentrations between 15.5 and 22 at.%, the solid solubility for Ti of the Laves phase decreases by max. 2 at.%. The Laves phase in sample PB64 showed a maximal solid solubility of 22 at.% Si at 36 at.% Ti. This differs from the reported one **[41]** by 2 at.% Si.

The maximal solid solubility of the Laves Phase Fe_2Ti for Si at a constant Ti concentration in the ternary system Fe-Si-Ti was investigated. Therefore, a sample series at a constant amount of 33.3 at.% Ti with a maximal amount of 26 at.% Si was prepared (PB1-PB8). Except the minor FeTi contamination, the single phase field Fe_2Ti extends at least up to 26 at.% Si. The XRD patterns of the samples PB7 and PB8 showed, two additional diffraction lines, at 2Θ=25.75 and 2Θ=27.5. The additional diffraction lines could not be assigned to any ternary phases in the vicinity of the sample composition. SEM investigations on these two samples exhibit a rather similar image according to Fig 56. Nevertheless, the extent of the contamination or the 'additional' phase on the boundaries of the Fe_2Ti grains is somewhat larger. The refined XRD-pattern, with the corresponding structures of the 'single-phase' sample PB6 is given in Fig 58.

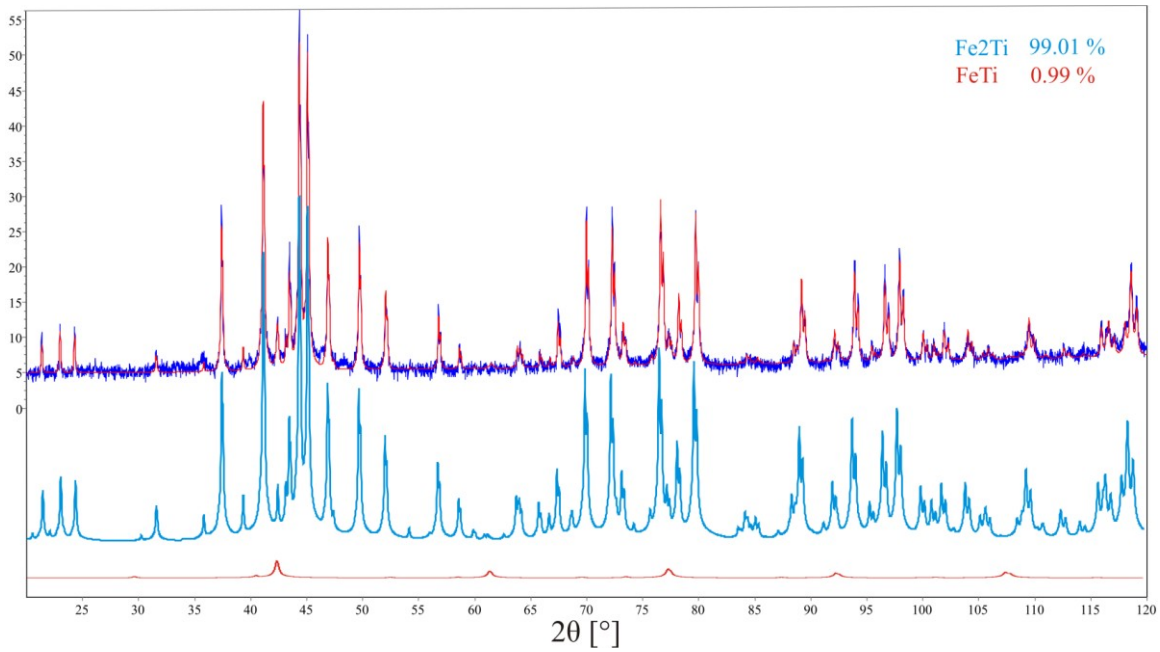

Fig. 58: XRD-pattern of PB6, showing the calculated structures Fe_2Ti and FeTi.

In Fig. 59, the refined XRD-pattern of PB8 is presented. It shows, as mentioned before, two additional diffraction lines, which are marked by black arrows. Compared to the pattern of sample PB6, the phase Fe_2Ti also prevails in PB8 and minor amount of FeTi was found.

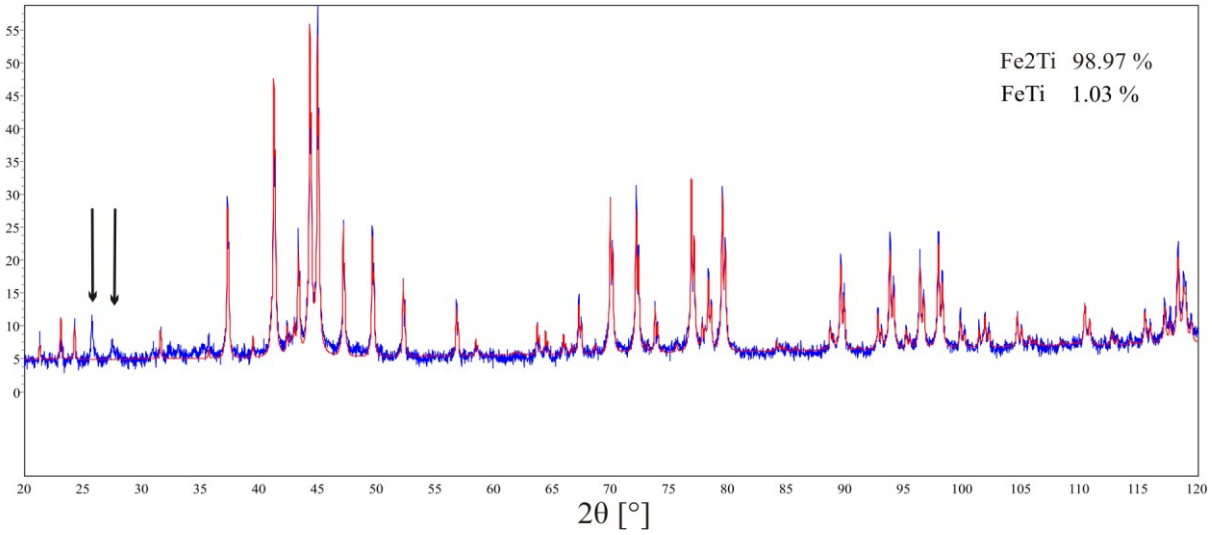

Fig. 59: XRD-pattern of sample PB8, showing the calculated structures and the unknown diffraction peaks, marked with black arrows.

Grain segregation was observed in all samples, except PB1, situated in the single phase field Fe_2Ti of the ternary system Fe-Si-Ti. This effect was investigated in more detail on the sample PB6. The observed results are given in Fig 60. It shows that the Fe concentrations decreases towards the grain center, while the Si concentrations increases. However, the Ti concentrations almost stay constant. (Grain segregation reduces the quality of Rietveld refinements and SEM-measurements.)

Due to the fact, that the contamination of PB7 and PB8 was observed to be small, they were included for further investigations on the dependence of the site occupancies on composition for the Laves phase Fe_2Ti by addition of Si. The already known data about the crystallographic positions and their occupancy of the Laves phase Fe_2Ti were already given in 6.1.1. The dependence of the site occupancies on composition for the Laves phase Fe_2Ti by addition of Si was investigated using the model $(\mathbf{Fe},Si)_2(\mathbf{Fe},Si)_6(\mathbf{Ti})_4$, which is in agreement with the stoichiometry. The observed dependence of the site occupancy for the Fe_2Ti by addition of different amounts of Si is given in Fig. 61. The refined compositions (XRD) of each sample, compared with the nominal compositions are listed in Table 24.

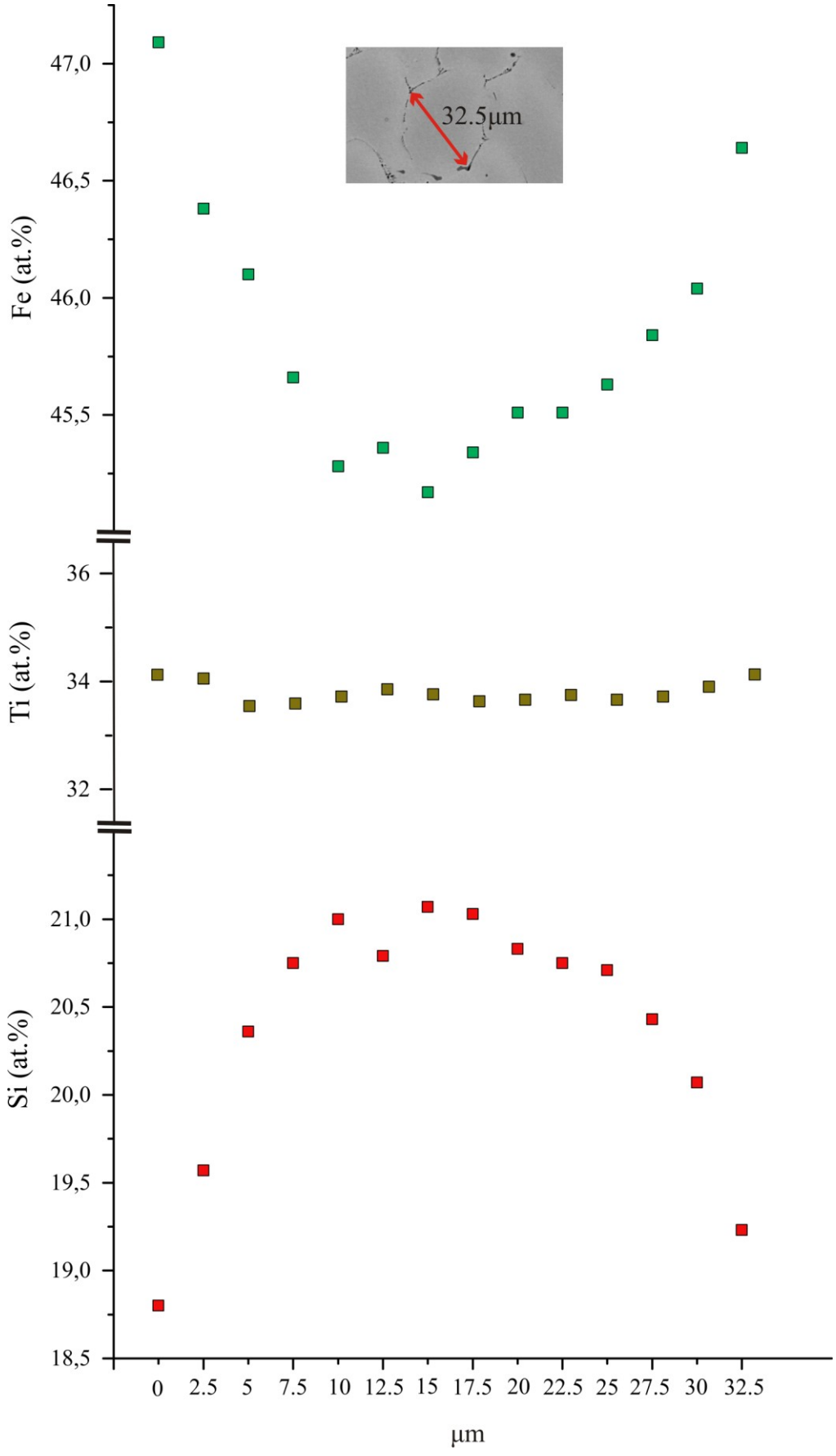

Fig. 60: Concentration profile within a Fe_2Ti grain in PB6.

Table 24: Comparison between the nominal and the refined compositions.

Sample/ nom. comp. (at.%)	Operation	Si	Fe	Ti
		(at.%)	(at.%)	(at.%)
PB02 $Fe_{62.7}Si_4Ti_{33.3}$	nom. comp.	4	62.7	33.3
	XRD	8.2	58.5	33.3
PB03 $Fe_{58.7}Si_8Ti_{33.3}$	nom. comp.	8	58.7	33.3
	XRD	9.9	56.8	33.3
PB04 $Fe_{54.7}Si_{12}Ti_{33.3}$	nom. comp.	12	54.7	33.3
	XRD	11.7	55	33.3
PaBe05 $Fe_{50.7}Si_{16}Ti_{33.3}$	nom. comp.	16	50.7	33.3
	XRD	15.5	51.2	33.3
PB06 $Fe_{46.7}Si_{20}Ti_{33.3}$	nom. comp.	20	46.7	33.3
	XRD	21.3	45.4	33.3
PB07 $Fe_{42.7}Si_{24}Ti_{33.3}$	nom. comp.	24	42.7	33.3
	XRD	22.3	44.4	33.3
PB08 $Fe_{40.7}Si_{26}Ti_{33.3}$	nom. comp.	26	40.7	33.3
	XRD	28	38.7	33.3

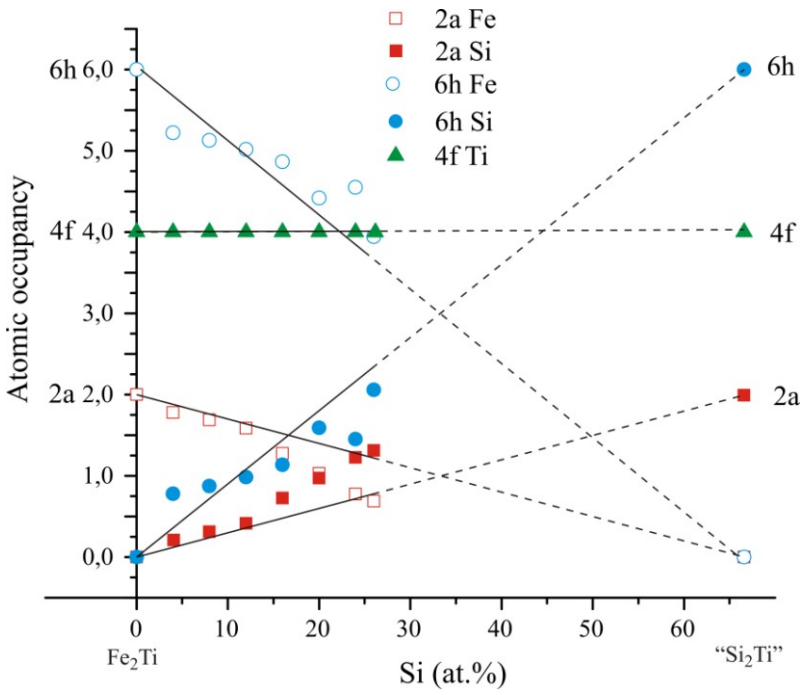

Fig. 61: Site occupancies of the Laves phase Fe_2Ti of the ternary system Fe-Si-Ti vs. nom. comp. of Si.

The refined compositions, obtained by Rietveld refinement show especially in the Si-poor samples a deviation of the nominal composition, which could be connected to the difficulties with grain segregation. In a range between 12 and 20 at.% Si they almost fit

perfectly. Fig. 61 describes an average positive deviation of linearity for the occupancy of the 2*a* Fe-position for Si-atoms. The occupancy of the 6*h* position for Si-atoms shows almost a good fit to linearity with a slight negative deviation in a range of 12-20 at.%. Below 12 at.% Si a positive and above 20 at.% Si a large negative deviation from linearity is observed. This behavior is certainly confirmed by the refined compositions, see Table. 24. Xinlin Yan et al. **[51]** reported a slight deviation from linearity for the dependence of the side occupancy of the 2*a* and 6*h* position by Al-atoms. Thereby, the 2*a* position is preferentially occupied by Al-atoms compared to the 6*h* position at low Al content. During this work an equal trend was observed for the dependence of the site occupancies on the Si concentration for the Laves phase Fe_2Ti in the ternary system Fe-Si-Ti.

According to the Rietveld refinement data of the samples PB1-PB8 the lattice parameters *a* and *c* as well as the volume of the Laves phase Fe_2Ti were plotted against the concentration of Si (see Fig. 62). While the lattice parameter *a* is increasing with increasing Si-concentrations, the lattice parameter *c* shows a decreasing behavior with increasing Si concentrations. The volume decreases approximately linear with increasing Si-concentration. Compared to the results for the lattice parameters *a* and *c* of the Fe_2Ti in the ternary system Al-Fe-Ti **[51]**, the increasing behavior of *a* with increasing amounts of a third element can be confirmed. However, the decreasing behavior of lattice parameter *c* of Fe_2Ti in the ternary system Fe-Si-Ti shows exactly the reverse trend, as reported for the ternary system Al-Fe-Ti **[51]**. This observation can be readily explained by comparing the atomic radii of aluminium, iron and silicon. Aluminium has an atomic radius of 143.1 pm, which is bigger, compared to the one of iron (124.1 pm). Therefore, the cell volume increase, when iron is substituted with aluminium. However, for silicon the opposite is the case, as the atomic radius of silicon is only 117 pm **[70]**.

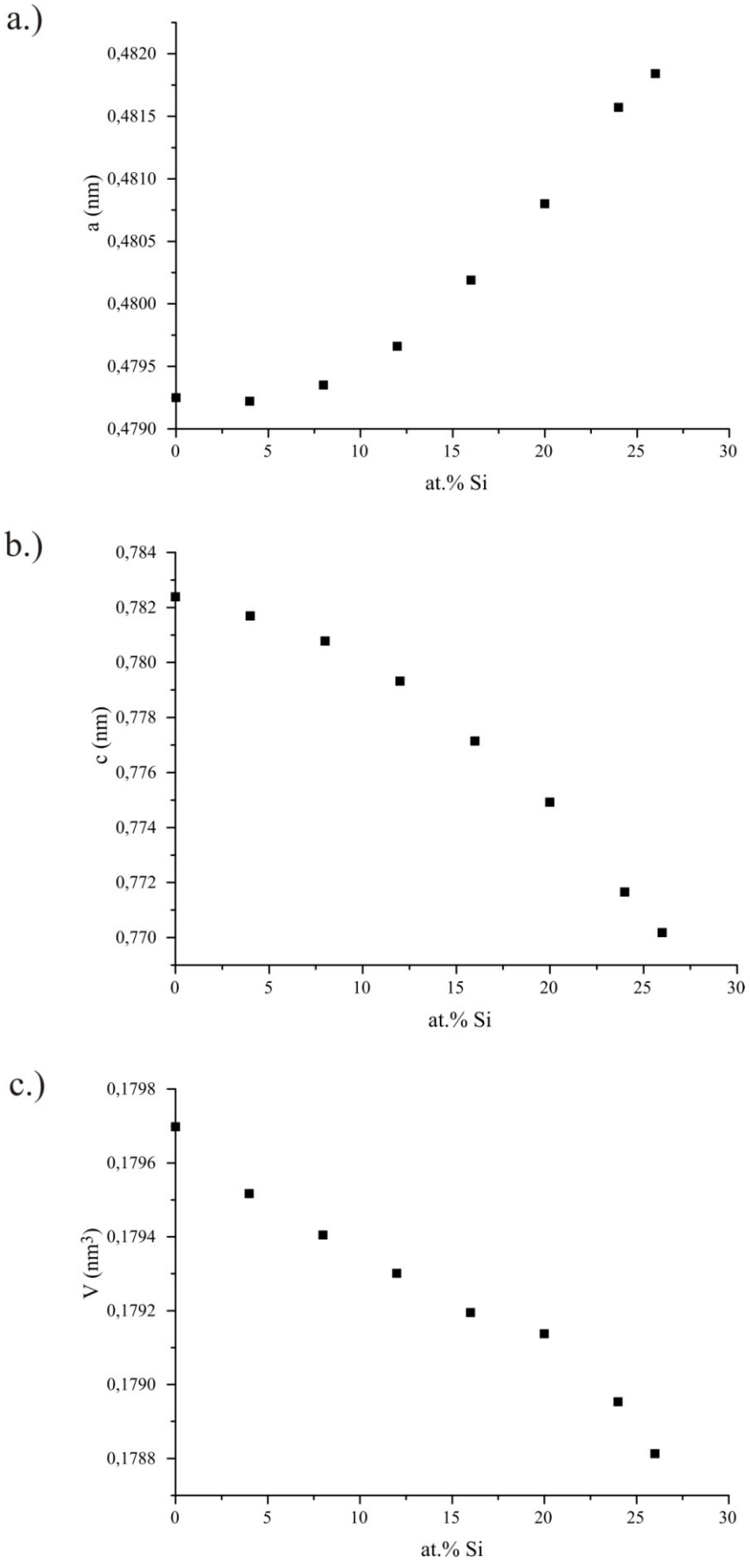

Fig. 62: Lattice parameters *a* and *c* as well as the volume of the Laves phase Fe_2Ti vs. nom. comp. of Si.

6.3.1. $Fe_{10}Si_{40}Ti_{50}$ (τ_7) and $Fe_{20}Si_{40}Ti_{40}$ (τ_8)

Weitzer et al. **[41]** reported the two ternary phases τ_7 and τ_8, whose crystal structures are still unknown, but their compositions were measured by SEM/EDX investigations. Thereby, τ_8 occurs from a peritectic reaction at 1640 °C ($L+Ti_5Si_3+ \tau_2= \tau_8$), while no further details for the formation of τ_7 were presented. To investigate their crystal structures, two samples with the nominal composition $Fe_{10}Si_{40}Ti_{50}$ (PB57) and $Fe_{20}Si_{40}Ti_{40}$ (PB58) were prepared and annealed at 900 °C and 1100 °C, respectively. Furthermore, another sample with the nominal composition$Fe_{20}Si_{40}Ti_{40}$ (PB58i) was produced and annealed for two hours at 1400 °C by an induction furnace. The obtained results are given in Table 22.

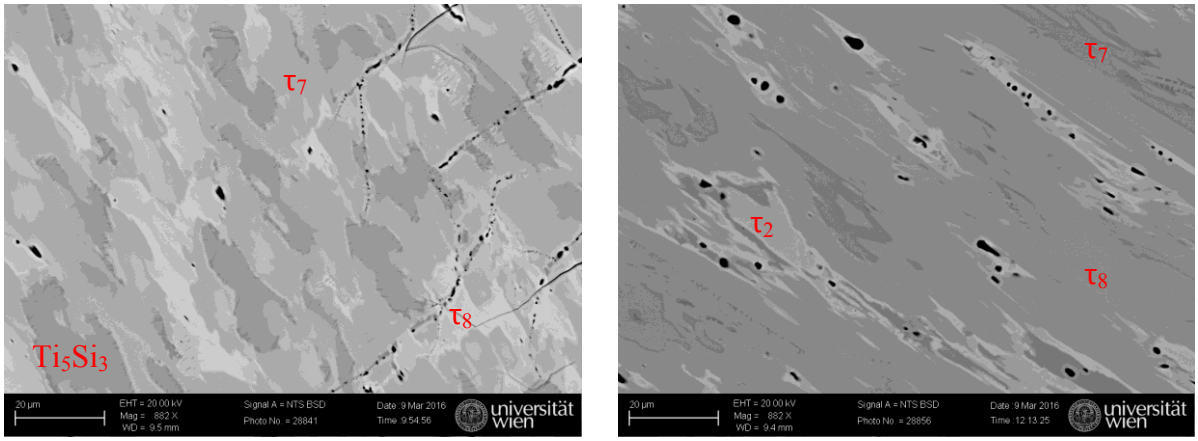

Fig. 63: SEM images; left: PB57 annealed at 900 °C; right: PB58 annealed at 1100 °C

The SEM-images of PB57 and PB58 are given in Fig. 63. No dependence of the annealing temperatures (900/1000 °C) was observed for both of them. They both contain three phases, whereby PB57 shows τ_7, τ_8 and Ti_5Si_3 and PB58 τ_7, τ_8 and FeSiTi (τ_2). Non equilibrium in both samples is evident. Further homogenization using powder pellets as well as higher temperatures and longer annealing times may be necessary to obtain single-phase equilibrium.

The sample PB58i shows predominantly the phase τ_8. SEM-images as well as LOM-images exhibit a small amount of τ_7 and Ti_5Si_3 in the center of the pills (Fig. 64). Therefore, a small piece from the edge of the pills were taken, powdered and investigated by XRD. The obtained XRD-pattern is given in Fig. 65. An indexation of all peaks was not possible. Due to the fact, that the grains of τ_8 were quite small, single crystal XRD investigation was impossible. The crystal structures of τ_7 and τ_8 are still under investigation.

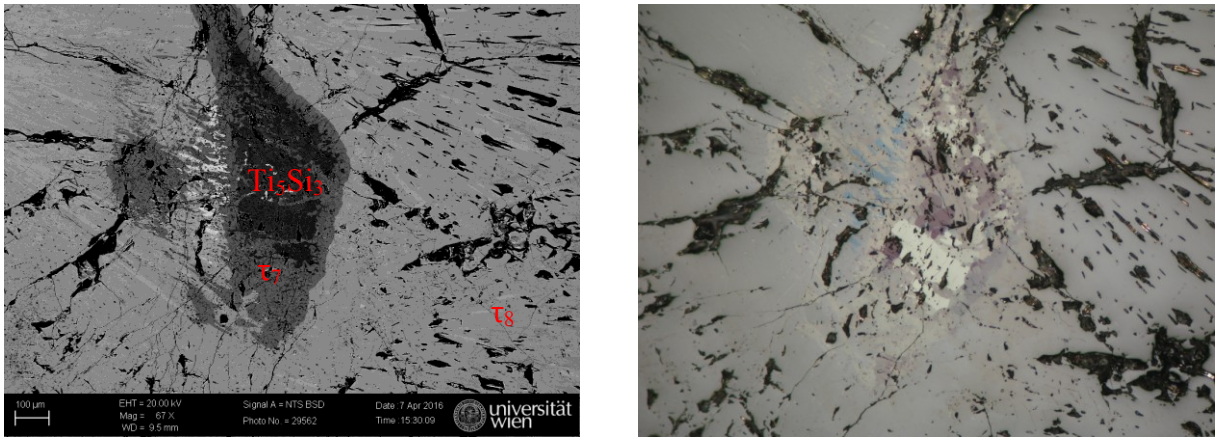

Fig. 64: Sample PB58i; right: SEM-image; left: Polarisation image (LOM)

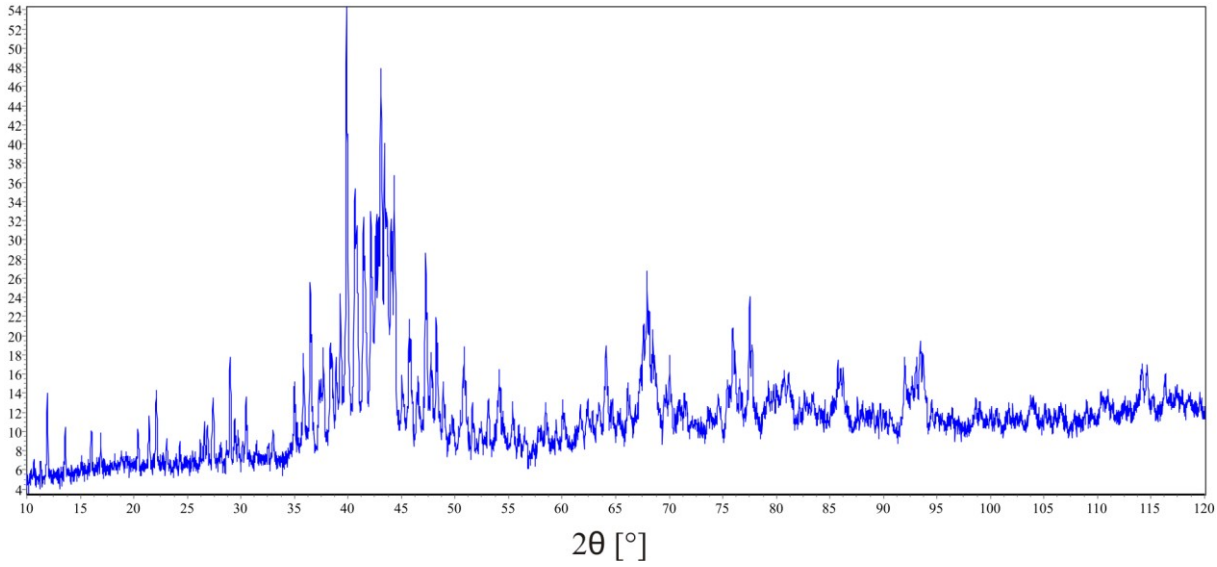

Fig. 65: XRD-pattern of PB58i.

7. Abstract

In order to characterize the homogeneity range of the Laves phase Fe_2Ti (C14) in the quaternary system Al-Fe-Si-Ti three partial isothermal sections at 900 °C, at constant titanium concentrations of 20, 25 and 33.3 at.%, were investigated by powder X-ray diffractometry (XRD), scanning electron microscopy (SEM) and optical microscopy. Additionally, the dependence of the site occupancies on the composition of the Laves phase Fe_2Ti by addition of Si, respectively, Al and Si was studied by Rietveld refinement of powder diffraction data for the quaternary system Al-Fe-Si-Ti as well as the ternary system Fe-Si-Ti. The lattice parameters *a* and *c* as well as the corresponding volume of the Laves phase was investigated with regard to the solubility of Si and Al.

The homogeneity range of the Laves phase Fe_2Ti in the quaternary system Al-Fe-Si-Ti at the 33.3 at.% Ti-section is limited by the according ternary homogeneity ranges of the Al-Fe-Ti and the Fe-Si-Ti systems at 900 °C and an approximately linear phase boundary through the quaternary system. The spatial extent towards the titanium-poor side was observed to be around 4 at.%, i.e. to a composition of around 29 at.% Ti. In the 25 at.% Ti-section, the Laves phase can only be found in two-, three- and four-phase equilibria.

The lattice parameters *a* and *c,* as well as the volume of the Laves phase Fe_2Ti in the quaternary system Al-Fe-Si-Ti increase with increasing concentrations of aluminium and silicon, with a ratio of 1:1 at the 33.3 at.% Ti-section. These results are in good agreement with the data of the ternary system Al-Fe-Ti **[51]**. Compared to the ternary system Fe-Si-Ti, where the lattice parameter *a* increases with increasing amounts of silicon, while the lattice parameter *c* as well as the volume is decreasing with increasing amounts of the other element, a reverse trend was observed.

Investigations on the dependence of the site occupancies on the composition of the Laves phase Fe_2Ti in the quaternary system Al-Fe-Si-Ti by addition of aluminium and silicon, with a ratio of 1:1, showed a slight deviation from linearity. Thereby, a positive deviation for the substitution of the 2*a* iron position by (Al+Si) was observed, while the 6*h* iron position shows a negative deviation from linearity. This phenomenon was also presented for the substitution of silicon for the two iron positions 2*a* and 6*h* in the ternary system Fe-Si-Ti.

8. Zusammenfassung

Um den Homogenitätsbereich der Laves Phase Fe_2Ti (C14) im quaternären Phasensystem Al-Fe-Si-Ti zu charakterisieren, wurden drei partielle isotherme Schnitte bei 900 °C und konstanten Titankonzentrationen von 20, 25 und 33.3 at.% mittels Röntgenpulverdiffraktometrie, Elektronenmikroskopie und optischer Mikroskopie untersucht. Zusätzlich wurden der Trend für die Besetzung der drei kristallographischen Gitterplätze 2*a*, 6*h* und 4*f* der Einheitszelle der Laves Phase Fe_2Ti mit zunehmender Löslichkeit von Silizium bzw. Aluminium und Silizium durch Rietveldverfeinerung von Pulverdaten für die Phasensysteme Al-Fe-Si-Ti und Fe-Si-Ti charakterisiert. Auch die Abhängigkeit der Gitterparameter *a* und *c*, sowie das daraus resultierende Volumen wurde in Hinblick auf die Löslichkeit von Silizium bzw. Aluminium und Silizium dargelegt.

Der Homogenitätsbereich der Laves Phase Fe_2Ti im quaternären System Al-Fe-Si-Ti bei einem konstanten Titangehalt von 33.3 at.% kann mit Hilfe der Löslichkeiten für Aluminium und Silizium aus den entsprechenden ternären Phasensystemen Al-Fe-Ti und Fe-Si-Ti, sowie durch eine leicht gekrümmte Phasengrenze durch das quaternäre System beschrieben werden. Die räumlich Ausbreitung der Laves Phase Fe_2Ti in Richtung der Titan-armen Seite des Zusammensetzungstetraeders liegt in einem Bereich von etwa 4 at.%, d.h. sie erstreckt sich bis zu einer Zusammensetzung von ca. 29 at.% Ti. Im partiellen isothermen Schnitt bei 25 at.% Titan wurde die Laves Phase ausschließlich in zwei-, drei- und vier-Phasengleichgewichten gefunden.

Die Gitterparameter *a* und *c*, sowie das daraus resultierende Volumen der Laves Phase Fe_2Ti steigen mit zunehmender Konzentration von Aluminium und Silizium (im Verhältnis 1:1), im partiellen isothermen Schnitt bei 33.3 at.% Titan an. Die erhaltenen Ergebnisse des quaternären Systems Al-Fe-Si-Ti korrelieren gut mit den Resultaten für das ternäre Phasensystem Al-Fe-Ti **[51]**. Im ternären System Fe-Si-Ti steigt der Gitterparameter *a* der Laves Phase mit zunehmendem Siliziumgehalt an, wobei ein genau umgekehrtes Verhalten für den Gitterparameter *c* und das Volumen beobachtet wird.

Es hat sich gezeigt, dass die kristallographischen Gitterplätze der Einheitszelle der Laves Phase im quaternären System Al-Fe-Si-Ti durch die Zugabe von Aluminium und Silizium nicht linear besetzt werden. Die Aluminium- und Siliziumatom substituieren bevorzugt die 2*a* Eisenposition verglichen mit der 6*h* Eisenposition. Im ternären System Fe-

Si-Ti wurde das selbe Phänomen für die Substitution von Siliziumatomen auf die zwei Eisenpositionen 2*a* und 6*h* beobachtet.

9. References

1. Stein, F., M. Palm, and G. Sauthoff, *Structure and stability of Laves phases. Part I. Critical assessment of factors controlling Laves phase stability.* Intermetallics, 2004. **12**(7-9): p. 713-720.
2. Okada, M., T. Kuriiwa, A. Kamegawa, and H. Takamura, *Role of intermetallics in hydrogen storage materials.* Materials Science and Engineering a-Structural Materials Properties Microstructure and Processing, 2002. **329**: p. 305-312.
3. Ronnebro, E., D. Noreus, M. Tsukahara, and T. Sakai, *Neutron diffraction study of the new hexagonal Laves phase (Hf,Ti)(Ni,V)(2) and its deuteride.* Journal of Alloys and Compounds, 1999. **293**: p. 169-173.
4. Livingston, J.D., *Laves-Phase Superalloys.* Physica Status Solidi a-Applied Research, 1992. **131**(2): p. 415-423.
5. Stein, F., C. He, O. Prymak, S. Voss, and I. Wossack, *Phase equilibria in the Fe-Al-Nb system: Solidification behaviour, liquidus surface and isothermal sections.* Intermetallics, 2015. **59**: p. 43-58.
6. Jacob, A., C. Schmetterer, D. Gruner, E. Wessel, B. Hallstedt, and L. Singheiser, *The Cr-Fe-Nb ternary system: Experimental isothermal sections at 700 degrees C, 1050 degrees C and 1350 degrees C.* Journal of Alloys and Compounds, 2015. **648**: p. 168-177.
7. Nei, J., K. Young, S.O. Salley, and K.Y.S. Ng, *Determination of C14/C15 phase abundance in Laves phase alloys.* Materials Chemistry and Physics, 2012. **136**(2-3): p. 520-527.
8. Yan, X.L., X.Q. Chen, A. Grytsiv, V.T. Witusiewicz, P. Rogl, R. Podloucky, and G. Giester, *On the ternary Laves phases {Sc,Ti}(2)M3Si (M = Cr, Mn, Fe, Co, Ni) with MgZn2-type.* Journal of Alloys and Compounds, 2007. **429**(1-2): p. 10-18.
9. Marker, M.C.J. and K.W. Richter, *Partial liquidus projection and vertical sections in the system Al-Fe-Si-Ti.* Intermetallics, 2014. **44**: p. 77-87.
10. Marker, M.C.J., L.I. Duarte, C. Leinenbach, and K.W. Richter, *Characterization of the Fe-rich corner of Al-Fe-Si-Ti.* Intermetallics, 2013. **39**: p. 38-49.
11. Palm, M., G. Inden, and N. Thomas, *The Fe-Al-Ti system.* Journal of Phase Equilibria, 1995. **16**(3): p. 209-222.

12. Löffler, F., *Investigations in the Ternary Systems Fe-Si-Mg and Fe-Si-Ti: Phase Equilibria and Mechanical Behaviour of Selected Alloys.* Fortschritt-Berichte VDI. Reihe, 2003. **5**: p. 1-106.

13. Hollemann, A., E. Wiberg, and N. Wiberg, *Lehrbuch der anorganischen Chemie*. 102., stark umgearbeitete und verb. Aufl. / von Nils Wiberg. ed. 2007, Berlin ; New York: Walter de Gruyter. xxxix, 2149 p.

14. Riedel, E. and C. Janiak, *Anorganische Chemie mit DVD*. 2007, Walter de Gruyter: Berlin.

15. *http://www.periodictable.com/*. [cited 2016; Available from: http://www.periodictable.com/.

16. Villars, P. and L.D. Calvert, *Pearson's handbook of crystallographic data for intermetallic phases*. 2nd ed. 1991, Materials Park, OH: ASM International.

17. Lamort, J., *Über Titaneisenlegierungen.*Ferrum, 1914. **11**(8): p. 225-234.

18. Jellinghaus, W., *Crystal structure of the compound Fe3Ti.* Zeitschrift für Anorganische Und Allgemeine Chemie, 1936. **227**(1): p. 62-64.

19. Witte, H. and H.J. Wallbaum, *Thermal and X-ray study of the system iron-titanium.* Zeitschrift für Metallkunde, 1938. **30**: p. 100-102.

20. Laves, F. and H.J. Wallbaum, *Zur Kristallchemie von Titan-Legierungen.* Naturwissenschaften, 1939. **27**(40): p. 674-675.

21. Ray, R., N.J. Grant, and B.C. Giessen, *Constitution of Metastable Titanium-Rich Ti-Fe Alloys - Order-Disorder Transition.* Metallurgical Transactions, 1972. **3**(3): p. 627-&.

22. Dew-Hughes, D., *The Addition of Mn and Al to the Hydriding Compound Feti - Range of Homogeneity and Lattice-Parameters.* Metallurgical Transactions a-Physical Metallurgy and Materials Science, 1980. **11**(7): p. 1219-1225.

23. Kaufman, L. and H. Nesor, *Coupled Phase-Diagrams and Thermochemical Data for Transition-Metal Binary-Systems .1.* Calphad-Computer Coupling of Phase Diagrams and Thermochemistry, 1978. **2**(1): p. 55-80.

24. Murray, J.L., *The Fe-Ti (Iron-Titanium) system.* Bulletin of Alloy Phase Diagrams, 1981. **2**(3): p. 320-334.

25. Massalski, T.B., H. Okamoto, P.R. Subramanian, and L. Kacprzak, *Binary alloy phase diagrams.* ASM International, 1990. **1-3**: p. 1485.

26. Kumar, K.C.H., P. Wollants, and L. Delaey, *Thermodynamic Reassessment and Calculation of Fe-Ti Phase-Diagram.* Calphad-Computer Coupling of Phase Diagrams and Thermochemistry, 1994. **18**(2): p. 223-234.

27. Jonsson, S., *Assessment of the Fe-Ti system.* Metallurgical and Materials Transactions B-Process Metallurgy and Materials Processing Science, 1998. **29**(2): p. 361-370.

28. Dumitrescu, L.F.S., M. Hillert, and N. Saunders, *Comparison of Fe-Ti assessments.* Journal of Phase Equilibria, 1998. **19**(5): p. 441-448.

29. Cacciamani, G., et al., *Critical evaluation of the Fe-Ni, Fe-Ti and Fe-Ni-Ti alloy systems.* Intermetallics, 2006. **14**(10-11): p. 1312-1325.

30. Bo, H., J. Wang, L. Duarte, C. Leinenbach, L.B. Liu, H.S. Liu, and Z.P. Jin, *Thermodynamic re-assessment of Fe-Ti binary system.* Transactions of Nonferrous Metals Society of China, 2012. **22**(9): p. 2204-2211.

31. Nishimura, H. and E. Matsumoto, *The Equilibrium Diagram of the Al-Fe-Ti System and the Segregation of Fe and Ti.* Nippon Kinzoku Gakkaishi, 1940. **10**: p. 339-343.

32. Markiv, V.Y. and V.V. Burnashova, *New Ternary Compounds in the (Sc, Ti, Zr, Hf)-(V, Cr, Mn, Fe, Co, Ni, Cu)-(Al, Ga) Systems'.* Dop. Akad. Nauk Ukrain. RSR, Ser. A, Fiz.-Mat. Tekh. Nauki, 1969. **5**: p. 463-464.

33. Markiv, V.Y., *Systems Ti-Fe-Al, Ti-Ni-Al and Ti-Cu-Al.* Akad. Nauk Ukrain. SSR, Metallofizika, 1973(46): p. 103-110.

34. Seibold, A., *Phase-Equilibria in the Ternary-System Ti-Fe-O and Ti-Al-Fe.* Zeitschrift für Metallkunde, 1981. **72**(10): p. 712-719.

35. Palm, M., A. Gorzel, D. Letzig, and G. Sauthoff, *Structure and mechanical properties of Ti-Al-Fe alloys at ambient and high temperatures.* Structural Intermetallics 1997, 1996: p. 885-893.

36. Palm, M. and J. Lacaze, *Assessment of the Al-Fe-Ti system.* Intermetallics, 2006. **14**(10-11): p. 1291-1303.

37. Vogel, R. and W. Schlüter, *The iron corner of the system iron-silicon-titanium.* Archiv für das Eisenhüttenwesen, 1938. **12**: p. 207-212.

38. Markiv, V.Y., L.A. Lysenko, and E.I. Gladyshevskii, *The Titanium-Iron-Silicon System.* J Neorg Mater, 1966. **2**(11): p. 1980-1984.

39. Jeitschko, W., *Crystal Structure of TiFeSi and Related Compounds.* Acta Crystallographica Section B-Structural Crystallography and Crystal Chemistry, 1970. **B 26**: p. 815-&.

40. Steinmetz, J., G. Venturini, B. Roques, N. Engel, B. Chabot, and E. Parthe, *TiMnSi2 and TiFeSi2 with New Orthorhombic-Type Structure.* Acta Crystallographica Section B-Structural Science, 1982. **38**(Aug): p. 2103-2108.

41. Weitzer, F., J.C. Schuster, M. Naka, F. Stein, and M. Palm, *On the reaction scheme and liquidus surface in the ternary system Fe-Si-Ti.* Intermetallics, 2008. **16**(2): p. 273-282.

42. Zakharov, A.M., I.T. Gu'ldin, A.A. Arnol'd, and Y.A. Matsenko, *Phase equilibria in the aluminum-silicon-iron-titanium system in the concentration ranges of 10-14% silicon, 0-3% iron, and 0-0.6% titanium.* Izvestiya Vysshikh Uchebnykh Zavedenii, *Tsvetnaya Metallurgiya*, 1988. **2**: p. 94-96.

43. Li, Z., X.W. Kuang, C.L. Liao, F.C. Yin, and M.X. Zhao, *Phase Equilibria of the Al-Fe-Si-Ti Quaternary System at 700 A degrees C.* Journal of Phase Equilibria and Diffusion, 2016. **37**(2): p. 174-185.

44. Friauf, J.B., *The crystal structure of magnesium di-zincide.* Physical Review, 1927. **29**(1): p. 0034-0040.

45. Laves, F., *Cristallography of alloy.* Naturwissenschaften, 1939. **27**: p. 65-73.

46. Laves, F. and H. Witte, *Crystal structure of $MgNi_2$ and its relation to the types $MgCu_2$ and $MgZn_2$.* Metallwirtschaft, Metallwissenschaft, Metalltechnik, 1935. **14**: p. 645-649.

47. Laves, F. and H. Witte, *The influence of valence electrons on the crystal structure of ternary magnesium alloys.* Metallwirtschaft, Metallwissenschaft, Metalltechnik, 1936. **15**: p. 840-842.

48. Paufler, P., *Early work on Laves phases in East Germany.* Intermetallics, 2011. **19**(4): p. 599-612.

49. Zhu, J.H., P.K. Liaw, and C.T. Liu, *Effect of electron concentration on the phase stability of NbCr2-based Laves phase alloys.* Materials Science and Engineering a-Structural Materials Properties Microstructure and Processing, 1997. **240**: p. 260-264.

50. Stein, F., Palm, M., Sauthoff, G., *Structure and stability of Laves phasses II-structure type variations in binary and ternary systems.* Intermetallics, 2005. **13**(10): p. 1056-1074

51. Yan, X.L., X.Q. Chen, A. Grytsiv, V.T. Witusiewicz, P. Rogl, R. Podloucky, V. Pomjakushin, and G. Giester, *Site preference, thermodynamic, and magnetic properties of the ternary Laves phase Ti(Fe1-xAlx)(2) with the crystal structure of. the MgZn2-type.* International Journal of Materials Research, 2006. **97**(4): p. 450-460.

52. Ipser, H., *Lecture: Phasendiagramme*, Universität Wien, Institut für Anorganische Chemie.-f. Materialien, Editor. 2015.

53. Marker, M.C.J., *Phase-equilibria, structural and physical characterization in the ternary system Al–Fe–Si and the quaternary system Al–Fe–Si–Ti.* in *Fakultät für Chemie* 2013, Universität Wien, PHD-thesis.

54. Campbell, F.C., *Phase Diagrams: Understanding the Basics*. 2012: ASM International.

55. Richter, K.W., *Lecture: Experimental methods for phase diagram determination*, Universität Wien, Institut für Anorganische Chemie-funktionelle Materialien, Editor. 2013.

56. *http://zeiss-campus.magnet.fsu.edu/articles/basics/reflected.html*. [cited 2016 1.4.]; Available from: http://zeiss-campus.magnet.fsu.edu/articles/basics/reflected.html.

57. Goldstein, J., *Scanning electron microscopy and x-ray microanalysis*. 3rd ed. 2003, New York: Kluwer Academic/Plenum Publishers. xix, 689 p.

58. *http://static.howstuffworks.com/gif/scanning-elecron-microscope-illustration.jpg*. [cited 2016 1.4.]; Available from: http://static.howstuffworks.com/gif/scanning-elecron-microscope-illustration.jpg.

59. Suryanarayana, C. and M.G. Norton, *X-Ray diffraction : a practical approach*. 1998, New York: Plenum Press. xiii, 273 p.

60. Puchegger, S. *Fakultätszentrum für Nanostrukturforschung; Zeiss Supra 55 VP*. 2015 [cited 2015 20.10.]; Available from: http://nanozentrum.univie.ac.at/home/zeiss-supra-55-vp/.

61. de Almeida, M.J.M., M.M.R. Costa, L.M. D'Alte da Veiga, L.R. Andrade, and A. Matos Beja, *Structure analysis of Laves phases with titanium.* Portugaliae physica, 1980. **11**: p. 219-227.

62. Stuwe, H.P. and Y. Shimomura, *Gitterkonstanten Der Kubisch Raumzentrierten Phasen FeTi, CoTi, NiTi.* Zeitschrift für Metallkunde, 1960. **51**(3): p. 180-181.

63. Bruckner, W., Kleinstu.K, and G.E.R. Schulze, *Atomic Arrangement in Homogeneity Range of Laves Phases ZrFe2 and TiFe2.*Physica Status Solidi, 1967. **23**(2): p. 475-&.

64. Kohlhaas, R., P. Dunner, and Schmitzp.N, *Uber Die Temperaturabhangigkeit Der Gitterparameter Von Eisen Kobalt Und Nickel Im Bereich Hoher Temperaturen.*Zeitschrift Fur Angewandte Physik, 1967. **23**(4): p. 245-&.

65. Guo, Y.Q., J.K. Liang, X.H. Zhang, W.H. Tang, Y.M. Zhao, and G.H. Rao, *Effects of Mn and Cu doping in La(T,Al)(13) (T=Fe,Co) on crystal structure and magnetic properties.* Journal of Alloys and Compounds, 1997. **257**(1-2): p. 69-74.

66. Popiel, E., M. Tuszynski, W. Zarek, and T. Rendecki, *Investigation of Fe3-Xvxal Alloys with Do3 Type-Structure by X-Ray, Magnetostatic and Mossbauer-Effect Methods.* Journal of the Less-Common Metals, 1989. **146**(1-2): p. 127-135.

67. Mishra, S.N., D. Rambabu, A.K. Grover, R.G. Pillay, P.N. Tandon, H.G. Devare, and R. Vijayaraghavan, *Mossbauer and Magnetization Studies in Fe3-Xruxsi.* Journal of Applied Physics, 1985. **57**(8): p. 3258-3260.

68. Inden, G. and W. Pepperhoff, *Experimental-Study of the Order - Disorder Transition in Bcc Fe-Al Alloys.* Zeitschrift Fur Metallkunde, 1990. **81**(10): p. 770-773.

69. Nowotny, H., H. Auer-Welsbach, J. Bruss, and A. Kohl, *Ein Beitrag zur Mn5Si3-Struktur (D 88-Typ).*Monatshefte für Chemie und verwandte Teile anderer Wissenschaften, 1959. **90**(1): p. 15-23.

70. Emsley, J., *The elements*. 3rd ed. 1998, Oxford

10. Appendices

10.1. List of tables

10.2. List of figures